

## **ABSTRACT**

SAPTARSHI, SOURABH. Laser Powder Bed Fusion Additive Manufacturing of Oxide Dispersion Strengthened Steel by In-Situ Reaction Synthesis. (Under the direction of Dr. Timothy Horn and Dr. Djamel Kaoumi).

Recent progress in oxide dispersion strengthened (ODS) steels produced by mechanical alloying (MA), and gas atomization techniques allow them to be used as fuel cladding in nuclear fission and fusion reactors. The thermally and mechanically stable nano oxide dispersoids in a ferritic and chromium matrix improve the radiation and creep resistance at high temperatures. As a result, ODS steels have a strong potential for high burnup (long-life) and high-temperature applications. However, the large-scale processing of ODS steels is a significant challenge. As part of this thesis, the current progress in the development of these ODS steel claddings, including their relevant mechanical properties like tensile and creep strengths, and irradiation performance, is reviewed. Furthermore, different ways to fabricate solid ODS parts have also been reviewed with a specific focus on additive manufacturing.

Experiments involving powder processed through a novel Gas Atomized Reaction Synthesis (GARS) methodology using laser powder bed fusion additive manufacturing (LPBF AM) have been characterized and analyzed for feasibility and scalability as part of this thesis. Experiments involving different powder composition under different atmospheric conditions have been characterized and compared for desired oxide density and mechanical properties. Tensile tests were performed to test for elongation and compare stress strain results with ODS samples prepared with HIP.

© Copyright 2022 by Sourabh Saptarshi

All Rights Reserved

Laser Powder Bed Fusion Additive Manufacturing of Oxide Dispersion Strengthened Steel by  
In-Situ Reaction Synthesis

by  
Sourabh Manoj Saptarshi

A thesis submitted to the Graduate Faculty of  
North Carolina State University  
in partial fulfillment of the  
requirements for the degree of  
Master of Science

Mechanical Engineering

Raleigh, North Carolina  
2022

APPROVED BY:

---

Dr. Timothy Horn  
Committee Co-Chair

---

Dr. Djamel Kaoumi  
Committee Co-Chair

---

Dr. Mohammed Zikry

---

Dr. Christopher Rock

## **DEDICATION**

Dedicated to my parents and my sister without whose support, this would not have been possible.

## **BIOGRAPHY**

My name is Sourabh Saptarshi and I was born in Chennai, India. I am pursuing an MS degree from the department of Mechanical and Aerospace Engineering at North Carolina State University (NC State University). After earning a bachelor's degree in Mechanical Engineering from Mukesh Patel School of Technology Management and Engineering in Mumbai, India, I moved to the US to further my studies and gain valuable experience working in the new product industrialization domain. At NC State, I got the opportunity of working and pursuing my research interest at the Center for Additive Manufacturing and Logistics, in the field of Additive Manufacturing and material development.

## ACKNOWLEDGMENTS

Firstly, I would like to thank my parents and family for their unconditional love and support without which, none of this would have been possible.

I would like to thank Dr. Timothy Horn for giving me the opportunity to work as a research assistant under his guidance and support. I would also like to thank Dr. Djamel Kaoumi, Dr. Mohammed Zikry and Dr. Christopher Rock for their guidance and mentoring throughout my time at NC State. The focused ion beam and transmission electron microscopy characterization of the samples produced in this study was carried out by Matthew DeJong and Dr. Ryan Schoell from Dr. Kaoumi's research group. I would like to thank Dr. Jennifer Forrester at the N.C. State Analytical Instrumentation Facility and Dr. Saul Lapidus at the Applied Photon Source at Argonne National Laboratory for assistance in collecting and analyzing the x-ray diffraction data we produced on the GARS precursor materials and solid samples. I would also like to thank Dr. Ruksana Baby for helping with microCT characterization and analysis, which was carried out at the N.C. State Analytical Instrumentation Facility.

I would like to thank Dr. Mark Pankow's BLAST lab for providing us with the high speed camera to perform DIC tensile testing and my lab mates Dr. Prithwish Tarafder, Nicholas Muecke, Emmanuel Amoako and Satya Konala, not only for all the help, but also for all the fun times that made my time at CAMAL very enjoyable.

I would also like to acknowledge the important contributions of our collaborators at AMES lab and Iowa State University for their pioneering work on the gas atomization reaction synthesis powders that we used in this study, Dr. Iver Anderson, Dr. Tim Prost, Dr. Emma White, Dr. Ralph Napalitano and Dr. Joel Rieken. Additionally, I would like to thank our collaborators at Pacific Northwest National Lab for the important discussions related to the processing GARS powders.

This work was carried out under the ARPA-E GAMOW (Galvanizing Advances in Market-Aligned Fusion for an Overabundance of Watts) program, DE- AR0001379, “Microstructure Optimization and Novel Processing Development of ODS Steels for Fusion Environments”.

This work was performed in part at the Analytical Instrumentation Facility (AIF) at North Carolina State University, which is supported by the State of North Carolina and the National Science Foundation (award number ECCS-2025064). The AIF is a member of the North Carolina Research Triangle Nanotechnology Network (RTNN), a site in the National Nanotechnology Coordinated Infrastructure (NNCI). Special thanks to James Rule at Thermo-Calc for assistance with thermodynamic calculations.

Portions of the preliminary data on the GARS powder used in this study were generated with support from the Department of Energy, Office of Fossil Energy (ARM program) through Ames Laboratory contract no. DE-AC02-07CH11358 is gratefully acknowledged. Use of the Advanced Photon Source at Argonne National Laboratory was supported by the U. S. Department of Energy, Office of Science, Office of Basic Energy Sciences, under Contract No. DE-AC02-06CH11357.

Finally, I would like to thank all my friends here at NC State and back home in Mumbai, India for the fun memories and constant support during rough times.

## TABLE OF CONTENTS

LIST OF TABLES .....	vii
LIST OF FIGURES .....	viii
<b>Chapter 1: Introduction</b> .....	<b>1</b>
1.1 Introduction.....	1
1.2 Thesis Structure .....	3
<b>Chapter 2: Literature Review</b> .....	<b>5</b>
2.1 Literature Review.....	5
2.2 Desired ODS properties .....	7
2.2.1 Radiation .....	7
2.2.2 Strengthening Mechanism .....	9
2.3 ODS Steel Powder Manufacturing.....	12
2.3.1 Mechanical Alloying (MA).....	12
2.3.2 Gas Atomization (GA) .....	15
2.3.3 Gas Atomization Reaction Synthesis (GARS) .....	19
2.3.4 Surface Treatment of gas atomized powder followed by Reaction Synthesis (STARS) .....	21
2.4 Consolidation Methods for ODS powder .....	22
2.4.1 Hot Isostatic Process (HIP).....	22
2.4.2 Friction Stir Welding (FSW) .....	23
2.4.3 Spark Plasma Sintering (SPS).....	24
2.4.4 Shear Assisted Processing and Extrusion (ShAPE).....	25
2.4.5 Additive Manufacturing.....	27
<b>Chapter 3: GARS: Cr-166</b> .....	<b>31</b>
3.1 Introduction.....	31
3.2 Additive Manufacturing Approach with Preliminary Cuboid Designs .....	36
3.3 Results and Discussion .....	38
3.4 Conclusions Drawn from Preliminary Cuboid Designs.....	49
<b>Chapter 4: GARS: ASC-1-81</b> .....	<b>52</b>
4.1 Background Information.....	52
4.2 Hypothesis.....	52
4.3 Methodology .....	53
4.3.1 Powder Preparation and Characterization.....	53
4.3.2 Laser Powder Bed Experimental Setup .....	56
4.4 Discussion .....	63
4.4.1 Powder Characterization.....	63
4.4.2 Solid Sample Characterization.....	68
4.4.3 Large Block Fabrication .....	86
4.4.4 Tensile Tests .....	89
4.5 Summary and Conclusion .....	91
4.6 Future Work .....	94

## LIST OF TABLES

Table 2.1	Literature review of existing research additive manufacturing using ODS powder .....	30
Table 3.1	Chemical composition in wt.% of the powder feedstock by ICP and inert gas fusion.....	31
Table 4.1	Mass and nominal size distribution of the 14YWT powder received from AMES lab (Batch ID: ASC-1-81) .....	54
Table 4.2	Powder composition of the 14YWT powder received from AMES lab (Batch ID: ASC-1-81) .....	54
Table 4.3	Typical LPBF processing parameters utilized for each gas mixture (Ar, Ar+3%O <sub>2</sub> , Ar+5%O <sub>2</sub> , Ar+7%O <sub>2</sub> and Ar+10%O <sub>2</sub> ).....	61
Table 4.4	Scan line length and islanding parameters used in this study, the X and Y size determine the scan line length. THE X and Y step determine how much this pattern shifts from one layer to the next and the angle of rotation is the angle of the island about the z axis relative to the sample X and Y axes .....	61

## LIST OF FIGURES

Figure 2.1	Figure. 2.1: Incoherent (left) and coherent (right) crystal structure [51] .....	7
Figure 2.2	BF-STEM, HAADF, and X-ray mapping results for as-extruded control material. In-depth variations in Cr–K and Fe–K are a thickness effect [19].....	8
Figure 2.3	STEM images and X-ray maps of samples irradiated with $4 \times 10^{20}$ Pt/m <sup>2</sup> , with a peak dose of 160 dpa irradiated at 750 C [19] .....	8
Figure 2.4	Oxide dispersoids acting as obstacles for the dislocation line [60].....	11
Figure 2.5	Inside of a ball mill process [63] .....	12
Figure 2.6	Top-Left image is SEM image of as-received bimodal Ti-16Sn-4Nb powder. Bottom- right image is SEM image of powder that were milled for 20 hrs [67] .....	14
Figure 2.7	Titanium X-ray maps obtained by EPMA of powder grains resulting of the milling of FeCrW + FeTi + YFe <sub>3</sub> + Fe <sub>2</sub> O <sub>3</sub> for different durations of milling [73] ..	15
Figure 2.8	Systematic representation of the working principle of a Vacuum Inert gas atomizer [91] .....	16
Figure 2.9	Illustration showing the atomization of the GARS powders [99] .....	20
Figure 2.10	The ODS microstructure evolution during hot consolidation of GARS precursor powder: a) initial low-temperature consolidation showing intact PPBs, b) dissociation of the PPBs (simulating heat treatment) and O diffusion into the $\alpha$ -(Fe,Cr) matrix, and c) formation of Y-enriched oxide dispersoids throughout the microstructure [9] .....	20
Figure 2.11	Typical process map for HIPed samples [108] .....	23
Figure 2.12	A schematic representation of a typical FSW process used to weld two ODS plates together while a rotating tip is plasticizing the two metals to fuse them together [111] .....	24
Figure 2.13	Schematic representation of a SPS system [113] .....	25
Figure 2.14	Schematic representation of a typical ShAPE apparatus [119] .....	26
Figure 2.15	Schematic process map representation of energy density plot obtained from literature review [99] .....	29
Figure 3.1	Histogram showing the volumetric powder size distribution measured by laser diffraction [99] .....	32

Figure 3.2	Backscatter SEM images in compositional mode of the Cr-166 feedstock prior to use in LPBF. ....	33
Figure 3.3	BEC microscope image of typical GARS powder showing a predominant Cr-Fe shell with small regions of oxides rich in Yttrium and Titanium .....	33
Figure 3.4	Gallium Ion contrast image of a cross-section of representative Cr-166 GARS powder particle at 200 X(A), 1500 X(B), 3500X (C) and 6492X (D) magnification. ....	34
Figure 3.5	EPMA chemical map of a Gallium Ion contrast image of a cross-section of representative GARS powder particle showing presence of elemental Yttrium indicated by yellow arrow (A), STEM HAADF and EDS images of regions rich in yttrium and iron near grain boundaries (B) [99] .....	34
Figure 3.6	FIB cross-section of a GARS powder particle (A-C), FIB cross-section of the surface of a 58 mm powder particle during TEM liftout (D), AES depth profile of the surface of a powder particle (E) EDS line scan overlay on a TEM image of a surface oxide (F). Figure D-F analysis was performed by Dr. Rieken on Cr-166 powder as part of his dissertation [9] .....	35
Figure 3.7	Modified Concept laser platform at N.C. State (A), Illustration showing how the GARS powder was loaded into the powder feeder to maximize build height (B) and Photograph of the build chamber showing the setup and location of carbon tape for collecting ejected spatter .....	36
Figure 3.8	Experimental setup showing the Concept Laser M100R sample fabrication (A), composite samples after fabrication produced with 4 different chamber environments (B), and illustration of sample fabrication and atmosphere strategy (C) [99] .....	37
Figure 3.9	Equilibrium thermodynamic results for 100 ppm (A), 410 ppm (B), 5000 ppm (C) and the natural logarithm of oxygen activity (D) at different oxygen concentration .....	38
Figure 3.10	XRD results of powder (bottom) and fabricated solids with each respective chamber atmosphere: argon – red, 5 wt% oxygen – green, air – blue (top).....	39
Figure 3.11	SEM images of fabricated solids produced in argon atmosphere showing EDS maps of Fe-Cr-Ti-Y rich areas .....	40
Figure 3.12	Photograph showing spatter generation at 1% oxygen atmosphere (A) and the accumulation of spatter particles at the completion of the test run (B).....	41

Figure 3.13 Backscattered SEM image of the spatter particle (A), EDS map color image (pink-Cr, red-Y, green-Ti, blue-O) showing typical micron scale Y-Ti-O Oxides overserved prevalently on the surface of ejected spatter particles (B). Arrows indicate yttrium-containing areas of interest .....	41
Figure 3.14 HAADF TEM images for the samples produced with LPBF in Argon, 1% oxygen, 5% oxygen and Air with respective Ti-Y-O EDS maps [99] .....	43
Figure 3.15 TEM For the samples produced with LPBF in Argon with Ti-Y-O EDS map and selected particle EDS line scans .....	44
Figure 3.16 TEM For the samples produced with LPBF in 1% O <sub>2</sub> with Ti-Y-O EDS map.....	44
Figure 3.17 TEM For the samples produced with LPBF in Air with respective Ti-Y-O EDS map and selected particle EDS line scans .....	45
Figure 3.18 Nano oxide size distributions from TEM images for samples fabricated in Argon, 1% oxygen, 5% oxygen and air [99] .....	45
Figure 3.19 Plot showing the median oxide size measured from TEM, error bars indicate the 10th and 90th percentiles of the oxide size distribution (A). Plot showing The measured density of oxides per m <sup>3</sup> (B). Thickness maps from EELS analysis were used to calculate volumetric oxide densities (C) [99] .....	47
Figure 3.20 Cumulative distribution of nano-oxides reported in this study as compared to the current literature [99].....	48
Figure 3.21 Contour map showing the Vickers hardness, measured over a 5mm x 8mm region of the LPBF consolidated GARS sample encompassing regions processed in argon, 1%O <sub>2</sub> , 5%O <sub>2</sub> and in air atmospheres .....	49
Figure 4.1 Histograms showing the Volume and Number Particle Size distribution of 20μm-45μm (A & B), 45μm-53μm (C & D) and a 20μm-53μm (E & F) after blending in an argon glovebox .....	55
Figure 4.2 Secondary scanning electron microscope images (100X, 250X and 500X) showing a bimodal powder size distribution and generally spherical morphology .....	56
Figure 4.3 Photograph of the LPBF/GARS experimental setup and workflow .....	58
Figure 4.4 Spectrum of optical emissions (OES) recorded for three samples during LPBF. Argon (Dark blue), Argon +5% oxygen (green), and Argon +10% (light blue) .....	58

Figure 4.5	Schematic of the build substrate and steel inserts upon which the LPBF samples were fabricated (A) and ISO-view CAD model of the same (B), final machined plate with slots (C) .....	59
Figure 4.6	Example of the toolpath output showing the 10mmx 10mm islands on a single layer of a 7.5 x 15mm sample. Left sample has a 30 $\mu$ m hatch spacing (A) and right sample has 80 $\mu$ m hatch spacing (B) .....	62
Figure 4.7	Photograph of the 150g vial of ASC-1-81 powder used for each experiment (A) and photograph showing how the powder was loaded into the LPBF powder deposition chamber (B) .....	62
Figure 4.8	Photographs showing an example of the samples being processed during LPBF (A), and after removal of the sample insert (B) .....	63
Figure 4.9	TEM image of a liftout harvested from a powder particle (A). The arrows indicate larger areas rich in Y, and the red arrows indicate discontinuous regions rich in Y. The labeled boxes indicate areas analyzed with STEM/EDS (B,C, & D). The STEM/EDS images highlight the distribution of elements in the shell of the powder (B) and the interior (C & D) .....	65
Figure 4.10	XRD results between 10 $^{\circ}$ and 80 $^{\circ}$ 2 $\theta$ for the GARS powders and LPBF fabricated solids (A). The inset in 'A' shows a higher resolution scan between 30 $^{\circ}$ and 44 $^{\circ}$ 2 $\theta$ . HE-XRD scans from APS beamline 11B confirm the presence of the Y <sub>2</sub> Fe <sub>17</sub> in the powder (B).....	68
Figure 4.11	Photograph showing a pair of LPBF samples after extraction from the insert and sectioning (right) and after cold mounting, grinding, and polishing .....	69
Figure 4.12	Optical microscope image tiles from the "Argon" atmosphere case across various speed and hatch spacing combinations .....	71
Figure 4.13	Measured optical relative density as a function of the volumetric energy density ( $E=P/vht$ J/mm <sup>3</sup> ).....	72
Figure 4.14	Plot of the volumetric energy density ( $E=P/vht$ J/mm <sup>3</sup> ) as a function of the beam velocity for LPBF samples produced in an Argon atmosphere. ....	73
Figure 4.15	Plot of the volumetric energy density ( $E=P/vht$ J/mm <sup>3</sup> ) as a function of the beam velocity for LPBF samples produced in an Argon+3% oxygen atmosphere .....	73
Figure 4.16	Plot of the volumetric energy density ( $E=P/vht$ J/mm <sup>3</sup> ) as a function of the beam velocity for LPBF samples produced in an Argon+5% oxygen atmosphere .....	74
Figure 4.17	Plot of the volumetric energy density ( $E=P/vht$ J/mm <sup>3</sup> ) as a function of the beam velocity for LPBF samples produced in an Argon+7% oxygen atmosphere .....	74

Figure 4.18 Plot of the volumetric energy density ( $E=P/vht$ J/mm <sup>3</sup> ) as a function of the beam velocity for LPBF samples produced in an Argon+10% oxygen atmosphere .....	74
Figure 4.19 Photograph of sample S10 from on the steel build insert (A) and micro-CT images showing high sample density (B-I) .....	77
Figure 4.20 micro-CT images showing regions of high density and pockets of large scale porosity in sample S2 that are likely the result of a layer spreading defect .....	78
Figure 4.21 Highlighted box shows sample S2 after powder application (A) and the final printed layer (B).....	78
Figure 4.22 MicroCT images of S71 showing high sample density (A-D). The extensive keyhole porosity in E-I is only apparent at the periphery of the scan line length islanding regions indicating that the steady state parameters for S71 are within the process window .....	79
Figure 4.23 Bar graph showing the hardness of all samples (S1-S92) grouped by the atmospheric condition during LPBF (error bars indicate one +/- standard deviation from the mean) .....	80
Figure 4.24 Representative backscatter electron microscope image from sample S2 produced in an argon atmosphere during LPBF.....	81
Figure 4.25 Backscatter electron microscope image from sample S2 from a region exhibiting micro-scale Y-Ti-O inclusions indicated by yellow arrows. Microscale lack of fusion porosity was also observed, but was not prevalent, and is indicated by the yellow circles.....	82
Figure 4.26 Backscatter electron microscope image from sample S2 from a region exhibiting micro-scale oxide inclusions in the vicinity of lack of fusion defects and, the EDS maps indicate these are rich in Ti-Y-O .....	82
Figure 4.27 Secondary electron microscope image from sample S64 from a region exhibiting micro-scale oxide inclusions in the vicinity of lack of fusion defects, the EDS maps indicate these are rich in Cr-Ti-O .....	83
Figure 4.28 Electron Backscatter Diffraction image of representative ASC1 1-81 Solid fabricated with LPBF (500x 0.4um step). Reconstructed IPF Map (left) and Pole Figure (right) .....	83

Figure 4.29 HAADF image of the liftout (A), the red box indicates the region of the STEM/EDS analysis shown in (C). EELS mfp map used to calculate the liftout thickness in the region of interest (B). The size distribution of oxides combined from multiple measurements on the liftout (D), and SAED patterns identifying the BCC Fe matrix and the Ti <sub>2</sub> Y <sub>2</sub> O <sub>7</sub> particles .....	85
Figure 4.30 Photograph of two LPBF fabricated test articles with dimensions 25 x 15 x 15 mm. Samples were built using 608mm/sec and a hatch spacing of 50um. Sample on the left was fabricated in inert environment (A) and in reactive Argon + 3% O <sub>2</sub> (B).....	86
Figure 4.31 BSE tiled image of S98 (15mm x 15mm x 25mm) sample printed in inert environment (A) and zoomed in image of areas depicting porosity in the micron level (B) .....	87
Figure 4.32 EBSD low magnification inverse pole figure (ipf) map for S98 showing a strong texture in the <100> direction (A), and a high magnification backscatter SEM image of a region enlarged from Figure 4.31 B showing a distribution of low-density particles indicated by the white arrows (B).....	88
Figure 4.33 Photograph of LPBF fabricated tensile bar stock with dimensions 14mm x 80mm x 8mm.....	89
Figure 4.34 Photograph of the CAD model of the tensile bar (A), as EDMed 2 tensile bars from the large tensile sample (B) .....	90
Figure 4.35 Grasshopper images of tensile being pulled in the lateral direction. As mentioned, pulling direction was perpendicular to the build direction.....	91
Figure 4.36 DIC maps showing the development of strain in the tensile sample from the start of the test until failure.....	91

# CHAPTER 1

## 1.1 Introduction

The objective of this study is to explore the potential of laser powder bed fusion (LPBF) additive manufacturing (AM) to melt precursor powders produced by Gas Atomization Reaction Synthesis (GARS) to produce an Oxide Dispersion Strengthened (ODS) steel.

ODS steels have increased in popularity in Generation IV nuclear reactors as well as in nuclear fuel claddings. This is in part due to the high creep, fatigue, and temperature resistance that ODS steels offer. ODS steels are also known to have high radiation resistance [1,2]. Fuel claddings are able to withstand high temperatures up to 700 °C[3,4] but they are not commonly used because of the time and cost associated with mechanically alloying (MA) and consolidating the powder materials from which they are made.

The currently accepted practice for processing ODS steels requires the forced dissolution of nano-scale  $Y_2O_3$  powder into the steel matrix by MA, followed by hot consolidation and thermomechanical processing that precipitates Y-Ti-O nano-scale oxides [5]. However, the extensive MA, which typically exceeds 40 hrs, and limited machinability present an impediment to the scalability of ODS steel alloys [6].

MA processes were developed to combine different compositions in powder form, which would otherwise be thermodynamically difficult to cast. Powders are typically blended together in a defined ratio in a jar that is filled with metallic balls. The jar is rotated, and the mechanical interaction between the balls and the powder results in repeated cold welding and fracturing of powder particles. The process can be carried out in a dry or wet solution. Lubrication is often used to prevent agglomeration or a change in microstructure due to heat build-up [7]. Mechanical alloying can also be carried out with high or low energy mixing. The repeated cold welding along

with strain-induced diffusion progressively homogenizes the powder. The properties of the end resulting powder depend significantly on milling parameters such as milling time, ball-to-powder ratio (BPR), milling media, and rotation speed. Typically, ODS steel powders are produced by combining a premade gas atomized alloy matrix (e.g., Fe-Cr-Al, Ni-Ti, Nb-Al), which is then milled with about 0.3 weight % yttrium or aluminum oxide ( $Y_2O_3$  or  $Al_2O_3$ ). Over time, and by constant shearing and cold welding of the oxides and the metal powder, yttrium is forced into solid solution and later precipitates as a pyrochlore when the powder is thermally processed. This process takes several hours and can be limited by the batch size. While the MA process can be scaled, several challenges exist. For instance, jars that are several meters in diameter and oriented horizontally may impart insufficient kinetic energy through ball impact [8]. Another limitation is batch-to-batch variation due to the use of balls to shear oxide and metal particles. Contamination from the balls, container media as well as the use of lubricating media is another concern. Over the years, there have been many alternative powder processing methods that have been developed that address these limitation. One of those is gas atomization reaction synthesis (GARS) which was developed at AMES laboratory [9–11]. In GARS method, all of the elements are melted in a crucible and homogenized together in a controlled melt chamber which is filled with an inert gas - argon. The molten alloy is then released into the cooling chamber where it is disintegrated into droplets by impact from a high energy reactive Ar + O<sub>2</sub> gas jet. The presence of added O<sub>2</sub> in the gas jet helps to form a kinetically stable oxide crust on the powder which acts as chemical reservoir for formation of yttrium oxide during melt pool phase [9,11].

Radiation and mechanical responses of ferritic steels based on 14YWT (Fe-14Cr-3W-0.4Ti-0.2Y) composition developed at Oak Ridge National Laboratory [12,13], have been widely used to study the microstructure and mechanical properties of ODS alloys [12,14–18,18–20]. In

this composition, Cr is added to Fe as a ferrite stabilizer [21], along with elements such as Ti [22] and W [23] for particle stabilization and solid solution strengthening, respectively. Y is then added elementally to the molten alloy. While producing ODS alloys using GARS method, after the homogenized liquid droplets break up, the rapid solidification results in the formation of Y-containing intermetallic (typically  $Y_2Fe_{17}$ ) or Y in supersaturated solid solution with Fe-Cr-Ti-W. A kinetically stable  $Cr_2O_3$  crust is formed over the powder which, is used as an oxygen reservoir. During HIP, this  $Cr_2O_3$  crust disintegrates releasing the trapped oxygen, paving the way for the oxygen to dissolve into the crust to form stable  $Y_2Ti_2O_7$  pyrochlore oxide dispersoids [9–11].

In this thesis, we explore the use of Fe-Cr GARS powder consolidated by LPBF AM under varying atmospheric conditions to demonstrate and understand the in-situ formation of oxides from liquid-phase processing and rapid solidification.

## 1.2 Thesis Structure

This thesis consists of a literature review on the current state of ODS alloys (Chapter 2). The literature review includes sections on how ODS steels are conventionally prepared. The literature review also covers the GARS method of producing ODS alloys which bypasses the requirement for MA processing. In chapter 3, a GARS powder composition that was previously used by Reiken et al. [9] for HIP consolidation was processed by LPBF. Oxygen content of the LPBF chamber atmosphere was varied to determine its influence on the formation of nano-oxides in the liquid melt pool. The precursor GARS powders and resulting samples were characterized to confirm the hypothesized reaction synthesis and to begin to elucidate the potential pathways for oxidation. In chapter 4, a new batch of powder was produced by AMES lab with a composition consistent with a common ODS steel alloy, 14YWT. 14YWT composition was chosen as extensive

research has been conducted to study the mechanical and radiation response of samples produced using 14YWT ODS alloy. Majority of these samples are produced using HIP, friction stir welding, while little work has been done to characterize the feasibility of using additive manufacturing. This chapter describes efforts to define a feasible and stable LPBF processing space and presents validation of the in-situ reaction synthesis as well as materials and mechanical characterization of the produced samples.

## CHAPTER 2

### 2.1 Literature Review

Recent advances in oxide dispersion strengthened (ODS) ferritic stainless steels have been very encouraging and, as a result, have seen extensive usage in fuel cladding, ducts, and structural components in sodium-cooled fast reactors (SFR) [24], generation IV nuclear reactor and fusion and fission reactors [25–27]. Fe-Cr matrix ODS alloys are promising not only due to their microstructure but also because of the presence of Y–Ti–O nano oxides dispersed along the grain boundaries. These nano oxides have been observed to impart excellent creep strength at high temperatures (up to 750°C) and high DPAs [24,28]. Traditionally these ODS alloys are made by mechanically alloying Fe-Cr-Y based alloy matrix powder with an oxide (either  $Y_2O_3$  or  $Al_2O_3$ ), and then the resulting powder is Hot Iso-statically Pressed (HIP) which leads to the generation of high-density nanoclusters [24,29]. Based on transmission electron microscopy (TEM), x-ray diffraction (XRD), atom probe tomography (APT) results, in a  $Y_2O_3$  Fe-Cr ODS alloy, cubic  $Y_2Ti_2O_7$  and orthorhombic  $Y_2TiO_5$  oxides (ranging from 2-30 nm) in an equilibrium phase have been identified [14,30–32].

Fission and fusion reactor service conditions are characterized by combinations of high temperatures, large stresses, chemically reactive environments, and intense neutron radiation fields. In a generation IV nuclear reactors, irradiation damage can reach several hundred displacements per atom (DPA) at temperatures ranging from 400 to 700°C [3,4,18,33]. Depending on the radiation levels and applications, atoms displaced from their lattice positions can create large excess concentrations of vacant and self-interstitial atom (SIA) defects, typically characterized by a neutron dose unit of DPA [34,35]. Displacement damage drives microstructural evolutions, changes in the dislocation structures, induced precipitation, and growing voids. This

degrades material properties such as hardening, fracture toughness, tensile strain, high-temperature irradiation creep property, introduction of void swelling, and large reductions of creep rupture lifetime and ductility [36].

Ferritic Fe-Cr alloy composition matrix with a chromium-rich ODS steels are ideal for applications in nuclear fusion and generation IV fission reactors and, as a result, have gained popularity over the years in part due to favorable creep resistance at higher temperatures [4,16,37,38] and as fuel cladding, duct and structural component for gas and liquid metal reactors [39]. A major reason is that the ferritic state makes the iron-base alloys less susceptible to radiation damage and void swelling [40].

Compared to precipitation hardening or other types of hardening methods, ODS alloys have a stable structure across a wide range of temperatures, and several studies have shown it to be anisotropic [41–43]. Conventionally ODS steels are extruded or rolled which causes the grain structure to be parallel along the direction of extrusion. The oxides have been observed to pin themselves along grain boundaries and also along elongated grain structure [20,44,45]. Precipitation hardening on the other hand is generally isotropic [46]. Solutes that are added to the liquid metal matrix, act as the necessary dispersoids to prevent dislocation along the slip plane.

Depending on the oxide size, there is coherency and or semi-coherency ( $D_{\text{oxide}} < 20\text{nm}$ ) between the oxide dispersoids in the ODS alloy which is what gives the parts the high tensile strength [47–50]. An incoherent precipitate is separated from the crystal structure (not related to the crystal structure) of the surrounding matrix, whereas a coherent precipitate (related to surrounding crystal structure) forms a definitive structure between itself and the matrix's crystal structure. In ODS alloy, the semi-coherent dispersoids act as dislocation barriers and pin the dislocation line, whereas in a precipitation-hardened material, the zones or Grain Boundary (GB)

act as obstacles to the dislocation line. Figure 2.1 below shows the difference between incoherent and coherent dislocations.

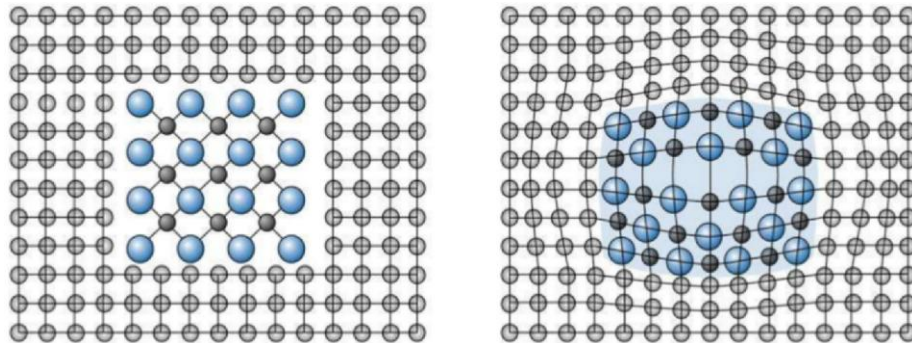


Figure. 2.1: Incoherent (left) and coherent (right) crystal structure [51].

## 2.2 Desired ODS Properties

### 2.2.1 Radiation

There are studies on various Fe-Cr ODS compositions with Y, Zr, Al, W, and or Ti additions, as well as commercially available ODS alloys such as MA957 that indicate an irradiation-induced change in grain structure, grain elongation, NC density, mechanical property and material performance over prolonged exposure [1,2,19,52]. Ribis et al. reported a reduction in NC density as well as diameter for MA957 (Fe-13.87Cr-1.05Ti-0.3Mo-0.13Ni-0.1Al-0.22Y<sub>2</sub>O<sub>3</sub> commercially available ODS ferritic alloy developed by International Nickel Company - INCO [53]) samples exposed to about 75 DPA and 430°C [1]. The ability of ODS alloys retaining its elemental composition even after heavy irradiation damage is crucial for its prolonged application. Certain et al. reported a reduction in NC density for a 14YWT sample exposed to high radiation of 100 DPA Ni<sup>+</sup> irradiation with a complete NC dissolution over a temperature range of -75°C to 100°C but at the same time, observed sporadic distribution of larger NC over 300°C which, was confirmed by APT [2].

Parish et al. analyzed a 14YWT sample and noticed coarse grain boundaries along the depth of an as fabricated sample (Figure 2.2). After exposure with 10MeV Pt<sup>3+</sup> ion and at higher temperature of 750°C, Parish et al. noticed a homogenous grain thickening with an evident Y, Ti, W and Cr grain boundary enrichment with no visible change to grain structure at a 0dpa depth in the as irradiated sample (Figure 2.3) [19]. These analysis by Certain et al. and Parish et al. prove that even after high irradiation, the elemental composition remained consistent even though the NC density changed with a change in dosage and irradiation temperature [2,19]. These findings theorize that the ability of ODS alloys to retain NCs and GBs at higher temperatures and irradiation will be beneficial to trapping point defects and retaining high temperature creep properties [19].

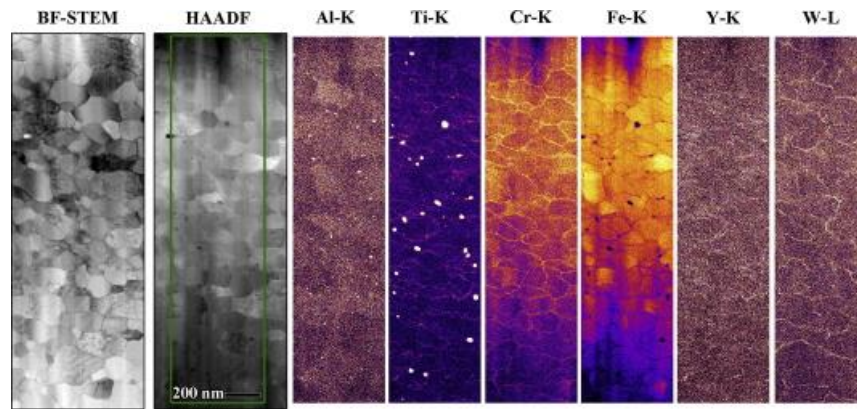


Figure 2.2: BF-STEM, HAADF, and X-ray mapping results for as-extruded control material. In-depth variations in Cr-K and Fe-K are a thickness effect [19].

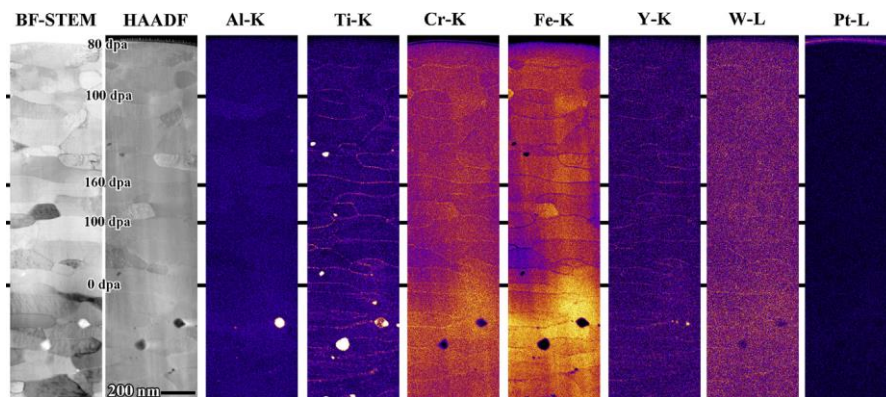


Figure 2.3: STEM images and X-ray maps of samples irradiated with 4x1020 Pt/m<sup>2</sup>, with a peak dose of 160 dpa irradiated at 750 C [19].

### 2.2.2 Strengthening mechanism

The strength of a material is its resistance to deformation. Beyond the elastic limit, yielding occurs due to movement of dislocations which results in plastic deformation. Dislocation movement is mitigated if some barrier or discontinuity comes in the path of dislocations. The effect of a barrier/discontinuity depends on its strength and size. In the case of ODS alloys, NCs act as these barriers/discontinuity. The boundary and dislocation interactions can be described by the Orowan mechanism [54,55]. Orowan studied the of flow stress resulting from a distribution of impenetrable obstacles on the slip plane [56].

Orowan dislocation mechanism describes each dispersions/dispersoids in the matrix acts as a stress concentrator [56]. It describes the interaction of dislocation with dispersions in a crystalline material. When a dislocation passes through these stress concentrators along the slip plane, the dislocations form a loop around each dispersoid/stress concentrator. This break in the dislocation in turn prevents the dislocations from easily gliding past the grain boundaries/slip plane [57]. The shape of the dislocation is influenced by anisotropy [54]. Hence, if there are more fine nano clusters along the grain boundaries, there is more resistance to the movement of dislocations and hence an increase in strength. NCs accumulate at grain boundaries, leading to the formation of local superstructures. A higher number of smaller grains along the grain boundary provide a stronger resistance of dislocation.

Martin's model demonstrates that the effect of NC strengthening mechanism can be attributed to particle spacing [58]. Compact NC spacing will yield better strengthening. The average particle spacing can be calculated by using equation 2.1 [58] –

Equation 2.1 -

$$\lambda_{\text{avg}} \cong 1.25r \left( \sqrt{\frac{2\pi}{3f}} \right)$$

Where –

$\lambda$  = particle spacing

$r$  = particle radius

$f$  = volume fraction of particle phase

The basic Orowan equation as modified by Ashby for polycrystalline materials with incorporated particles spacing, estimation of line spacing and mutual interaction of dislocation of particle yield stress of the material is described by Equation 2.2 [59] –

Equation 2.2 :

$$\sigma = \frac{0.83M\mu b}{2\pi\sqrt{1-\nu}} \left( \frac{\ln\left(\frac{2r}{r_0}\right)}{\lambda_s - 2r_s} \right)$$

Where:  $M$  = Taylor's factor

$\mu$  = shear modulus

$b$  = Burger's vector

$\nu$  = Poisson's ratio

$r_0$  = cut-off radius of dislocation core

$\lambda_s - 2r_s$  = Mean interparticle separation on the slip plane

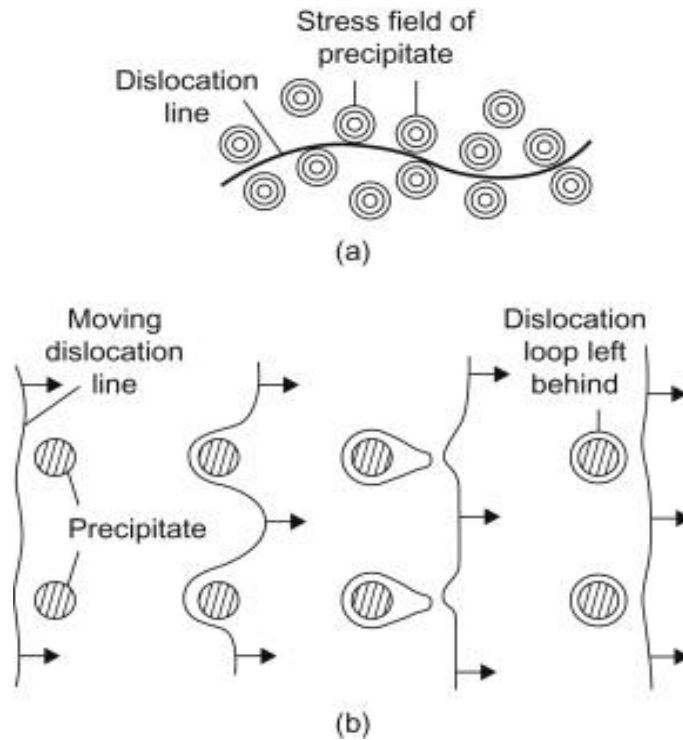


Figure.2.4: Oxide dispersoids acting as obstacles for the dislocation line [60].

The dislocation line continues to bend around the particle according to the Orowan mechanism until it is enclosed completely and the dislocation can move on, leaving a dislocation ring around the bypassed particle. Coherent particle is mainly sheared by the location, whereas incoherent particles are subject to strength of the particle. Shearing stress increases with an increase in dislocation radius. Therefore, it cannot become greater than the Orowan stress as the dislocation then requires less energy to bow out between precipitates. Thus, for the same type of particle, resistance depends on the precipitate's diameter, i.e. the particle size.

## 2.3 ODS Steel Powder Manufacturing

### 2.3.1 Mechanical Alloying (MA)

The most commonly employed method for making ODS steel powder is by MA. Here, the elemental powders, along with the nano-scale oxides are enclosed in a chamber filled with a fixed ball-to-powder ratio (B.P.R) (Figure 2.6) for a fixed duration to get a homogeneously alloyed powder. The fundamental process involves the shearing of the powder particles by the repeated impact of the balls which causes repeated cold welding, fracturing and re-welding of the powder particles for the entire duration [61]. Once the powders are milled together, the powders may be subjected to a hot isostatic process (HIP) or other consolidation processes [62]. One of the advantage of using MA is that metal powder and oxides that chemically would not combine together can be combined using the milling process.

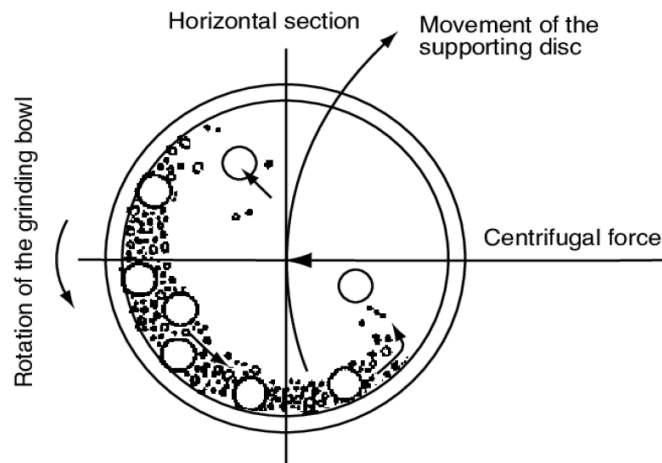


Figure. 2.5: Inside of a ball mill process [63].

There are several models available that define the kinetic shock energy experienced by the powder particles during fracturing caused by the energy which is imparted by the balls upon impact. One of the model is defined by Maurice et al. In their model, they define the powder deformation during collision between two balls as follows [64] -

Equation 2.3 –

$$\alpha(r) = Rv \sqrt{\left(\frac{\rho_b}{H_v}\right) - \frac{r^2}{R}}$$

Where –

R = distance from center of impact

r = radius of the balls

v = relative velocity of the balls at impact

$\rho_b$  = density of the grinding balls

$H_v$  = powder density

Another important factor that can affect powder deformation as identified by Maurice et al. is the powder hardness. Powder hardness can determine the normal elastic force acting to separate the particles during cold welding. The deformation strain can be found by the following equation [64]-

Equation 2.4 –

$$\varepsilon = -\ln\left(\frac{h_0 - \alpha(r)}{h_0}\right)$$

Where –

$h_0$  = powder coating thickness

As the powders are alloyed together in a container, there is a high risk of contamination (particles breaking off from the container wall due to repeated impact from the balls) being mixed with the powders. Also, depending on the matrix material, if the powder is mixed for a very long time, or at high speed, the cold welding could overwhelm the process, and the particles might agglomerate [65,66].

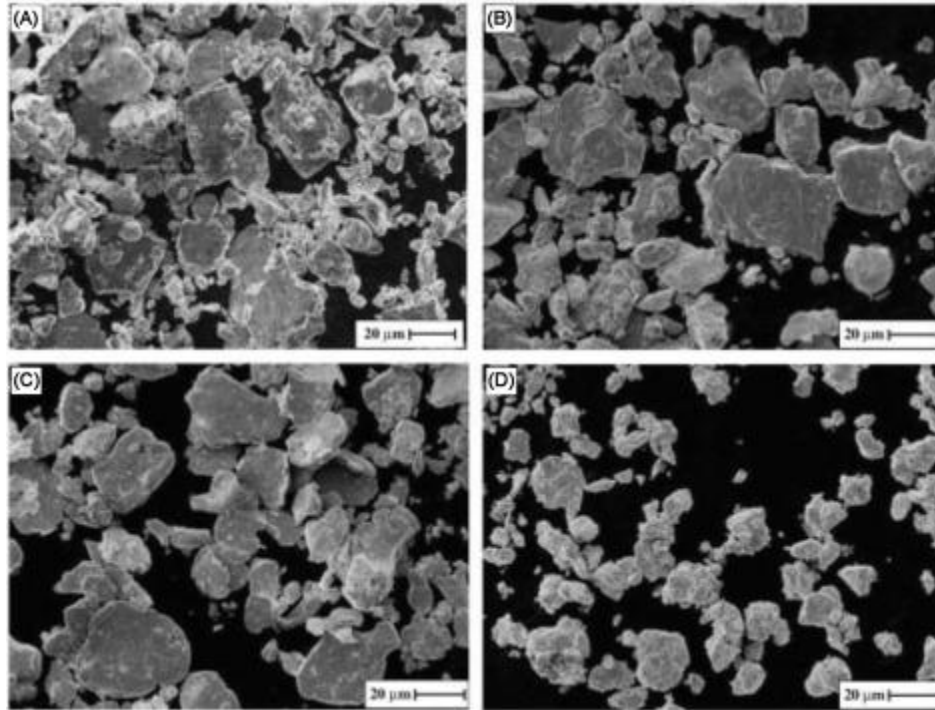


Figure 2.6: Top-Left image is SEM image of as-received bimodal Ti-16Sn-4Nb powder. Bottom- right image is SEM image if powder that were milled for 20 hrs [67].

There are many alloy compositions that can be prepared using MA for example commercially available MA957 (Fe-13.87Cr-1.05Ti-0.3Mo-0.13Ni-0.1Al-0.22Y<sub>2</sub>O<sub>3</sub>) [53], PM2000 (Fe-20Cr-5.5Al-0.5Ti-0.5Y<sub>2</sub>O<sub>3</sub>) [68], Fe-12Cr-1.9W-0.3Ti-0.18Y [69], Fe-13.5Cr-2Al-0.5Ti [70], Fe-9Cr-1Mo-0.25Ti-0.5Y<sub>2</sub>O<sub>3</sub> [71], Fe-9Cr-1W-0.5Y<sub>2</sub>O<sub>3</sub>-0.25Ti [71] , Fe-14Cr-0.22Hf [72]. Either individual elemental alloys or, gas atomized precursor powder can be milled with Y<sub>2</sub>O<sub>3</sub> oxide to create an ODS alloy composition. Several studies have shown that during MA process, the Y<sub>2</sub>O<sub>3</sub> gets dissolved likely due to fragmentation caused by repeated oxide fracture mixing process reducing Y<sub>2</sub>O<sub>3</sub> particles to a sufficiently small particle which then dissolves by repeated dislocation shearing [73–75]. Laurent-Brocq studied the influence of MA on nanoclustering in ODS steel by milling FeCrW+Fe<sub>2</sub>Ti+YFe<sub>3</sub>+Fe<sub>2</sub>O<sub>3</sub> together for 1-144 hrs and noticed progressive incorporation of Fe<sub>2</sub>Ti into the FeCrW matrix. The Fe<sub>2</sub>Ti fragments are stuck

along the crust at first and gradually homogenize into the matrix [73]. APT analysis confirmed a random and homogenous distribution of Ti, TiO, Y and YO after 72 hrs of milling which confirms the presence of Y and O in a solid oversaturated solution which is consistent with other study [73,76–78].

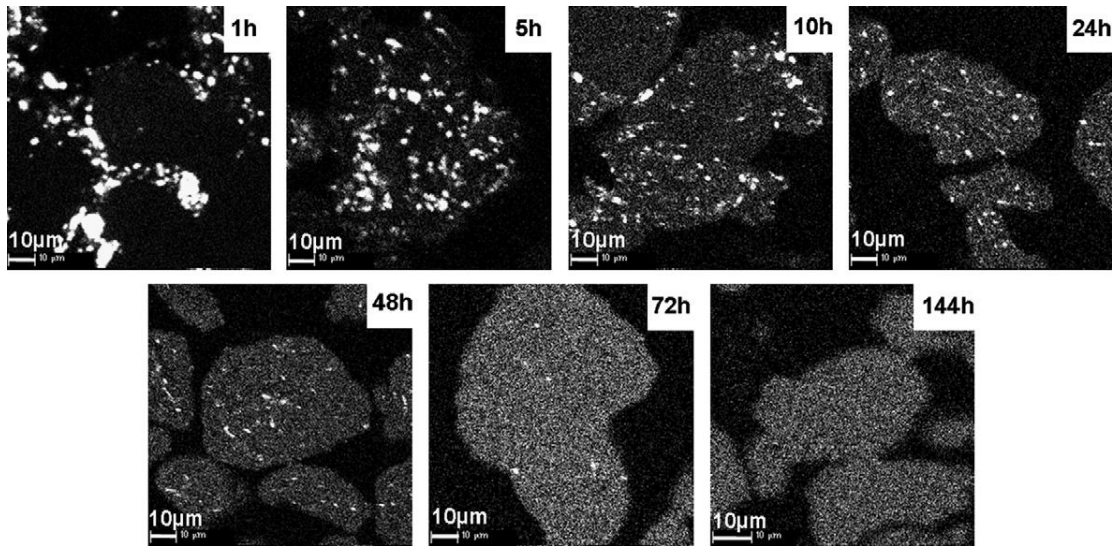


Figure 2.7 : Titanium X-ray maps obtained by EPMA of powder grains resulting from the milling of FeCrW + Fe<sub>2</sub>Ti + YFe<sub>3</sub> + Fe<sub>2</sub>O<sub>3</sub> for different durations of milling [73].

### 2.3.2 Gas-Atomization (GA)

At present, powders for additive manufacturing are most commonly produced with gas atomization [79–81]. Using GA, it is feasible to produce a wide variety of alloys from nearly any base metal element [10,82,83]. In gas atomization, molten liquid metal is melted in a refractory ceramic crucible by induction melting and raised to a superheated temperature. A stream of molten metal is split into fragments from impact by high-energy gas jets as a result from transfer of momentum (generally by non-reactive gasses like argon (Ar) or nitrogen (N)) as the molten metal exits through the orifice of the nozzle [84]. As the fragments fall through the chamber, they then break down into liquid droplets that spheroidize due to the liquid surface tension [85–87]. In GA,

solidification tends to be very fast on the order of  $10^2$  to  $10^7$  K/s for argon gas atomization because of the small particle size [88]. Lawley estimated the spheroidization time of a roughly  $100\ \mu\text{m}$  powder particle to be in the range of  $0.1$  to  $10\ \mu\text{s}$  [89]. Figure 2.8 is an example of a systematic representation of the working of a gas atomizer. The feedstock can either be in molten state or be a solid metal bar/rod that is induction melted [90]. The droplets then rapidly solidify in the cooling chamber. Equations 2.4-2.7 describe the various parameters that can be controlled to dictate the morphology of the powder.

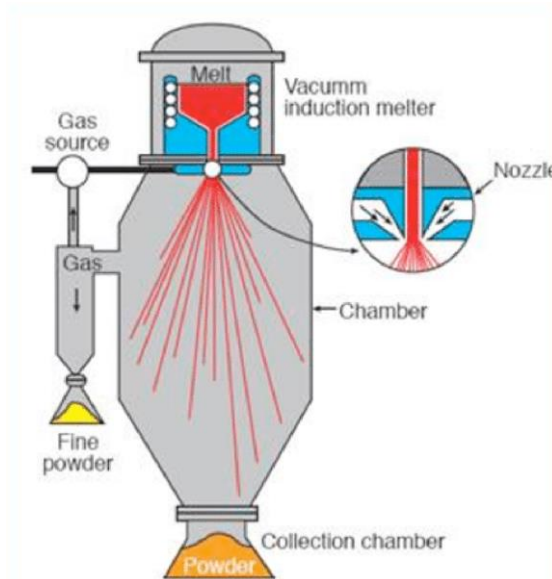


Figure 2.8 : Systematic representation of the working principle of a Vacuum Inert gas atomizer [91].

As is evident from Equation 2.5 - 2.6 listed below, the particle size distribution and the thermal behavior of a droplet can relatively be controlled by gas pressure, gas/melt flow rate (which is governed by orifice diameter), gas composition, and velocity of gas at which it impacts the liquid metal stream [92–94]. The velocity of atomized droplets increases with increasing gas pressure and the thermal behavior of the droplets is controlled by the processing conditions (atomizing gas composition, gas pressure, gas/melt mass flow ratio, melt superheat temperature,

and alloy composition) [95]. These parameters help to dictate the final composition and yield of the final powder size distribution. Anderson et al. were able to use a closed couple GA to achieve a ultrafine (<20  $\mu\text{m}$ ) yield of 32% for Fe-ODS GARS powder by altering the gas flow condition [96]. Park did a set of experiments to GA  $\text{Al}_{10}\text{SiMg}$  alloy powder production by varying orifice diameter, gas pressure and melt temperature and noted that with increase in orifice diameter for a constant pressure and temperature, the mass flow rate increased thus gave a higher yield [97]. Park also noted that for a smaller orifice diameter, the size distribution shifted more towards fine powder [97]. Similarly, for a constant gas pressure and melt flow rate, higher melt temperature gave a higher powder yield but at the same time noted a decrease in yield after a certain temperature as it affected material viscosity [97].

Lubanska demonstrated that the mean particle size  $D_{50}$  of GA metal powder can be predicted through Equation 2.5 and 2.6. In these equations, the viscosity, density, and surface tension for a given metal are constant at a predetermined atomizer melt temperature and stream diameter [93,94]. Therefore it can be observed that the mean particle size  $D_{50}$  is influenced by the gas velocity and gas/melt mass flow rate [93].

Equation 2.5 :

$$D_{50} = Kd \left( \left( 1 + \frac{\dot{m}_L}{\dot{m}_G} \right) \frac{v_L}{v_G w_e} \right)^{\frac{1}{2}}$$

Equation 2.6 :

$$\text{We} = \frac{\rho_L U_G^2 D}{\sigma} \text{ (Webber equation)}$$

Where –

$d$  = melt stream diameter

$\dot{m}_L$  and  $\dot{m}_G$  = mass flow rate of liquid metal and gas

$v_L$  and  $v_G$  = Kinematic viscosity of melt and gas

$\rho_L$  = melt density

$U^G$  = gas velocity

$\Sigma$  = melt surface tension

$K$  = empirical constant (between 40 and 50)

Perez-de León et al. demonstrated through Equation 2.7 that the thermal behavior of the droplet can be affected by factors such as gas pressure, gas/melt flow rate, droplet size and composition [92].

Equation 2.7:

$$\dot{T} = \frac{6f_r(T_{\text{melt}} - T_{\text{Gas}})h}{c_{pd}d\rho_m}$$

Where –

$\dot{T}$  = cooling rate of the droplet in Kelvin

$f_r$  = consideration of gas/melt flow rate

$T_{\text{melt}}$  = droplet/melt superheat temperature in Kelvin

$T_{\text{Gas}}$  = temperature of the ambient atomization gas in Kelvin

$h$  = convective heat transfer coefficient between a droplet and atomization gas

W/(m<sup>2</sup>\*K)

$C_{pd}$  = specific heat capacity (J/(kg\*K))

$d$  = droplet size diameter in meter

$\rho_m$  = density of droplet/melt (kg/m<sup>3</sup>)

There are many different ways to produce metal powder particles using gas atomizers. This section focuses on the GA process and its relevance to the present work.

### 2.3.3 Gas Atomization Reaction Synthesis (GARS)

Although MA-based ODS steel alloys have been commercially available for decades, processing challenges have caused negative impact in their widespread adoption [29,98]. Several studies have sought to address this gap by developing alternative processing methods to incorporate nano-scale oxide dispersoids in steels. Rieken et al. at AMES lab explored GARS to synthesize ferritic Fe-Cr steel by exposing the surface of molten metal droplets to a reactive atomization gas (e.g. – Ar+ ~2000ppm O<sub>2</sub>) and rapidly solidifying the droplet [9]. In the GARS process, all of the elements in the ODS alloy are melted and homogenized together in the refractory crucible. Upon atomization and rapid solidification, the Y is either trapped in solution as elemental Y at the grain boundaries or as a stable Fe<sub>17</sub>Y<sub>2</sub> intermetallic [10]. During atomization, the addition of oxygen to the argon stream promotes the formation of metastable oxide crust rich in chrome [9,10]. Figure 2.9 depicts the GARS process. During subsequent solid state hot consolidation processes like HIP or extrusion, the Cr-rich oxide crust dissolves and the oxygen reacts with Y to form a fine dispersion of stable, nano-scale Y-oxides (Figure 2.10) [9]. Reiken refers to the Cr-O shell as a chemical reservoir for the formation of downstream oxides [9,10]. Using this process, most of the powder size particles were found to be spherical. Rieken also observed that the oxygen content associated, varied with the powder size with the scale inversely proportional as the surface area to volume ratio increases [11].

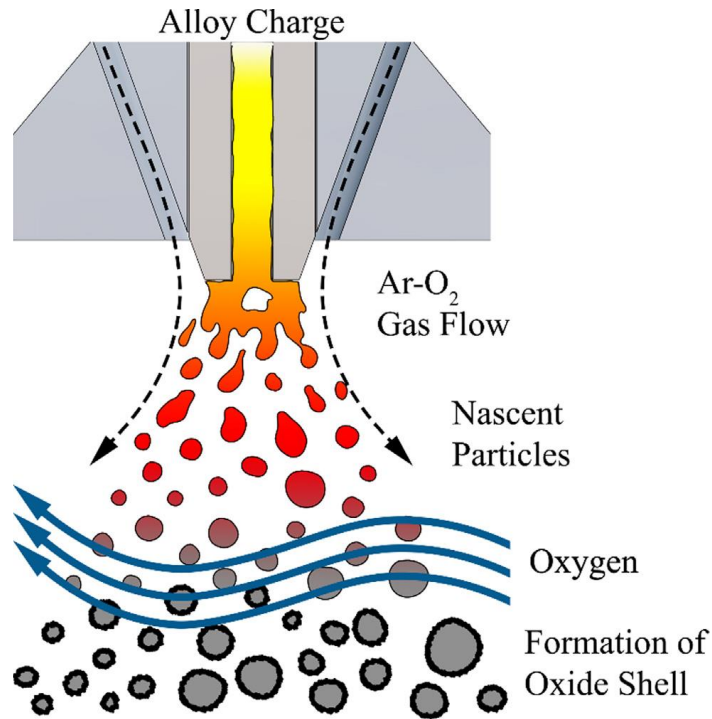


Figure 2.9: Illustration showing the atomization of the GARS powders [99].

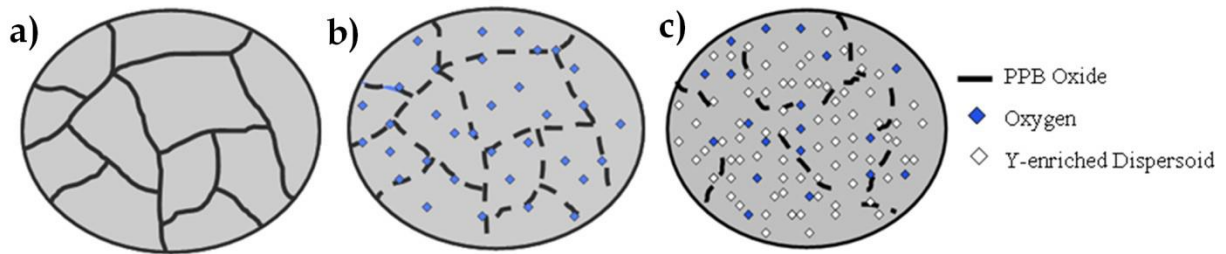


Figure 2.10: The ODS microstructure evolution during hot consolidation of GARS precursor powder: a) initial low-temperature consolidation showing intact PPBs, b) dissociation of the PPBs (simulating heat treatment) and O diffusion into the  $\alpha$ -(Fe,Cr) matrix, and c) formation of Y-enriched oxide dispersoids throughout the microstructure [9].

Because GARS powder is atomized from the liquid melt, the cross-contamination that is commonly encountered in MA is minimized. Additionally, solidification in freefall results in nearly spherical powders that exhibit good flowability. This is an important factor for supplying powder to any number of manufacturing processes but especially in additive manufacturing

where layer/powder bed formation and consistency is critical. The oxygen for oxide formation is delivered from the oxide crust. The amount of oxygen available can be varied during the surface oxidation process.

#### **2.3.4 Surface Treatment of gas Atomized powder followed by Reactive Synthesis (STARS)**

Gil et al. developed a ferritic Fe-Cr ODS powder processing method called surface treatment of gas atomized reaction synthesis (STARS) [29]. In the STARS method, a metallic Fe-Cr oxide rich surface is created by atomizing the powder using just argon to split the liquid metal, followed by controlled HIP and heat treating of atomized powder in the presence of oxygen [100]. During heat treatment, the metastable oxide layer formed at Prior Particle Boundary (PPB) during HIP diffuses inside ferritic grains to react with the dissolved Y and Ti, resulting in Y-Ti-O precipitates [29,101]. Care is required during HT To avoid detrimental effects to the final microstructure, such as a change in grain structure and or induction of thermally induced porosity. Gil et al reported a heterogenous ferritic grain size and yttrium rich precipitation at grain boundaries of as atomized powder but noticed the formation of thermally induced porosity (TIP) and presence of Ti (C,N) phases post HT at 900C [101].

The main differentiating factor between GARS and STARS lies in the atomization process. While GARS exposes the liquid metal droplets to a reactive Ar-O<sub>2</sub> gas at higher temperature, in the STARS method, the powder is oxidized at lower temperatures [102].

## **2.4 Consolidation Methods for ODS powders**

### **2.4.1 Hot Isostatic Process (HIP)**

ODS alloys are most commonly produced by MA of nanoparticles of yttrium-oxide ( $Y_2O_3$ ) with metal matrix powders often containing Fe, Ni, Cr, Al, Y, and or W [103]. The powders are then processed into the final shape with various powder metallurgy methods including HIP followed by thermomechanical or thermal treatment to achieve desired grain structure and mechanical properties [104]. HIP also helps achieve densification of powder which helps remove trapped gas pores that were created during gas atomization or MA.

In conventional HIP techniques, the powder container is typically heated by radiation from the enclosing furnace through external heating elements and convection of inert gases. The sample is heated as a consequence of the heat transfer occurring by conduction from the external surface of the container to the powders. As during HIP, heating causes the material to undergo a plastic deformation to reduce porosity, the powder are stored in a contained. The consolidated powder take the shape of the container which, can then be extruded or hot rolled to give it a final shape.

Components produced by HIP have high-temperature creep resistance [105–107] and corrosion resistance. Figure 2.11 is a representation of a typical HIP process. Samples after HIP can be hot rolled extruded into tubes, sheets or bars.

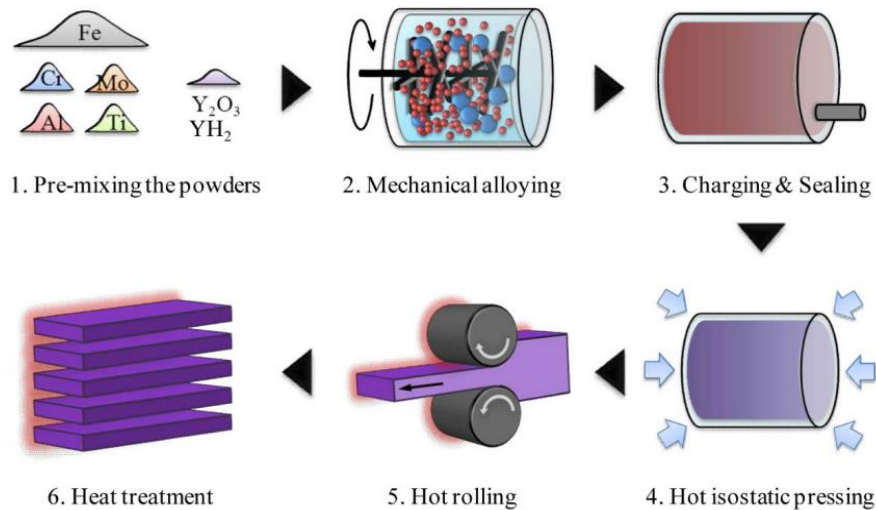


Figure 2.11: Typical process map for HIPed samples [108].

## 2.4.2 Friction stir welding (FSW)

Friction stir welding makes use of friction generated by a rotating tool to plasticize the metals and then fuse them together to form a joint without melting the metal alloys (Figure. 2.12). The two alloy plates are joined together and held together by a fixture. The rotating tool pin lays perpendicular to the two connecting plates and is held in place for a certain amount of time while rotating at high velocity to use friction to create heat to plasticize the metals in order to facilitate the joining of the two alloys along the joining/weld line [109].

This method is particularly advantageous while fabricating ODS alloys as high-temperature melt pool generated during conventional welding processes can cause the oxide dispersoids to break down and agglomerate. During FSW, the peak temperature generally does not exceed 70-90% of the melting temperatures of the joining metals [109]. As friction stir welding does not melt the surfaces, the dispersoids are still maintained on the surfaces, which allows the alloys to maintain their physical properties even after fusing together [78,109,110]. The

microstructure can also be customized to be similar to the joining metals by changing process parameter.

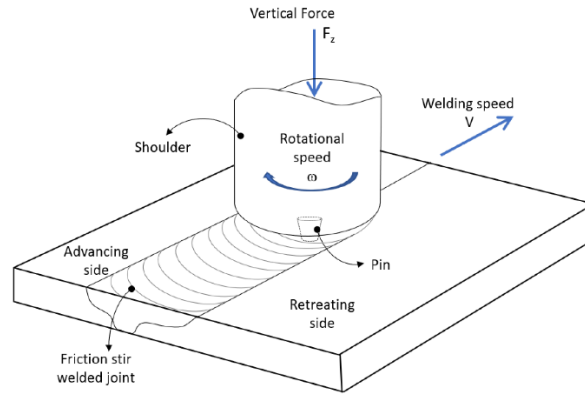


Figure. 2.12: A schematic representation of a typical FSW process used to weld two ODS plates together while a rotating tip is plasticizing the two metals to fuse them together [111].

### 2.4.3 Spark Plasma Sintering (SPS)

Spark Plasma Sintering (SPS) is a sintering process in which an electric current runs directly through powder in a mold [112]. Samples produced using this method are generally manufactured under vacuum and are sintered to a desirable temperature to influence the densification of the powder and get the desired microstructure [113]. Rapid heating and short process times can be achieved by this method. The heating rate during SPS process depends on the geometry of the container, powder's thermal and electrical properties, and on the electric power supplier. Due to rapid heating and short processing times, the grain growth is suppressed which might not be desirable as it affects the mechanical properties [114]. Compared to HIP, heating rates of SPS can be as high as 1000 °C/min, which reduce the processing time depending on the material and process container [76]. XRD and TEM analysis of as fabricated samples proved the presence of stable  $Y_2Ti_2O_7$  oxide [76].

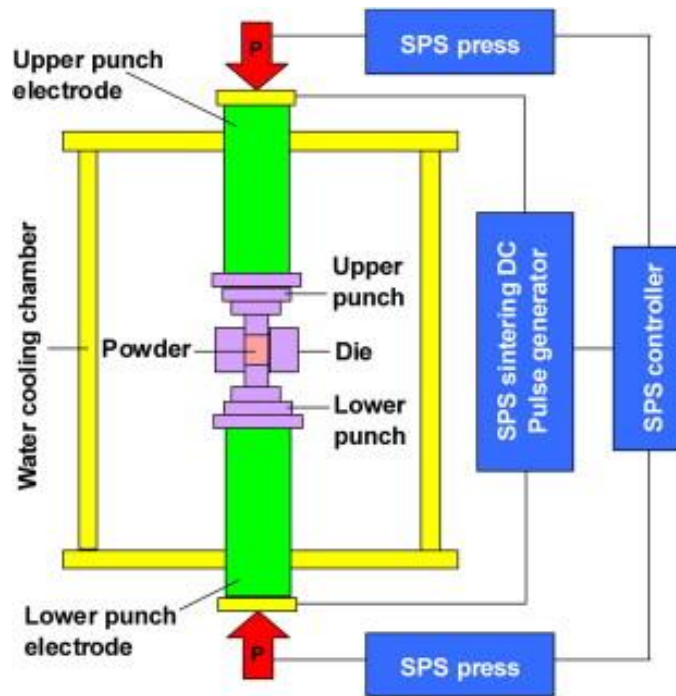


Figure 2.13: Schematic representation of a SPS system [113].

Studies by Ponraj et al., Franke et al., Rajan et al., Karak et al. have shown that ODS samples produced by SPS have high density, high micro hardness values [71,76,77,115] over samples produced conventionally by HIP. Franke et al. compared the mechanical properties of samples with and without oxides produced by SPS and noticed an increase in hardness values as well as UTS with increase in milling and oxide concentration [115].

#### 2.4.4 Shear Assisted Processing and Extrusion (ShAPE)

Also known as friction stir scribe process for joining dissimilar materials is a process of joining dissimilar materials or powders and, was developed at Pacific Northwestern Lab (PNNL) [116–118]. This process uses a machine to spin billets or chunks of bulk metal alloys, creating enough heat through friction to soften the material so it can be extruded through a die to form tubes, rods and or channels. Unlike conventional processes, this method uses a fraction of the

energy needed to extrude material through the die. This benefit enables the production of smaller machinery to produce parts. Samples with diameter as small as a few millimeters to a length of a few centimeters can be produced using this method [119,120].

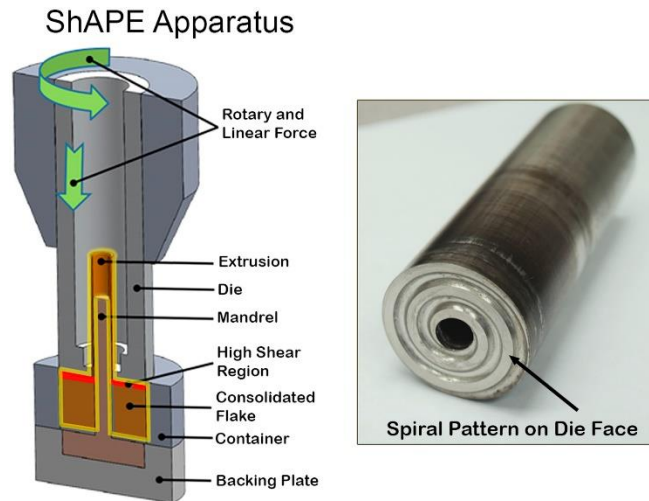


Figure 2.14: Schematic representation of a typical ShAPE apparatus [119].

Croteau et al, Overman et al, Li et al, Komarasamy et al have observed that through ShAPE fabrication, finer microstructural grains can be obtained as compared to the microstructure of before extrusion specimen [119–122]. These fine grains have been reported to be typically uniform throughout the sample thus providing greater strength and ductility. Li and Grant et al., have fabricated copper graphite composite structures like wires using the ShAPE process and have observed void free structures with uniform microstructure and homogenized dispersion of graphite within the microstructure. They have also reported smaller average grain size and smaller maximum grain diameter with a higher vickers hardness ,yield stress and elongation of samples produced using ShAPE as opposed to using billets produced using hot extrusion [123,124].

### 2.4.5 Additive Manufacturing

Conventional techniques such as friction stir welding, extrusion, SPS, ShAPE produce small scale billets or rods of material that must be machined or joined into a final geometry. AM however, presents the possibility of directly fabricating customized near net-shaped manufacturing. However, on the surface, AM is not an intuitive choice because ODS steels are generally considered difficult to weld due to the potential for slag-off, agglomeration, and the propensity for small oxide precipitates to coarsen or leave the weldment during joining [125–127]. Nevertheless, the small local melt volume coupled with relatively high cooling rates associated with laser powder bed fusion (LPBF) AM has inspired several research efforts with compelling results. Table 2.1 highlights several properties of interest that have been generated for ODS steels produced by AM, when such details are reported in the literature across common AM processes of LPBF, electron beam powder bed fusion (EB-PBF), and directed energy deposition (DED). While the details in Table 2.1 vary significantly, the studies reported share common features, including the presence of larger oxide particles, inclusions, or agglomerates that, coupled with AM defects, in general limit the expected mechanical properties.

Additive Manufacturing has been widely used in recent years to manufacture ODS alloys due to the ability to control solidification and cooling rates. Capabilities of LPBF and DED as suitable alternatives have been showed in various studies [128–131]. It has been widely speculated, but never explicitly shown, that due to localized heat input (which can be varied by changing process parameters such as beam or scanning speed, hatch spacing, energy/power, beam spot size, raster pattern etc. along with strong Marangoni forces caused by different thermal gradient coefficients and surface tension in the molten melt pool, a constant stir of the liquid occurs which helps in a homogenous oxide dispersion as the molten pool rapidly solidifies [129,132,133]. Another advantage is grain structure. It has been reported by multiple studies that due to successive

re-melting of previous layers, grain structures tend to grow/elongate along the epitaxial direction as the part orientation in Z-axis [129,130,132,134]. Buendia et al. reported smaller grain size and a homogenous distribution in the LPBF samples, which was observed to be a key factor for enhanced mechanical properties [135]. Zhong et al. also reported a similar observation where-in they reported high oxide density and high density of nano-structured precipitates along the grain boundary of the alloy matrix, which they attributed to be the dominant strengthening mechanism and estimated irradiation sink for high Cr steels [128].

Nevertheless, where TEM analyses are reported, nano-scale oxides of various phases are prevalent, with median diameters ranging from  $< 10$  to  $> 100$  nm. Early studies utilized established or commercially available compositions of powders such as PM2000 [126,136], 14YWT [137], or MA956 [138] in LPBF processes. Notably, very little research has focused on the optimization of the process parameter space, as shown in Figure. 2.15, the reported process window for LPBF of dense structures is comparable to that of the austenitic stainless steels that are routinely used in AM [139,140]. Other groups have blended, milled, or mechanically alloyed oxide particles with steel precursor materials for LPBF processing [141–149]. Recently, Zhang et al. used MA to introduce 0.3 wt%  $Y_2O_3$  and 0.3% Ti of 316L powders which were then consolidated with LPBF [150]. Using laser DED, Shi et al. produced samples of Fe-9Cr-1.5 W-0.3Ti-0.3Y from MA powders. The samples exhibited high UTS (794 MPa) and small average oxide size (21.9 nm), which was improved after hot isostatic pressing (HIP), and were 1046 MPa and 13.3 nm, respectively. Morrow et al.[151] found 20–280 nm size inclusions in as-built test samples produced by AM 304 and 316 L using DED and LPBF. Saeidi et al. [152] identified spherical Cr-silicate (mainly of Si and O) spheres roughly 50 nm in diameter throughout the material. A

distribution of larger oxides with median diameters of hundreds of nanometers to tens of microns, e.g., Eo et al., 312–485 nm, and Song et al., 271–1896 nm are also reported [153,154].

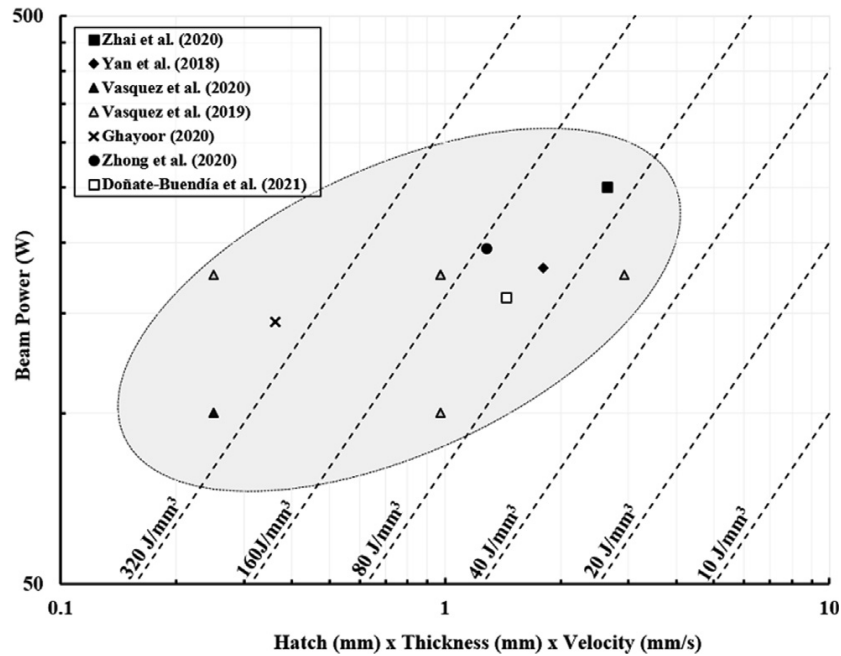


Figure 2.15: Schematic process map representation of energy density plot obtained from literature review [99].

While these compiled data from the various literature suggest that, with further development, L-PBF AM may become a workable alternative for producing bulk ODS steel components, the feedstocks used in these studies have still typically depended on MA processing, which, as discussed, is a major limiting factor to the potential scalability of ODS steels. Recent findings in the literature review have corroborated the premise that careful alloy design could leverage a pathway for selective oxidation of yttrium to form more desirable nano-scale oxides in-situ, in the liquid phase, and within the LPBF AM melt pool.

In order to mitigate some of the limitations of ODS fabrication, in the present study, the potential of fabrication through GARS and LPBF has been explored. Both the precursor GARS powders and the LPBF samples were characterized to assess the effectiveness and limitations of LPBF processing as a means to bypass the MA process step typical of ODS steel materials.

Table 2.1: Literature review of existing research additive manufacturing using ODS powder [99].

Ref.	AM Process	Alloy	Wt. % Oxide	Oxide size d50 (nm)	Test temp. °C	$\sigma_{UTS}$ (MPa)	$\sigma_{Yield}$ (MPa)	Hardness <sup>a</sup>
Walker et al. [126]	LPBF	PM2000	0.5	48.4 ± 25.2	—	—	—	—
Hunt et al. [138]	LPBF	MA956	0.3–0.7	—	RT	660	—	—
Gao et al. [142]	EB-PBF	Fe18Cr2W0.5Ti + Ball Milled Y <sub>2</sub> O <sub>3</sub>	0.3	18.05	RT	1371	—	—
Vasquez et al. <sup>c</sup> [143]	LPBF	Fe14Cr1W0.3Mn0.3Si0.2Ni + Ball Milled Y <sub>2</sub> O <sub>3</sub> + TiH <sub>2</sub>	0.3	>35	—	—	—	189 HV
Vasquez et al. <sup>c</sup> [144]	LPBF	Fe14Cr1W0.3Mn0.3Si0.2Ni + Ball Milled Y <sub>2</sub> O <sub>3</sub> + TiH <sub>2</sub>	0.3	—	—	459	—	—
Zhong et al. <sup>c</sup> [145]	LPBF	316L + MA Y <sub>2</sub> O <sub>3</sub>	—	37	RT	637	574	—
					250	476	456	—
					400	447	420	—
Ghayoor et al. [146]	LPBF	304L + MA Y <sub>2</sub> O <sub>3</sub>	5	<100	—	—	—	296 ± 12 HV
Ghayoor et al. [147]	LPBF	304L + MA Y <sub>2</sub> O <sub>3</sub>	0.5	—	RT	700	575	—
Ghayoor et al. [148]	LPBF	304L + MA Y <sub>2</sub> O <sub>3</sub>	0.5	968	RT	700	575	350 ± 12 HV
Paul et al. [155]	LPBF	304L + Inkjet Y-Si-O	—	—	RT	586	695	272 ± 6 HV
Chang et al. [149]	LPBF	Fe14.4Cr1.8 W0.3Ti0.1Mn0.05C + Ball Milled Y <sub>2</sub> O <sub>3</sub>	0.5	35 ± 15	—	—	—	—
Boegelain et al. [136]	LPBF	PM2000	0.5	—	—	465	430	—
Doñate-Buendía et al. [141]	DED	Fe21Cr4.67Al0.47Ti + Y <sub>2</sub> O <sub>3</sub> Blended	0.08	100	RT	—	—	240 HV0.1
		Fe21Cr4.67Al0.47Ti + YIG Blended	0.08	100	RT	—	—	230 HV0.1
Doñate-Buendía et al. [156]	DED	PM2000	0.08	—	RT	—	—	223 ± 9 HV0.1
	LPBF	PM2000	0.08	—	RT	—	—	247 ± 8 HV0.1
Doñate-Buendía et al. <sup>c</sup> [135]	DED	PM2000	0.08	50	RT/	—	—	222 ± 9 HV0.1
	LPBF	PM2000	0.08	30	RT/	—	—	249 ± 7 HV0.1
					600 <sup>b</sup>	—	—	—
Shi et al. [157]	DED	Fe-9Cr-1.5 W-0.3Ti-0.3Y MA	0.3	21.9	RT	794	—	339
			0.3	13.3	RT	1046	—	347
			0.3	21.9	600	461	—	—
				13.3	600	592	—	—
Shi et al. [158]	DED	Fe-15Cr-2 W-4.5Al-0.3Ti-0.3Zr-0.3Y MA	0.2	—	RT	370	—	—
			0.2	—	RT	410	—	—
			0.2	<10	RT	490 <sup>c</sup>	—	—
			0.2	<10	RT	525 <sup>c</sup>	—	—
Zhang et al. <sup>c</sup> [150]	LPBF	316 L + 0.3 + Y <sub>2</sub> O <sub>3</sub> + 0.3Ti	0.3	45	—	—	—	—

## CHAPTER 3

### 3.1 Introduction

The preliminary proof of concept for this thesis was performed using GARS powder that was produced by Dr. Iver Anderson's group at AMES lab. This batch of powder composition, referred to by its AMES designation as Cr-166, was previously studied by Reiken [9] for its application in HIP processing. This batch was chosen for the present LPBF trials not only for its availability but also because the LPBF results could be directly compared to the previous HIP study. Approximately 200g of powder from this batch, Cr-166, was provided.

Prior to LPBF consolidation, characterization of the Cr-166 powder was carried out. The bulk elemental composition of the powder shown in Table 3.1, was determined by inductively coupled plasma mass spectrometry (ICP-MS). The oxygen content was determined by inert gas fusion (LECO ONH 836) referencing ASTM E1019 for steels.

Table 3.1: Chemical composition in wt.% of the powder feedstock by ICP and inert gas fusion.

Fe (wt%)	Cr	Y	Ti	O (ppm)
bal	14.99	0.15	0.10	410*

Additionally, the size, morphology, composition, and structure of the powder was characterized to better understand its influence on downstream LPBF processing. A Microtrac S3500 laser diffraction particle analyzer utilizing a wet method with ultrasonic agitation was used for particle size distribution measurement. The powder morphology was observed on a JOEL 6010LA scanning electron microscope (SEM) with electron dispersive spectroscopy (EDS). The particle size was measured by laser diffraction and showed a volume distribution of 24-49  $\mu\text{m}$  (for the 10th and 90th percentile, respectively) and a median size of 33  $\mu\text{m}$  shown in Figure 3.1. The

distribution exhibited a limited number of fines, which is typical of this size distribution commonly used for laser powder bed fusion feedstock.

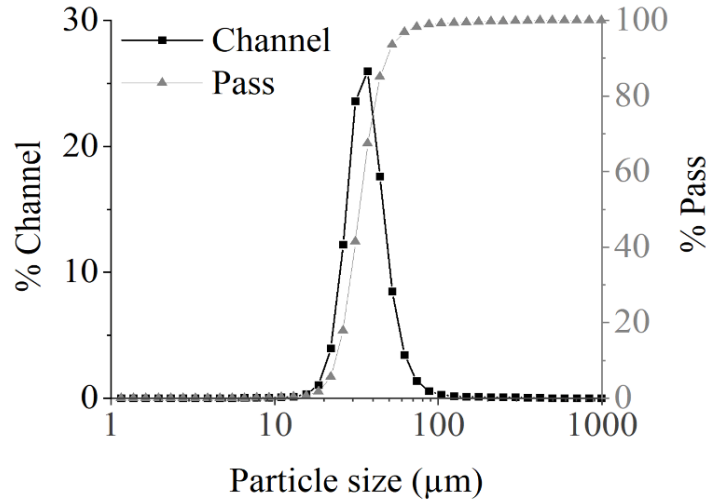


Figure 3.1: Histogram showing the volumetric powder size distribution measured by laser diffraction [99].

Figure 3.2 shows a compilation of backscatter SEM images in compositional mode (BEC) of the as-received and unused GARS powder. The observed morphology is typical of gas atomized powders with a mixture of spherical particles and ovals without a significant fines fraction. The images show no observable inhomogeneity with a small number of satellites and dimples, similar to those previously reported [9], where the surface oxide formation tended to discourage smaller-scale satellite particles. While these small features were occasionally observed in the starting powder, most of the Y is expected to be intermetallic  $\text{Fe}_{17}\text{Y}_2$

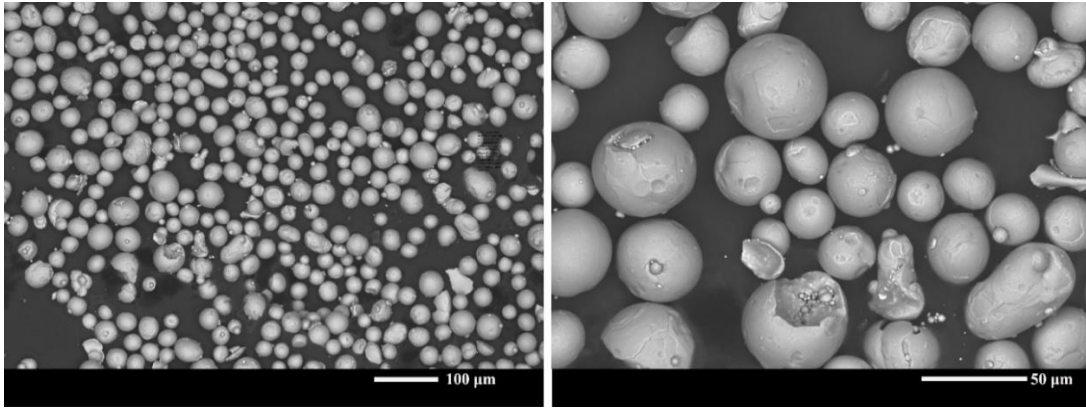


Figure 3.2: Backscatter SEM images in compositional mode of the Cr-166 feedstock prior to use in LPBF.

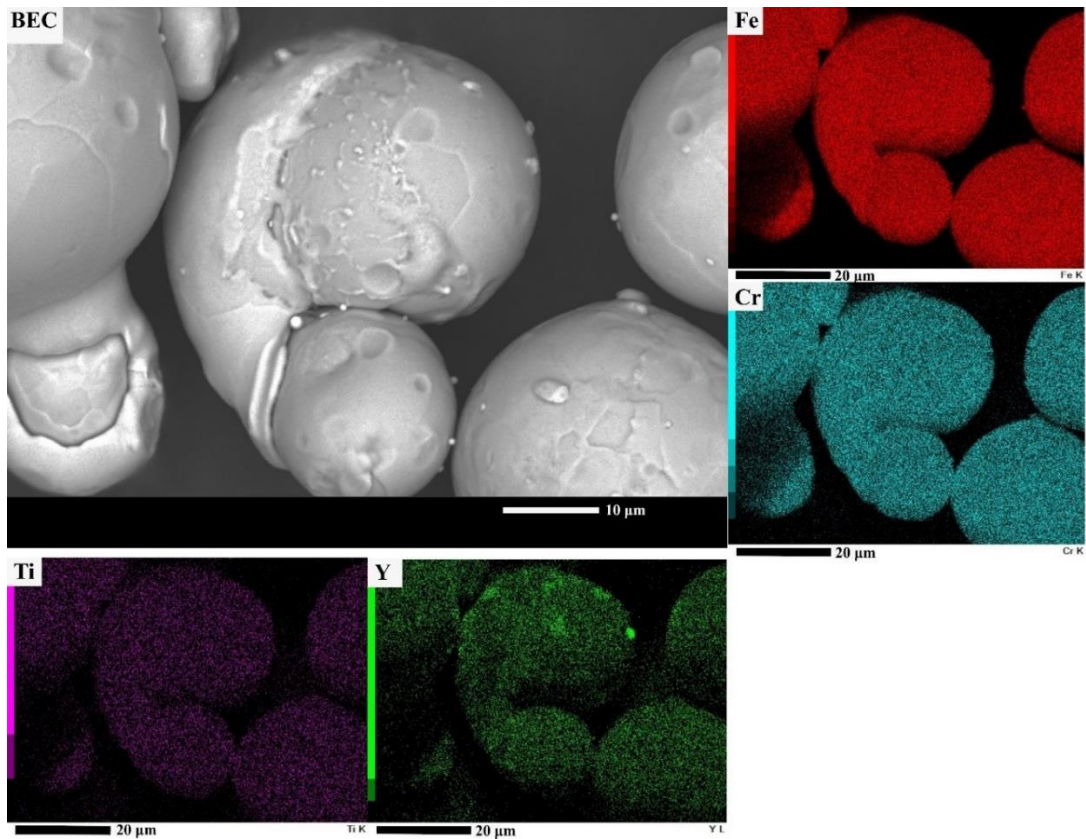


Figure 3.3: BEC microscope image of typical GARS powder showing a predominant Cr-Fe shell with small regions of oxides rich in Yttrium and Titanium

Figure 3.4 and 3.5 shows an image of a cross-section of the powder produced with gallium ion contrast imaging which generally shows isotropic grain sizes in the range of 1 – 20 µm.

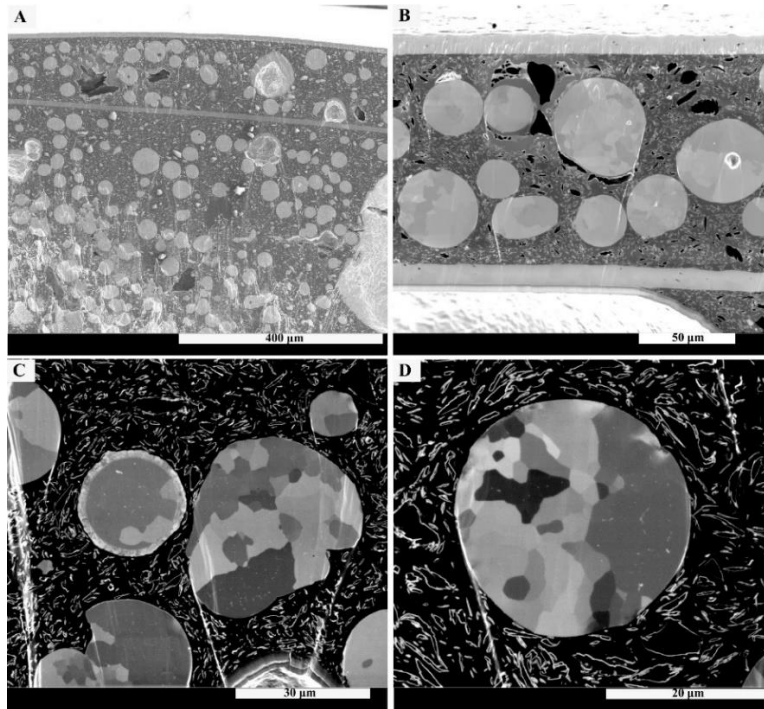


Figure 3.4: Gallium Ion contrast image of a cross-section of representative Cr-166 GARS powder particle at 200 X(A), 1500 X(B), 3500X (C) and 6492X (D) magnification.

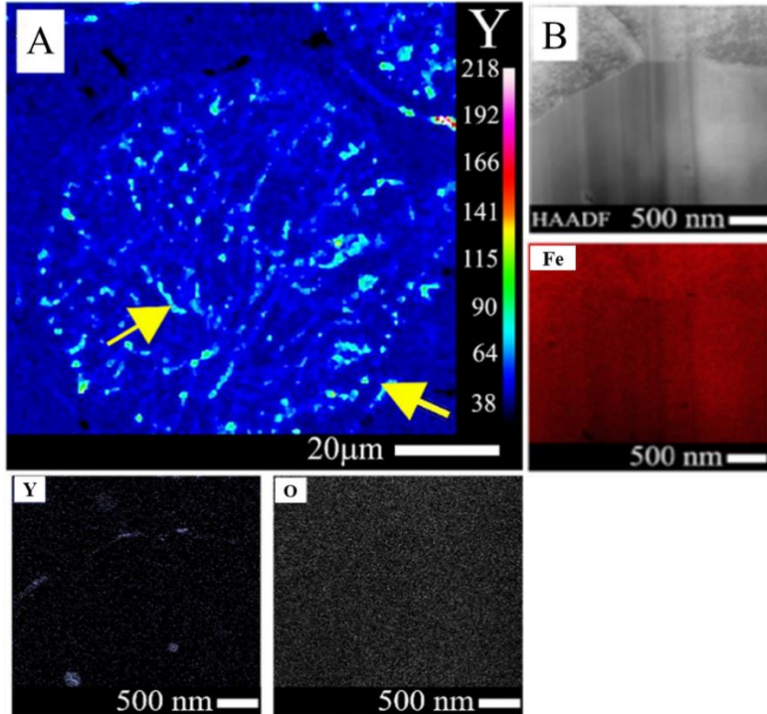


Figure 3.5: EPMA chemical map of a Gallium Ion contrast image of a cross-section of representative GARS powder particle showing presence of elemental Yttrium indicated by yellow arrow (A), STEM HAADF and EDS images of regions rich in yttrium and iron near grain boundaries (B) [99].

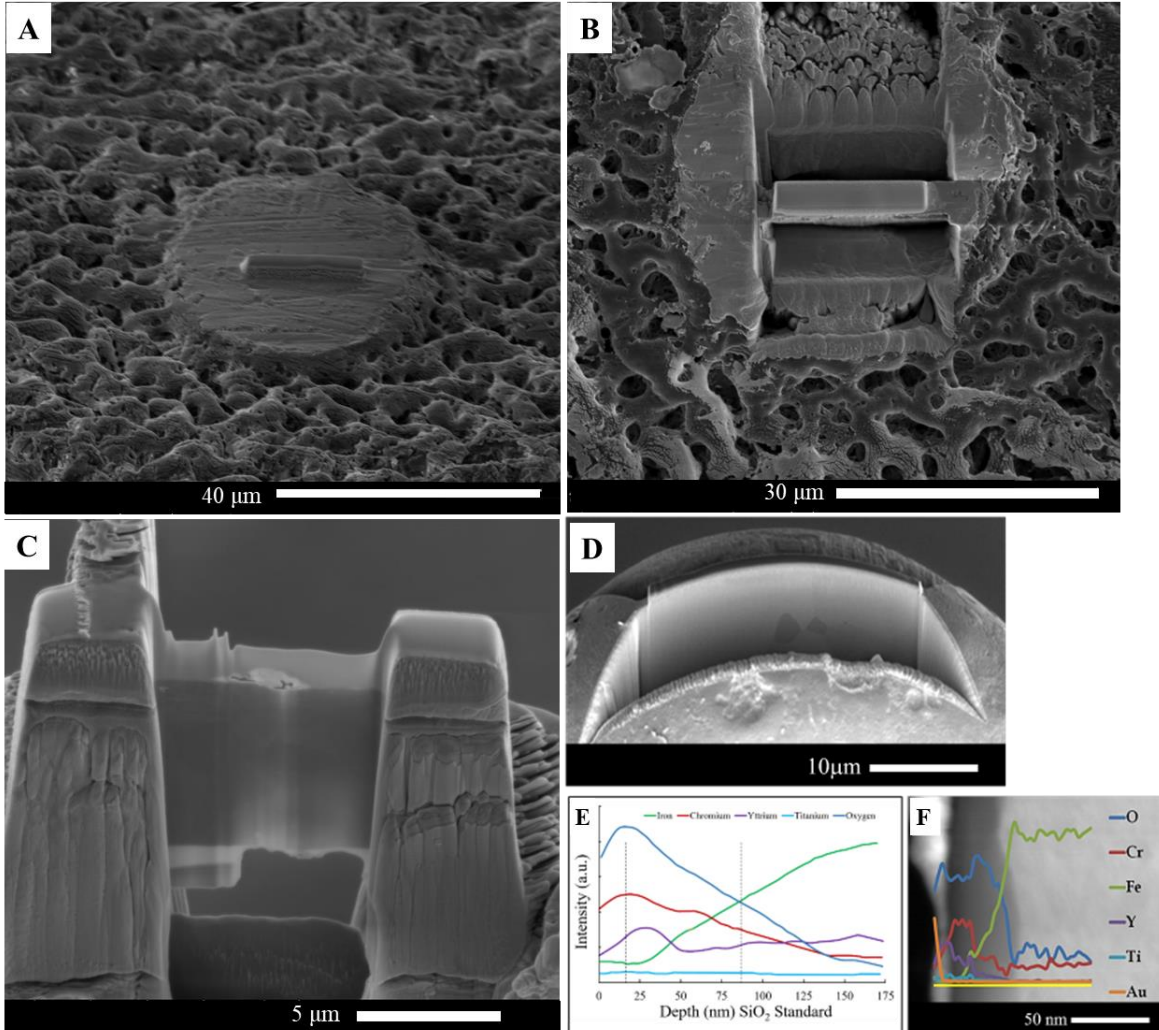


Figure 3.6: FIB cross-section of a GARS power particle (A-C), FIB cross-section of the surface of a 58  $\mu\text{m}$  powder particle during TEM liftout (D), AES depth profile of the surface of a powder particle (E) EDS line scan overlay on a TEM image of a surface oxide (F). Figure D-F analysis was performed by Dr. Rieken on Cr-166 powder as part of his dissertation [9]

Figure 3.6 is a collection of SEM, TEM images of a typical Cr-166 GARS powder. TEM and AES analysis of a 58  $\mu\text{m}$  powder particle revealed the presence of an oxidized surface on the powder that was, generated by AMES lab. Figure 3.6D – 3.6F was performed by Dr. Joel Rieken as part of his dissertation on Cr-166 composition that was created for HIP study and further information on powder properties can be found in his dissertation [9]. Figure 3.6A – 3.6C was performed at NC State at the Analytical Instrumentation Facility (AIF). Figure 3.6E EDS line scan

revealed O and Cr peaks from the crust to a depth of 50nm which was further confirmed by AES data (Figure 3.6F) which was measured from the surface to 175 nm into the matrix showing peaks in O, Cr. As can be seen from both Figure 3.6E and 3.6F, a small amount of Y is observed in both EDS and AES line scan data sets.

### 3.2 Additive Manufacturing Approach with Preliminary Cuboid Designs

A modified concept laser M100R with a 100W Nd:YAG fiber laser at ~1060 nm wavelength and 40  $\mu\text{m}$  spot size, shown in Figure 8A was used to fabricate four (4) test articles with a cross-section of 10 mm x 10 mm upon 90 mm x 90 mm stainless steel build plate. As this was an initial study to check for feasibility, and due to limited availability of powder, a DOE study could not be conducted and as such, parameter for SS 316L were used. Here the laser power was 90W, the beam scan speed was 1500 mm/s, the distance between scan lines, or hatch offset, was 0.080mm, and the layer thickness was 0.020mm, resulting in a nominal volumetric energy of 37.5  $\text{J}/\text{mm}^3$ .

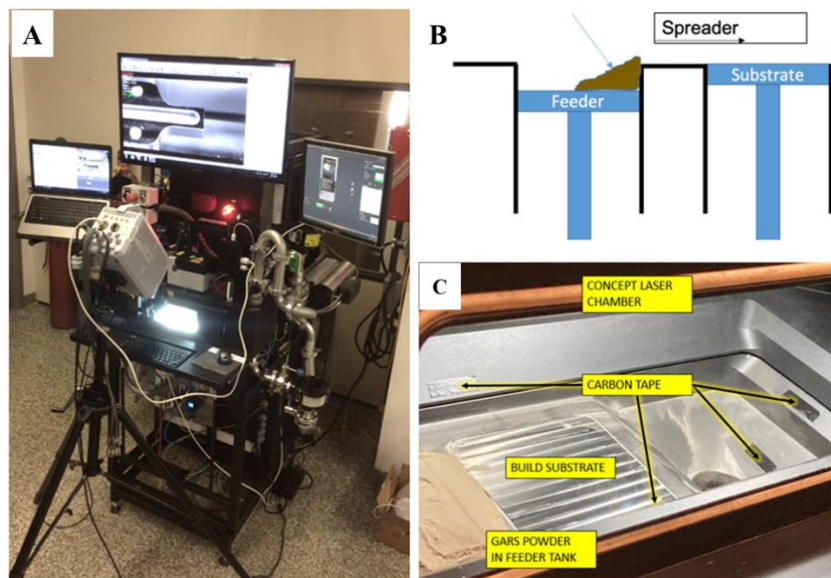


Figure 3.7. Modified Concept laser platform at N.C. State (A), Illustration showing how the GARS powder was loaded into the powder feeder to maximize build height (B) and Photograph of the build chamber showing the setup and location of carbon tape for collecting ejected spatter.

Due to the small volume of powder available (~200g), powder was loaded on the rightmost portion of the feeder tank and the powder spread was limited to 20% of the build area to maximize the sample height (Figure 3.7 B).

Figure 3.8 shows the overall approach for which four atmospheric environments were considered: Ar, Ar+1wt% O<sub>2</sub>, Ar+5wt% O<sub>2</sub>, and air; the gas mixtures were pre-mixed research-grade cylinders provided by Arc3 gasses. For the first 3mm of build height, all four specimens were fabricated with these parameters. The atmosphere in the chamber was argon and was maintained below 0.1% oxygen content. This was monitored by both the system integrated oxygen sensor, but also by a RKI OX-600 oxygen monitor probe inside the build chamber. After 3mm, the process was paused, and the chamber was back filled with a pre-mixed Ar+1% oxygen process gas, and the process was restarted. Sample #1 was turned off, so only three of the samples were continued. After another 3mm this was repeated and the process gas was replaced with Ar+5% O<sub>2</sub>, and building continued for two of the remaining samples. After another 3mm, the process gas was allowed to run in an ambient atmosphere (air, ~21% oxygen) for the final sample, shown in Figure 9B.

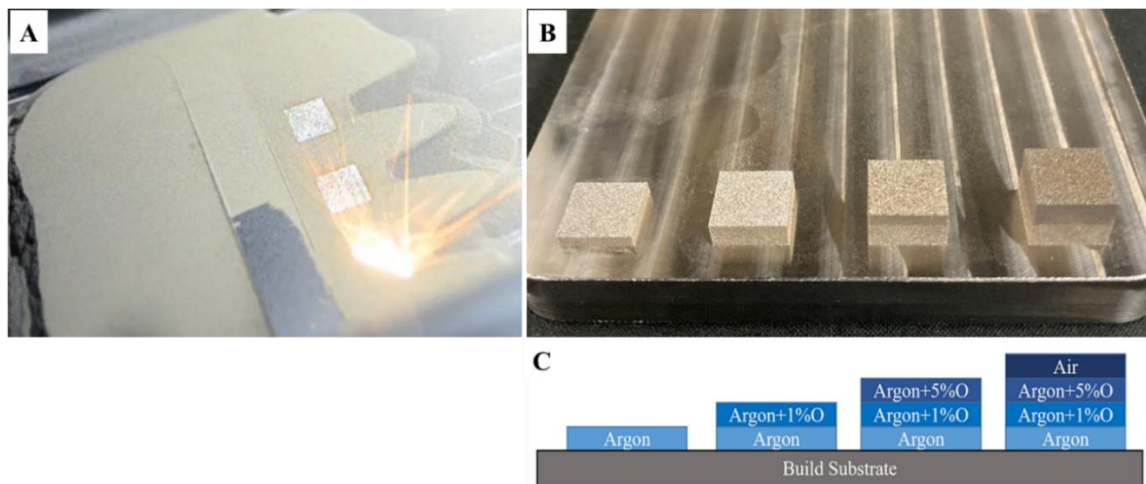


Figure 3.8: Experimental setup showing the Concept Laser M100R sample fabrication (A), composite samples after fabrication produced with 4 different chamber environments (B), and illustration of sample fabrication and atmosphere strategy (C) [99].

It is difficult to explicitly predict how much oxygen will be absorbed in the melt pool with varying LPBF atmospheres, as well as localized compositional variations due to interactions between the top of the liquid pool and the chamber atmosphere; therefore, as a sensitivity test, oxygen was increased in the equilibrium calculation from 1000 ppm wt. - 20000 ppm wt. Representing oxygen disassociated in the liquid pool to view a range of possible oxides.

### 3.3 Results and discussion

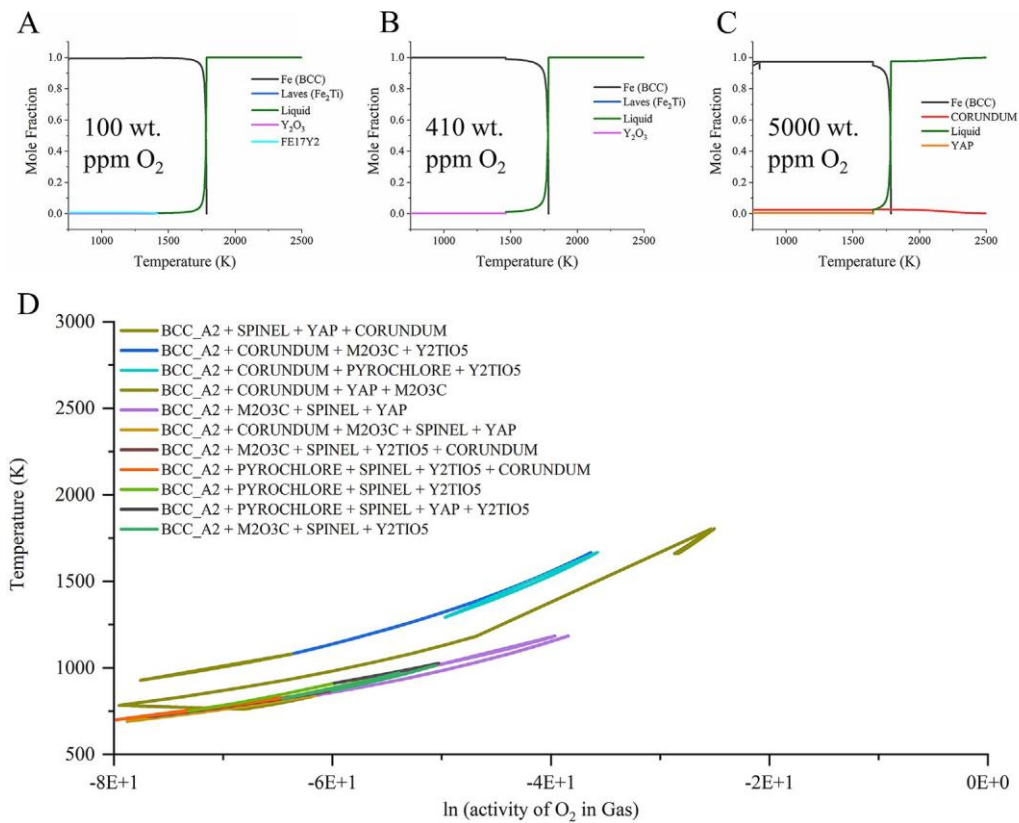


Figure 3.9: Equilibrium thermodynamic results for 100 ppm (A), 410 ppm (B), 5000 ppm (C) and the natural logarithm of oxygen activity (D) at different oxygen concentration [99].

X-Ray diffraction was used to determine phase content in starting powder and fabricated solids in varying oxygen atmospheres (Figure 3.9). The largest peaks in the powder diffractometry are the (110) and (211) planes for Fe at 43.55° and 64.8° for all conditions, with only trace peaks

in comparison. The powder (bottom curve) contains a small peak at  $42.6^\circ 2\theta$ , which is consistent with iron-yttrium intermetallic such as  $\text{Fe}_{17}\text{Y}_2$ . The peak is small and was difficult to refine accurately due to its height compared to the main (111) Fe peak and background noise.

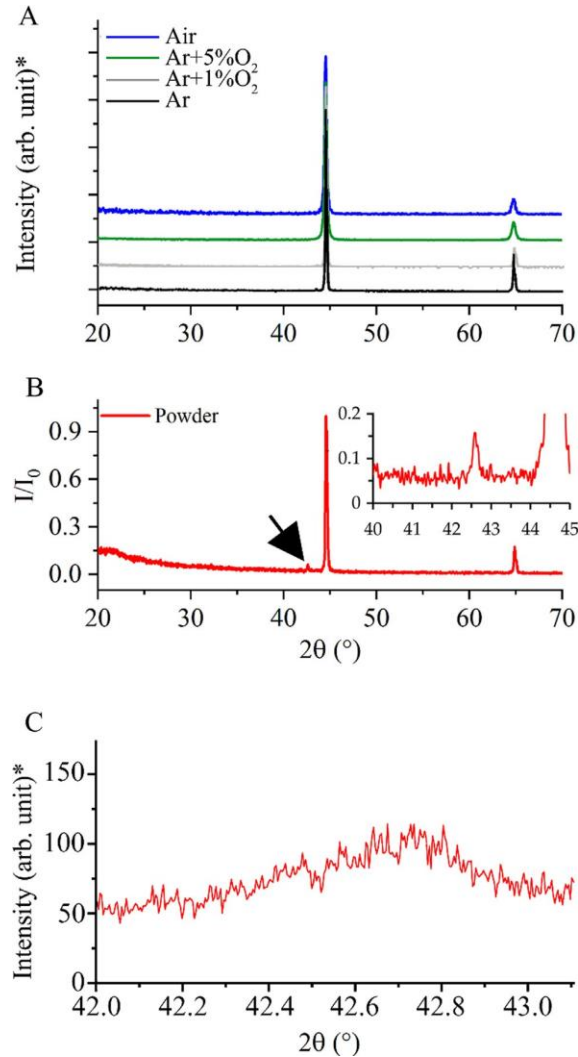


Figure 3.10: XRD results of powder (bottom) and fabricated solids with each respective chamber atmosphere: argon – red, 5 wt% oxygen – green, air – blue (top) [99].

When the powder is melted, the XRD (Figure 3.10) shows that the small intermetallic peak disappears, however, no prominent peaks were observed other than those for BCC Fe. Rieken reported that  $\text{Ti}_2\text{Y}_2\text{O}_7$  was observed to form using HIP and  $1200^\circ\text{C}$  heat treatment [9]; however,

trace amount of the oxides phases in our study were difficult to resolve using XRD due most likely to the micro-alloyed trace amount of Y and Ti.

SEM and TEM were used to observe the microstructure of fabricated solids with the chamber atmospheres ranging from argon to air, where multi-scale particles of varying compositions were observed. The SEM image and EDS maps in Figures 3.11 are typical of microstructures illustrating porosity due to un-optimized parameters where two types of oxide particle morphologies were commonly observed; spherical and prismatic (lens or triangular), 1-10 micron in size, which appeared randomly or without obvious microstructural preference. The solids fabricated in lower oxygen environments typically showed particles rich mainly in Y-Ti-O, while the sample fabricated in the air contained additional oxides rich in Cr-Y-Ti-O as shown in Figure 3.10. Here, the EDS maps illustrate both Cr-rich and Cr-free oxides where the larger Cr-Y-Ti-O particles are most likely due to the abundance of oxygen present in the atmosphere to react with the 15wt% chromium in the melt pool as well as yttrium and titanium either by direct oxidation or by reduction of the Cr-rich oxides.

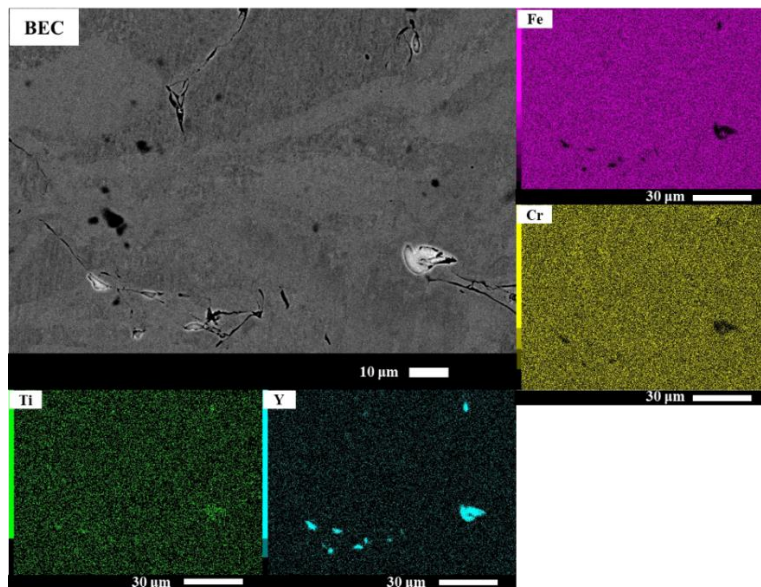


Figure 3.11: SEM images of fabricated solids produced in argon atmosphere showing EDS maps of Fe-Cr-Ti-Y rich areas.

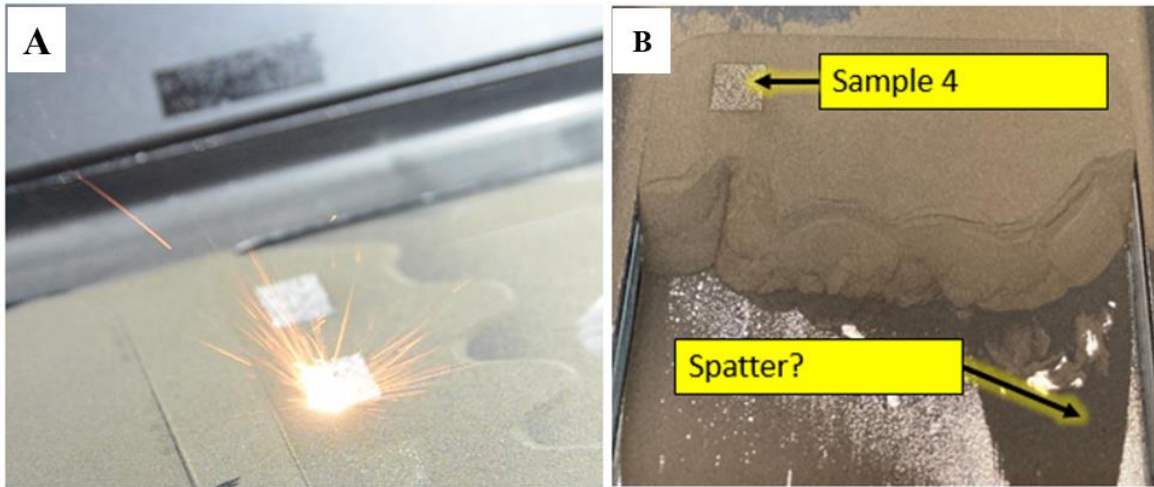


Figure 3.12: Photograph showing spatter generation at 1% oxygen atmosphere (A) and the accumulation of spatter particles at the completion of the test run (B).

There is likely a second contributor to the larger scale oxide particles observed in the solid microstructures. As illustrated in Figure 3.12 A & B, a significant amount of spatter was generated by the process in the form of both entrained particles and atmosphere-affected melt pool ejected droplets. In previous work by our group on 316L, it was shown that ejected spatter in LPBF was often larger than the starting feedstock size distribution.

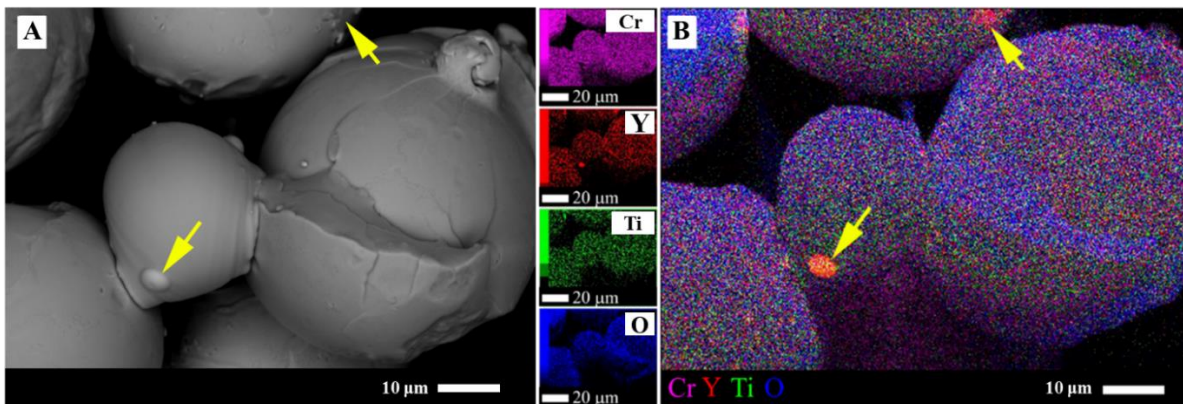


Figure 3.13: Backscattered SEM image of the spatter particle (A), EDS map color image (pink-Cr, red-Y, green-Ti, blue-O) showing typical micron scale Y-Ti-O oxides overserved prevalently on the surface of ejected spatter particles (B). Arrows indicate yttrium-containing areas of interest.

In this study, after fabrication, we screened the powders from the build area from the 90th percentile of the original size distribution thus retaining these larger ejected particles. Figure 3.13 shows an example of +325 mesh spatter screened from the powder bed after LPBF processing, where three particles are agglomerated together. This figure shows SEM EDS maps for Cr-Y-Ti-O to illustrate the location of surface oxides, featuring the prominent lens-shaped Y-rich oxide in the center of the image. This lens-shaped 4-5 micron oxide is observed on the surface of a solidified liquid ligament ejected from the melt pool, which connected the left and right particles together. The size and shape is consistent with the micron size particles in the solidified particles. It is unclear if these prominent oxides formed in the melt pool or existed from the previous melt layers and were ejected out with the liquid ligament, or if the oxide formed from the as the liquid ligament was traveling through the chamber atmosphere. It is clear, however, that oxides of this morphology and size are prevalent in solid samples with similar elemental makeup and would be incorporated into the solid if melted into subsequent layers. The oxide particle size observed here is consistent with spatter reported in other alloy systems where the oxides range from a few hundred nanometers to microns in size and consisted of elements typical of reduction such as Si, Ti, Mn, and Al, depending on the alloy system [139,140]. Also, recent reports in 316L have identified a number of silicates present in solid articles ranging in size from 50 nm to nearly 2 microns, similar in size and composition to oxides reported in spatter for that steel system. In the present system, yttrium and titanium exhibit the favorable free energies for oxide formation, oxides of this size and morphology were observed prevalently on the surface of liquid generated spatter but were only rarely observed in the original starting feedstock. From these observations, it is plausible that at least a portion of the large-scale oxides, can be attributed to ejected spatter that is reincorporated into solid material during LPBF processing.

Figure 3.14 shows representative TEM images from the argon, 1% O<sub>2</sub>, 5% O<sub>2</sub> and air fabricated samples. Here the high angle annular dark-field (HAADF) images reveal oxides with their associated Y-Ti-O composite EDS map. The yttrium and titanium-rich oxides were measured consistently less than 50 nm and were ubiquitous, especially apparent as small, spherical oxides. The micron-sized chromium-rich oxides commonly found in SEM for the air fabricated solid was not frequently observed at the nanometer scale, indicating that the mass-limited reaction for yttrium and titanium oxidation is more favorable for forming nano oxides; although it is presently unclear the relationship between composition, processing space and oxide size in these micro-alloyed GARS systems. Figures 3.15 - 3.17 shows TEM images for the samples fabricate in Ar, 1% O<sub>2</sub> and Air. Spherical oxides as represented in Figure 3.14 D & E at 180 kx magnification and identified by very small XRD peaks as Ti<sub>2</sub>Y<sub>2</sub>O<sub>7</sub>.

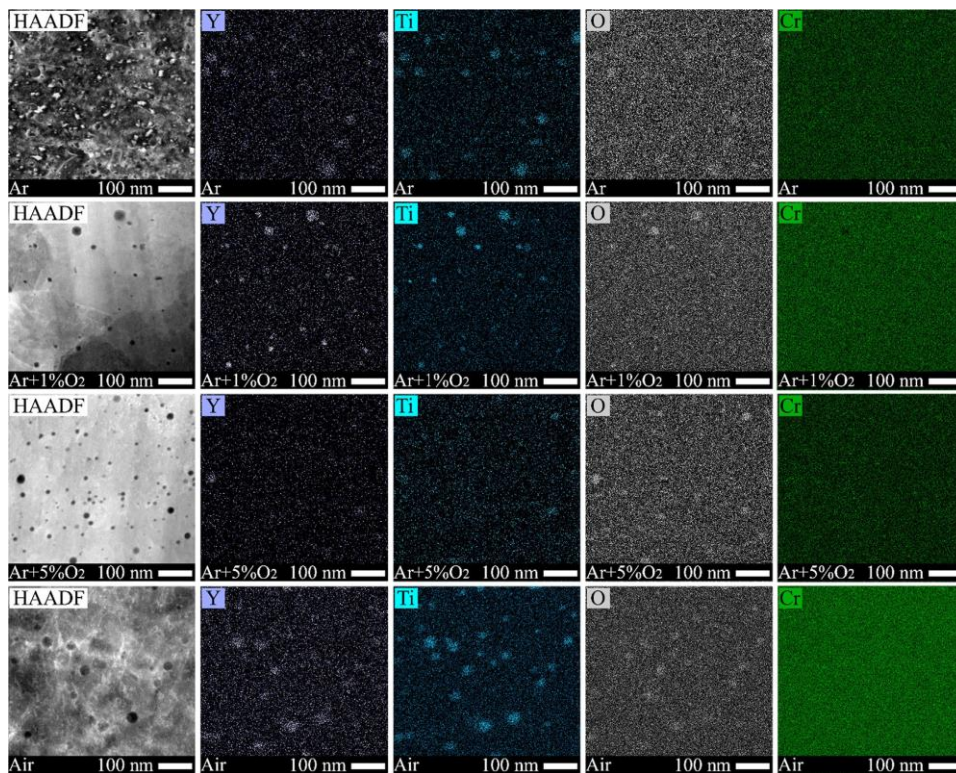


Figure 3.14: HAADF TEM images for the samples produced with LPBF in Argon, 1% oxygen, 5% oxygen and Air with respective Ti-Y-O EDS maps [99].

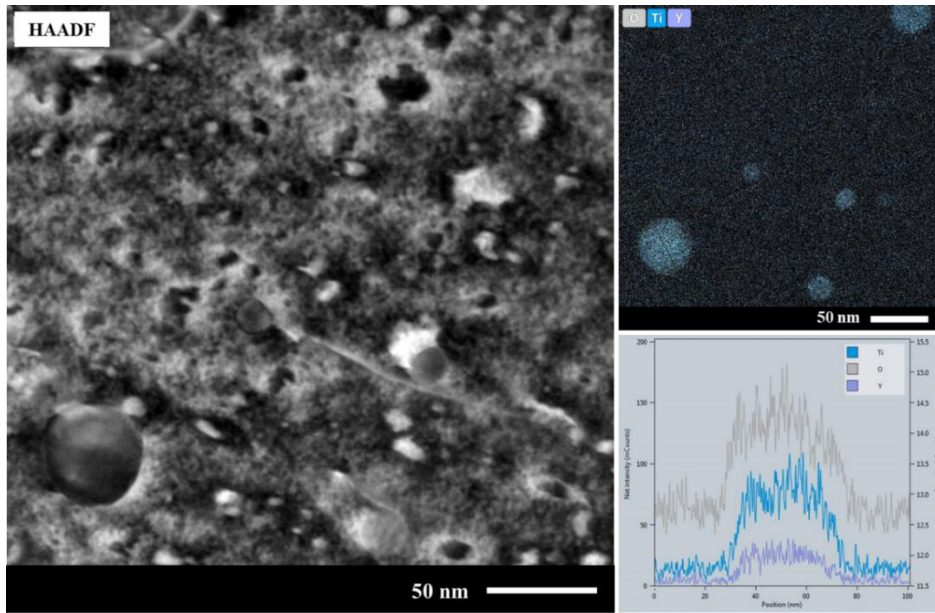


Figure 3.15: TEM For the samples produced with LPBF in Argon with Ti-Y-O EDS map and selected particle EDS line scans

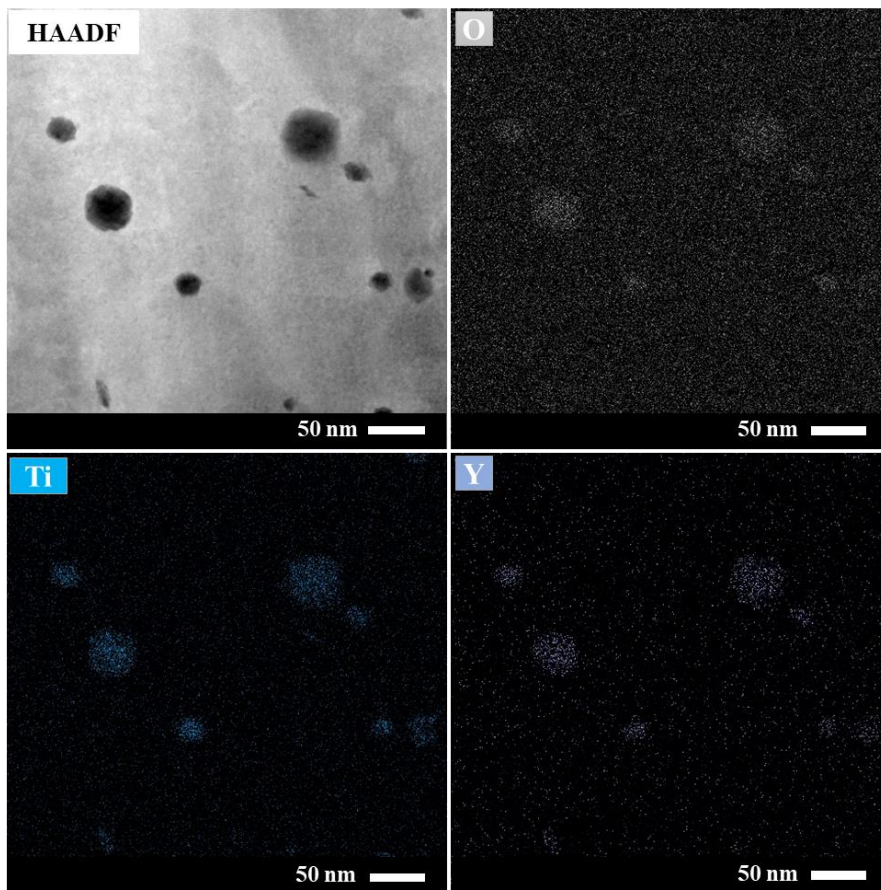


Figure 3.16: TEM For the samples produced with LPBF in 1% O<sub>2</sub> with Ti-Y-O EDS map

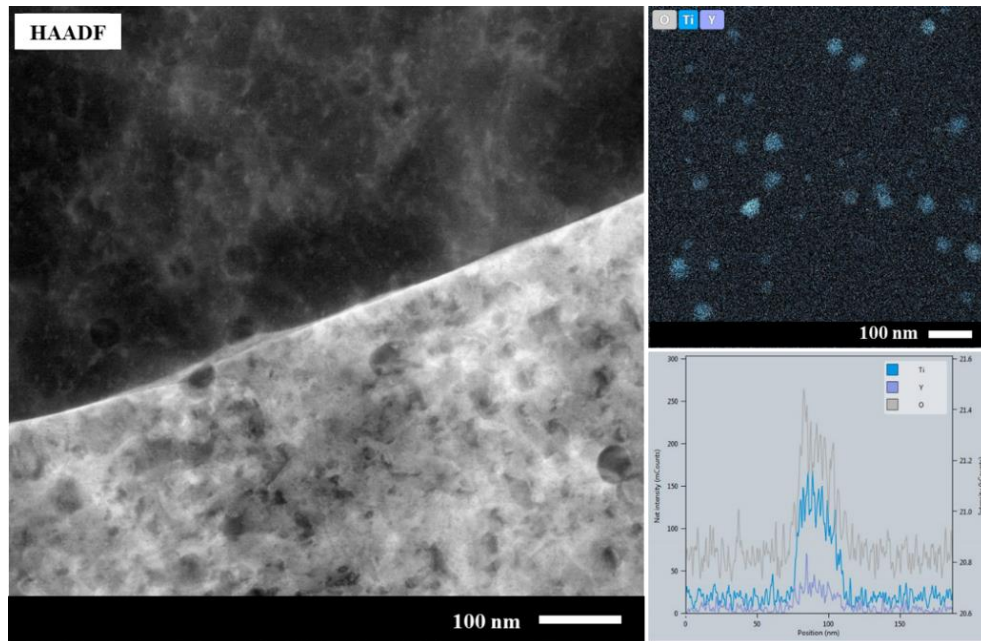


Figure 3.17. TEM For the samples produced with LPBF in Air with respective Ti-Y-O EDS map and selected particle EDS line scans.

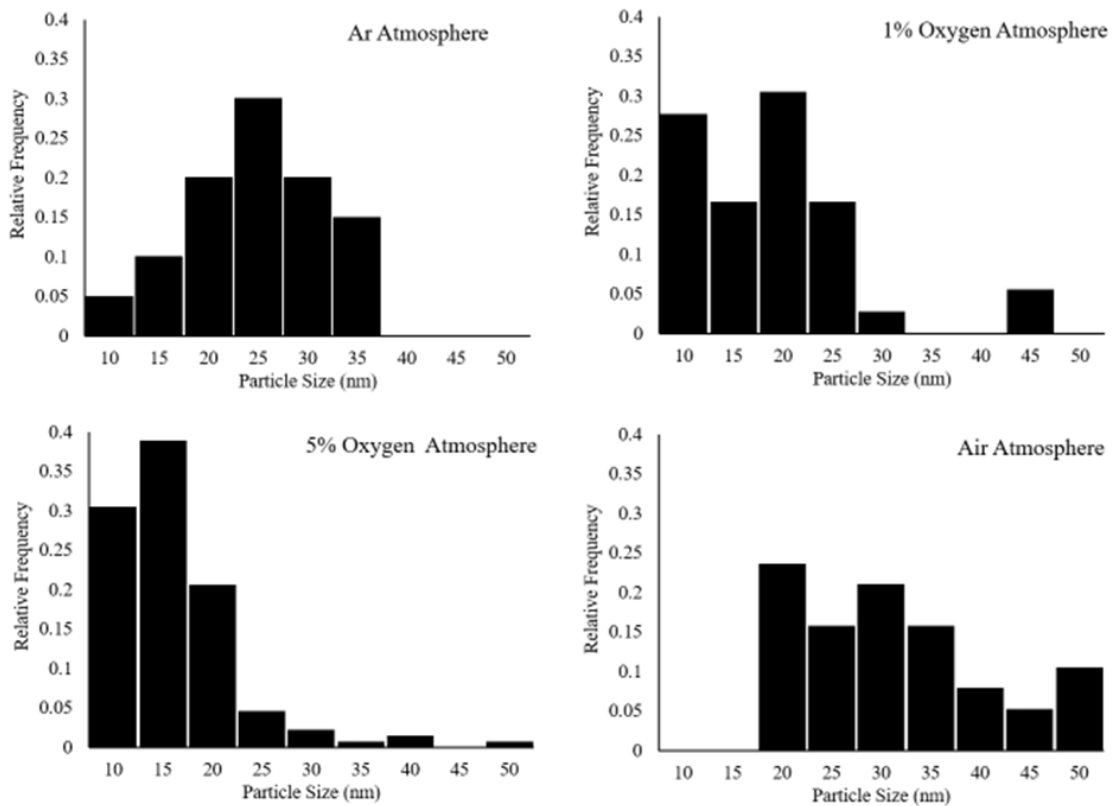


Figure 3.18: Nano oxide size distributions from TEM images for samples fabricated in Argon, 1% oxygen, 5% oxygen and air [99].

Figure 3.18 shows the histograms of the dispersoid sizes measured from TEM for solids produced in the argon, 1% oxygen, 5% oxygen, and air atmosphere conditions. From the histograms, the nano-oxide sizes were found to be significantly larger in the air region (average size: 29 nm) as observed by the shift in sizes mainly from 20 – 50 nm, as compared to the Ar (average size: 22 nm) with oxides measured consistently less than 35 nanometers.

As seen in Figure 3.19 the nano-oxide size decreases from the Ar condition to the 5% condition. The minimum median oxide size occurs at an atmosphere of 5% oxygen at 12.2nm. The error bars in Figure 3.19 A represent the 10<sup>th</sup> and 90<sup>th</sup> percentiles of the oxide size distribution. Figure 3.19 B shows an inverse relationship between the median oxide size and the calculated density of nano-scale oxides. The highest density of oxides was observed in the sample produced with 5% oxygen at  $3.4 \times 10^{21}$  oxides/m<sup>3</sup>. The range of nano-dispersoid sizes for the 5% oxygen sample are smaller than those reported previously for LPBF, as shown in the cumulative distributions from this study and the AM studies from the literature where the size values for oxide dispersions range from 18.05 to <100 nm for MA powders and 100 nm for blended powders, with one outlier at nearly 1 micron. This indicates that microalloying powders with oxide-forming elements and exposing them varying levels of oxygen during LPBF has the capability of producing nanoscale oxides comparable to traditional ODS processes such as MA but without the processing issues related to oxide agglomeration or brittle structures.

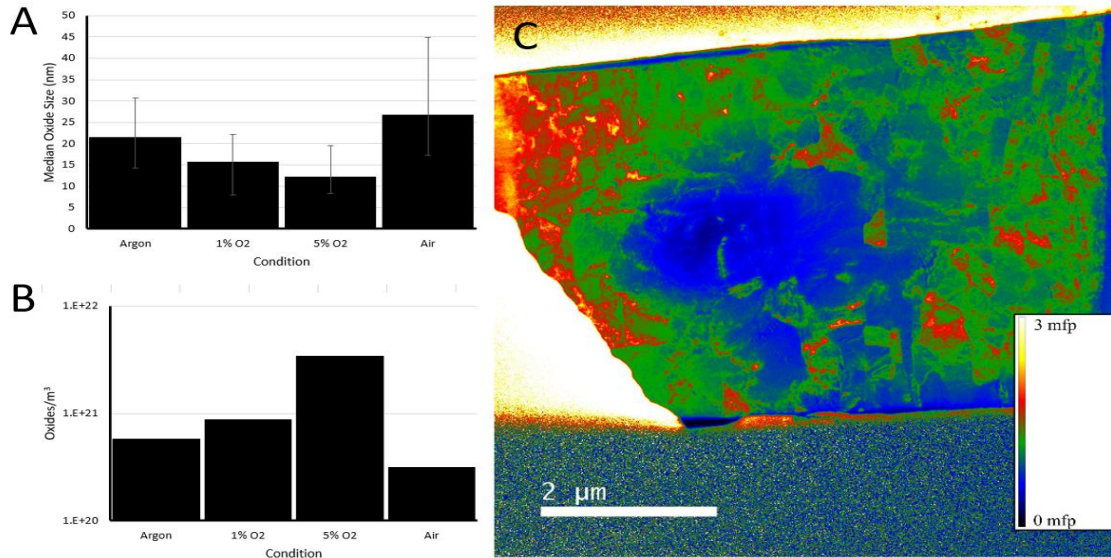


Figure 3.19: Plot showing the median oxide size measured from TEM, error bars indicate the 10th and 90th percentiles of the oxide size distribution (A). Plot showing the measured density of oxides per m<sup>3</sup>(B). Thickness maps from EELS analysis were used to calculate volumetric oxide densities (C) [99].

It should be noted that, unlike many studies in the literature which simply assumed TEM foil thickness in the calculation of the volumetric density of oxides, the thickness measurements and maps of the TEM lift-outs used in our study were obtained using Electron Energy Loss Spectroscopy (EELS) zero loss method using the Digital Micrograph script developed by Malis et al. [159] (Figure 3.19 C). The electron Mean Free Path (MFP) in obtained for the regions of interest and converted into a thickness using the method which relies on the mean atomic number based on the composition. The thickness area of the regions of interest were used to calculate particle densities. The error in thickness measurement is estimated to be ~10%.

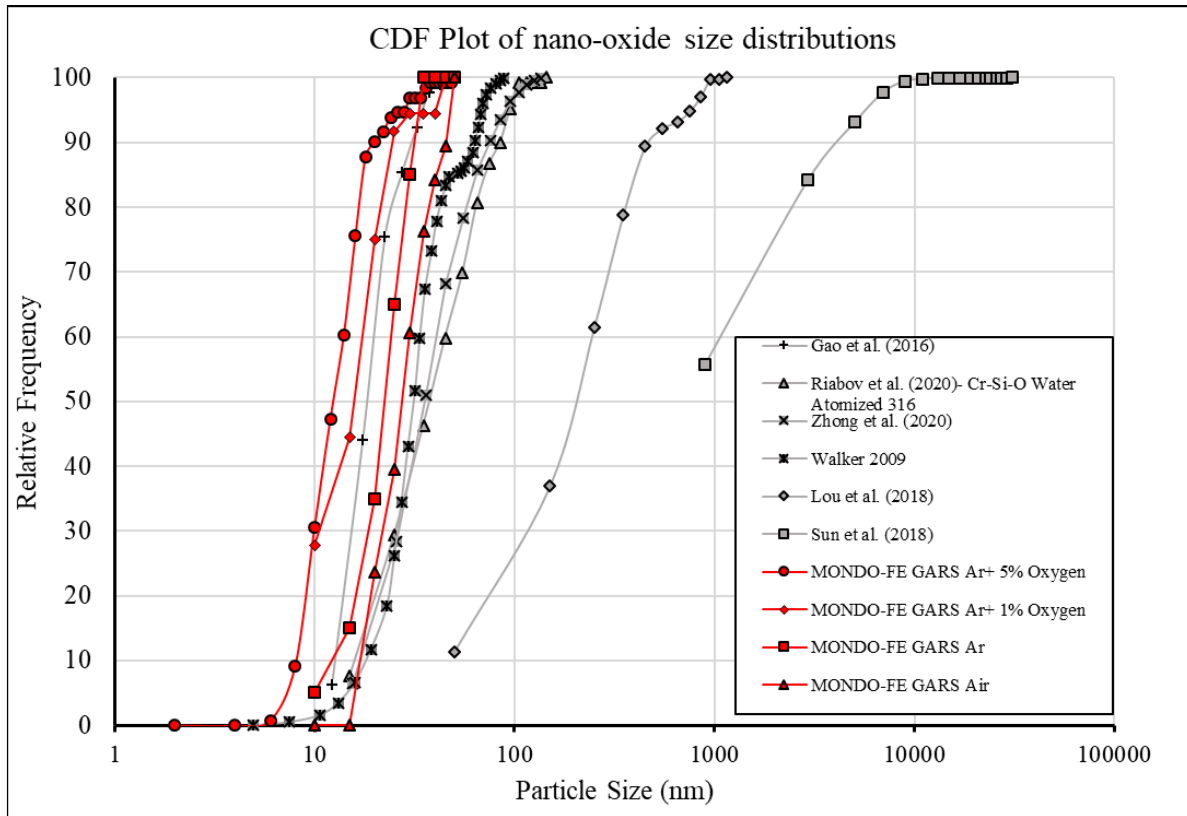


Figure 3.20: Cumulative distribution of nano-oxides reported in this study as compared to the current literature [99].

Figure 3.21 shows a contour map of the Vickers hardness measured over a 5mm x 8mm region that encompassed material processed in all four chamber atmosphere conditions. These data show a general increase in the Vickers hardness associated with increasing oxygen content in the atmosphere during processing. The average of the measurements was  $147.0\text{HV} \pm 27.2$  from the argon region,  $148.3\text{HV} \pm 25.4$  for the region produced in 1% O<sub>2</sub>,  $160.8\text{HV} \pm 17.8$  for the region produced in 5% O<sub>2</sub>, and  $170\text{HV} \pm 10.7$  for the region produced in air. These values are consistent with and fall in the range of LPBF of ODS steels with similar compositions in this study; again demonstrating that ODS steels can be produced by in situ formation of nano-oxides during LPBF processing of micro alloyed powders without the need of MA or blending. The previously noted porosity in the samples contributed to the variability in the hardness map, nevertheless, the

general trend in the hardness values is in agreement with the measured oxide size and density distributions.

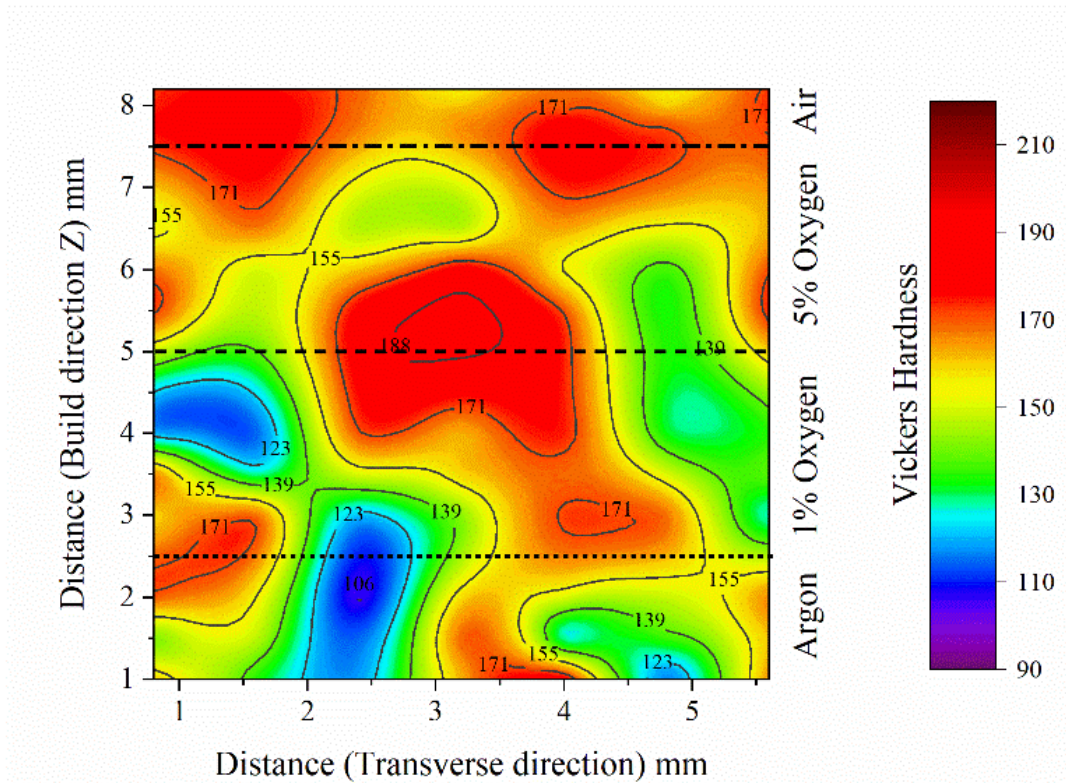


Figure 3.21: Contour map showing the Vickers hardness, measured over a 5mm x 8mm region of the LPBF consolidated GARS sample encompassing regions processed in argon, 1%O<sub>2</sub>, 5%O<sub>2</sub> and in air atmospheres [99].

### 3.4 Conclusions Drawn from Preliminary Cuboid Designs

The micro-alloyed GARS feedstock consisted of a Cr-oxide rich shell and mostly free of Y oxides or Ti oxides. Yttrium was instead found inside the powder as a stable intermetallic, Y<sub>2</sub>Fe<sub>17</sub>; The powder was found to have only trace amounts of second phase as confirmed by EPMA and XRD. The powder did show a very thin surface oxide which was not readily detectable in the powder XRD but was sufficient to fuel Y-Ti-oxide formation in low oxygen PBF environments.

- Solids samples were fabricated using melt parameters commercially available for 316L stainless steel.

- The use of powder bed fusion techniques is preferred for this system as the rapid solidification was shown to produce a fine distribution of spherical oxide particles in the steel with no obvious agglomeration or significant coarsening during processing.
- TEM was used to measure the nanoscale oxides, which ranged in size from a minimum median value of 12.2nm at atmospheric oxygen content of 5% to a maximum median value of 26.7nm for the sample fabricated in Air .
- Sample parameters must be further optimized to improve density without sacrificing oxide size or nano-oxide density distribution.
- Solids fabricated in low oxygen environments produced micron-scale Y-Ti-O rich oxides where the samples produced in air contained a mix of micron-sized Cr-Ti-Y rich and Y-Ti rich oxides, which agreed reasonably well with thermodynamic calculations. The nanometer oxides did not show a significant amount of chromium, regardless of the fabrication environment.
- This study demonstrated the formation of a high density of nanoscale oxides in the solids produced by reaction synthesis in the melt pool during LPBF; The maximum number of oxides,  $3.4 \times 10^{21}$  oxides/m<sup>3</sup>, was observed for the samples produced with an atmospheric oxygen content of 5%. The minimum,  $3.12 \times 10^{20}$  oxides/m<sup>3</sup>, occurred in regions produced in air.
- However, a bimodal size distribution was observed where oxides on the order of 1-10 microns were also observed along with the nanoscale oxides where micron size oxides were found to have lens shaped and prismatic morphologies. The larger-scale oxides, at least in part, were found to originate on the surface of spatter ejected

from the melt pool, which is subsequently remelted by the LPBF process. These large oxides effectively sequester Y and Ti that would otherwise be available to form nanoscale oxides, suggesting that the management of melt pool spatter may play an important role in maintaining a high density of nanoscale oxides during LPBF.

- The observation of micron-scale Y-Ti-Cr oxides on the surfaces of spatter ejected from the melt pool also has implications related to the recyclability of ODS powders for AM, which requires further study.

## CHAPTER 4

### 4.1 Background Information

The preliminary results from chapter 3 demonstrated that the liquid phase consolidation of GARS precursor powders by LPBF resulted in a high density of nano-scale dispersoids. This was accomplished using legacy GARS powders from a previous AMES lab HIP consolidation study. In this chapter, a new powder composition corresponding to ODS 14YWT, was produced by AMES lab. The objective of these experiments was to elucidate the feasible LPBF process parameter space to produce fully dense samples. From the densest samples, the oxide size and density were characterized, and finally, tensile samples were produced to evaluate the mechanical properties.

### 4.2 Hypothesis

The alloy in this study is termed 14YWT, where 14 indicates the Cr concentration (wt.%) and YWT represents the additions of  $Y_2O_3$ , W, and Ti. This composition was developed at Oak Ridge National Laboratory [12,13]. The composition of these alloys is a crucial to obtain the desired parameters like high strength and creep behavior. Cr improves the corrosion of the BCC ferritic iron [160]. It has been observed that at the addition of Ti promotes the decomposition of  $Y_2O_3$  to form smaller but highly densely packed Y-Ti-O oxide [9,30,161]. Yttrium maintains limited diffusivity in the ferritic matrix over temperature ranges of 700-1300°C, and therefore helps to stabilize Y-Ti-O nano oxide after formation [9,161].

The primary purpose of the study in this chapter is to map the process space of the 14YWT GARS powder from AMES lab (AMES batch ASC-1-81) by studying and characterizing the microstructure and performing preliminary mechanical testing of the as-produced samples. The influence of varying the oxygen content of the LPBF chamber atmosphere was also investigated.

The experiments were performed under various atmospheric conditions varying from Argon, Argon + 2%, 3%, 5%, 7% and 10% O<sub>2</sub> by wt. Unlike the previous Cr-166 study, each sample fabrication was performed under a single atmospheric condition at a time. For this study, the hatch spacing and laser beam speed were varied to create a process map which ensured that process conditions ranging from under melt conditions (less volumetric energy) to over melting (very high volumetric energy) conditions were simulated. Layer height (0.025mm) and laser power (95W) were kept constant. Based on the optical relative densities and Vickers hardness measurements, a process space was identified which was used to fabricate a large block to demonstrate scalability and repeatability and, a tensile sample to test for preliminary mechanical testing.

## **4.3 Methodology**

### **4.3.1 Powder Preparation and Characterization**

Table 4.1 shows the mass and nominal size distribution of the 14YWT powder received from AMES lab. The powder was screened by AMES lab into 3 distributions with a yield of 611g between 45 μm and 53 μm (-270/+325 Mesh), 2434g between 20μm and 45 μm (-325/+625 Mesh) and 1321g below 20μm (-625 mesh). Oxygen content was measured by inert gas fusion using a LECO OH 836 referencing E1019 – 18 standard iron base alloys. Table 4.1 depicts the recorded oxygen content of the powder. The bulk elemental composition of the as-atomized (-60Mesh) powder performed by AMES lab was determined by ICP-MS, shown in Table 4.1. ICP, developed in the early 1960s by Thomas Reed is based on measurement of excited atoms and ions at the characteristic wavelength for the measured elements [162]. ICP-MS developed in 1980s is used for elemental and isotope analysis and uses an inductively coupled plasma ICP (which serves as ion source) and ionized samples to measure an atom's mass by mass spectrometry (MS) [163]. In an ICP setup, the plasma is an atom source while in an ICP-MS the plasma is an ion source [164].

ICP is mainly used for samples with high total dissolved solids (TDS) or suspended solids while on the other hand, ICP-MS is a preferred choice for trace-element detection due to its ability to detect trace elements in parts per trillion (or even lower in cases of some elements) and, speed of analysis [164,165].

Table 4.1: Mass and nominal size distribution of the 14YWT powder received from AMES lab (Batch ID: ASC-1-81)

Mass (g)	Nominal Size Distribution ( $\mu\text{m}$ )	Screen Cut (Mesh)	Oxygen Content (ppm)
611	-53/ 45	-270/+325	928*
2434	-45/+20	-325/+270	1034*
1321	-20	-625	661*
*Based on steel standard-will calibrate based on new data for GARS			

Table 4.2: Powder composition of the 14YWT powder received from AMES lab (Batch ID: ASC-1-81)

Element	Wt.%	Method
Cr	14.03	ICP
Fe	82.1	Bal.
Ti	0.4	ICP
W	3.06	ICP
Y	0.35	ICP-MS
Zr	<0.001	ICP-MS

Particle size distribution (PSD) of the powder was analyzed using a Microtrac S3500 laser diffraction particle analyzer following a wet method protocol with ultrasonic agitation. The numeric distribution of the nominal 20 $\mu\text{m}$  to 45 $\mu\text{m}$  cut reveals a bimodal distribution with a significant fraction of fine powder. Powder from 20  $\mu\text{m}$  - 45  $\mu\text{m}$  and 45  $\mu\text{m}$  - 53  $\mu\text{m}$  were blended

together. It can be hypothesized that retaining this bimodal distribution may result in improved process ability during LPBF. Figure 4.1 shows the volumetric and numeric powder size distributions for the 20 – 45  $\mu\text{m}$ , 45 - 53  $\mu\text{m}$  and the 20 - 53  $\mu\text{m}$  blended powder. A significant fraction of fines and a bimodal distribution is evident in the numeric distribution. These data are supported by the initial observations of the powder morphology, which was imaged using a JEOL 6010LA scanning electron microscope (SEM) samples (Figure 4.2).

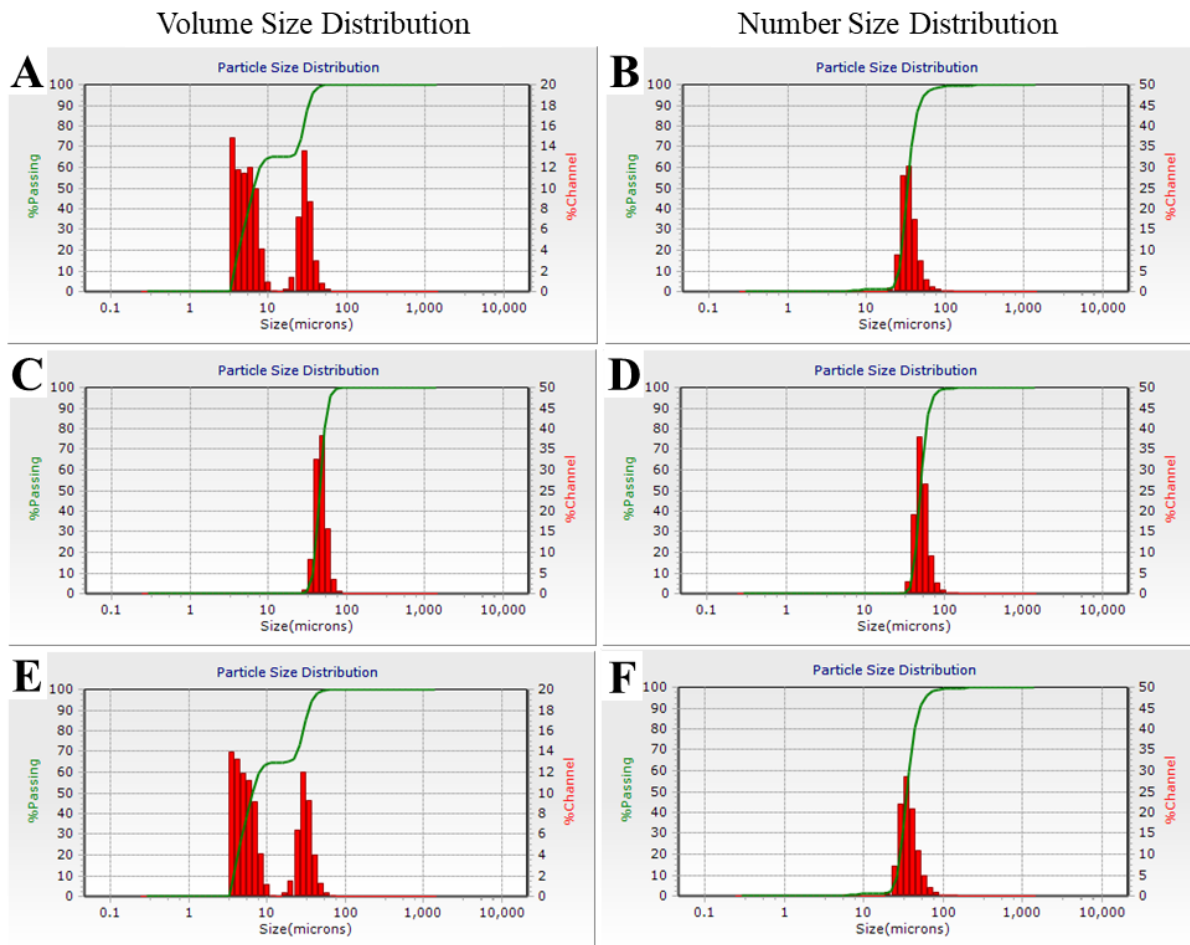


Figure 4.1: Histograms showing the Volume and Number Particle Size distribution of 20 $\mu\text{m}$ -45 $\mu\text{m}$  (A & B), 45 $\mu\text{m}$ -53 $\mu\text{m}$  (C & D) and a 20 $\mu\text{m}$ -53 $\mu\text{m}$  after blending in an argon glovebox.

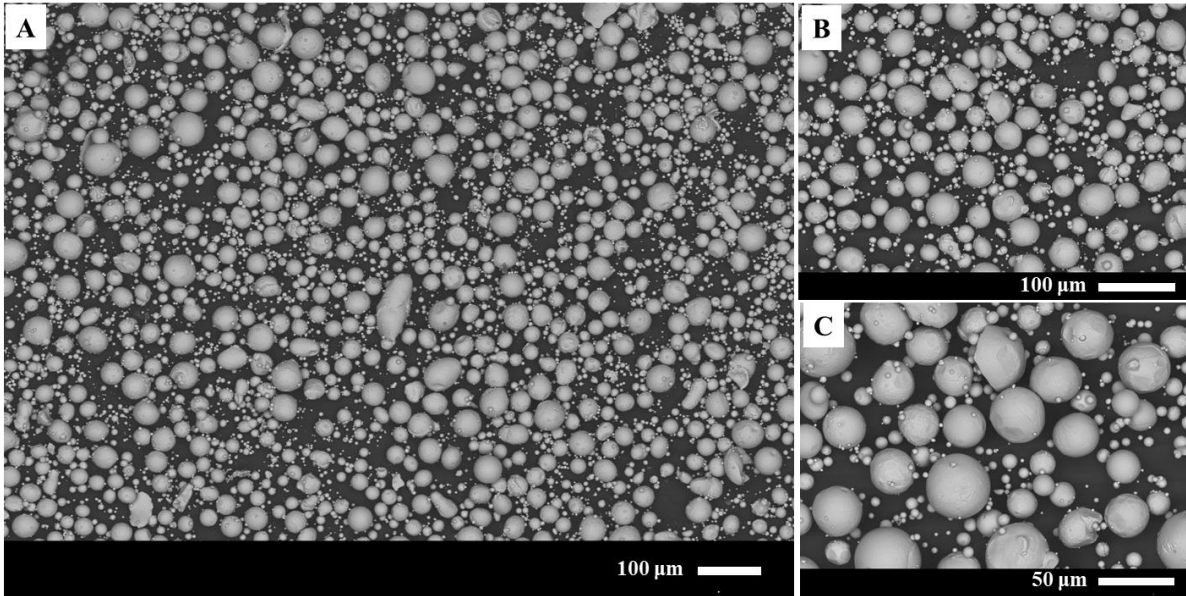


Figure 4.2: Secondary scanning electron microscope images (100X, 250X and 500X) showing a bimodal powder size distribution and generally spherical morphology.

#### 4.3.2 Laser Powder Bed Fusion Experimental Setup

LPBF fabrication of all test specimens was carried out using a modified concept laser M100R with a 100W Nd:YAG fiber laser at  $\sim 1060$  nm wavelength and  $50 \mu\text{m}$  spot size. Figure 4.3 shows a photograph of the modified machine. Since previous trials, few modifications had been added to the concept laser to effectively analyze oxygen content in the system. A Thor labs CCS200 optical emission spectrometer (OES) was aimed at each sample during LPBF under each atmospheric condition. OES is a method for determining the elemental composition of variety of metals and or alloys by digitally analyzing the visible and ultraviolet elemental wavelength of the plasma plumes generated when an element reaches it's excited stage by losing electron [166]. Emission wavelength is determined by the atomic transitions and emission intensity depends on atomic concentration. Research by Lough et al., Everton et al., Lednev et al., have shown OES is an ideal choice for applications where an exact breakdown of elemental composition is desired to analyze in-process failure detection by detecting and analyzing the spectral content of vapor plume

and relative emission intensity [167–169]. A Stanford Research Systems SRS 200AMU Residual Gas Analyzer (RGA) was installed to sample the partial pressures of the chamber gases. An RGA is essentially a mass spectrometer which is designed for environmental analysis and process control for vacuum systems. RGA can monitor chemical composition of the gas within a vacuum chamber by ionizing the gases and then filtering them according to their mass to charge ratio, which then creates a current and the intensity is recorded as the output signal [170,171]. Research by Nyman et al, Terrazas et al., Ledford et al., Frigola et al., highlights the feasibility and importance of using an RGA to analyze and monitor the chamber for concentration of outgassing including contamination for process monitor [172–175]. As the powder sinters, residual surface gases including oxygen escapes the system and can then be analyzed by the RGA. In order to sample at high (atmospheric pressures) the RGA was connected to a Pfeifer High-Cube turbo cart. As the concept laser operates under gaseous conditions at atmospheric pressure, in order to effectively measure residual gases, a chamber interface in the form of a 4 µm copper conflat connector disc that has been precision laser-drilled with a 4µm through hole. This essentially created a controlled leak, allowing the RGA to operate under  $5e^{-4}$  mBar condition. Powder storage, sampling, and blending all took place in a flowthrough argon glovebox (right side of Figure 4.3). Data from RGA could not be effectively analyzed due to lots of noise in the data. Figure 4.4 below is a plot showing the output of the optical emission spectrum for 3 samples with the same LPBF parameters, but different gas mixtures (Ar, Ar+5%O and Ar+10%O). This work is ongoing and interpretation is contingent upon additional data being compiled from the other samples, nevertheless, the OES sensor is able to differentiate melt pools from the various test conditions (Figure 4.4). These data are, of course considered with a margin of error regarding probe placement and instance of data collection.



Figure 4.3: Photograph of the LPBF/GARS experimental setup and workflow.

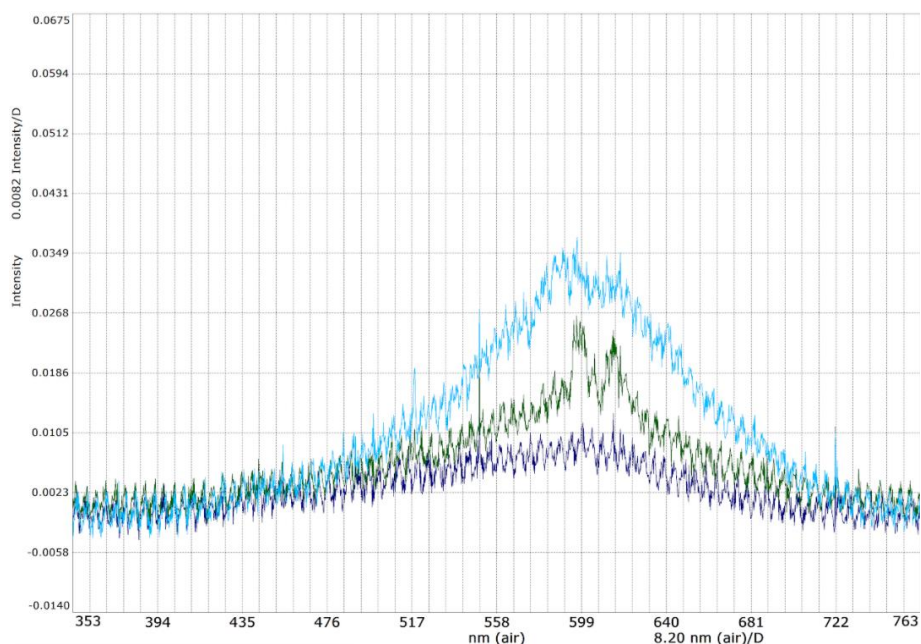


Figure 4.4: Spectrum of optical emissions (OES) recorded for three samples during LPBF. Argon (Dark blue), Argon +5% oxygen (green), and Argon +10% (light blue)

During each experimental run, the process was continuously recorded by an optical camera mounted on the outside of the IR filter viewport. This was used to qualitatively assess the surface condition of the powder bed and the fabricated samples. Along with the RGA and OES, Oxygen content was also monitored with a low external resolution ( $\pm 0.1\%$ ) RKI OX-600 oxygen monitor which was installed in the system chamber and monitored throughout the process.

The experimental design was organized such that a standard 1000 series steel LPBF build substrate (from GE/Concept laser) measuring 90mm x 90mm x 10 mm was CNC machined with three slots 6.35 mm deep and 20.32 mm wide across the plate. Low-Carbon steel plate stock, precision ground on both faces was water-jet cut into inserts that matched the slots in the plate. These inserts became the substrate upon which the GARS samples were produced, eliminating the time-consuming step of using wire EDM to separate the samples from the plate for analysis. A 2D schematic diagram (A), 3D CAD file (B), and as fabricated plate (C) for this design are shown in Figure 4.5 along with the seven 15mm x 7.5mm x 3.5mm samples that were fabricated on the first insert for each trial. To preserve powder to print multiple samples, powder was only spread onto the first insert in this portion of the study. The as printed samples were etched ‘S#’ on the top surface where ‘#’ represented the sample number. Each sample had a unique identifier which was used to distinguish each sample. Figure 4.7 describes the powder loading methodology. As with previous Cr-166 trial, 150g of powder was loaded on the right side of the feeder such that only the first insert got powder during re-coating phase. This ensured that sufficient fresh powder was available to print 3 prismatic and 2 tensile samples without powder re-use as much as possible.

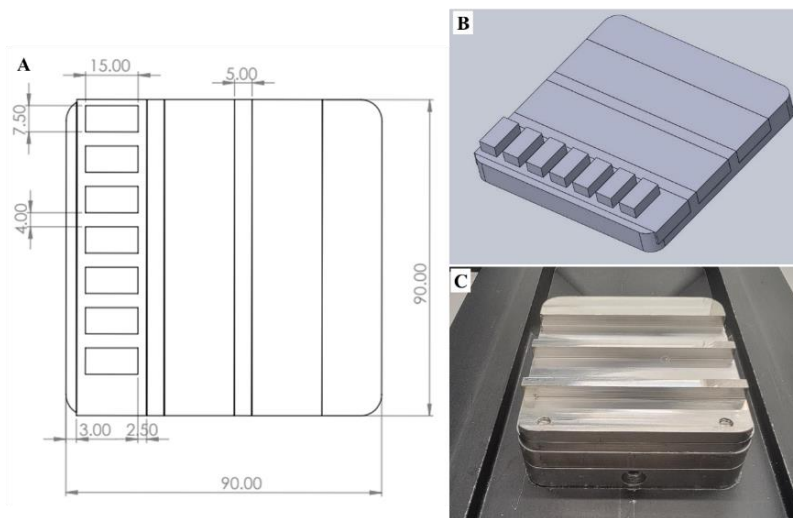


Figure 4.5: Schematic of the build substrate and steel inserts upon which the LPBF samples were fabricated (A) and ISO-view CAD model of the same (B), final machined plate with slots (C)

For each gas mixture, ~21 samples were fabricated with laser powder bed fusion in accordance with the LPBF process parameters shown in Table 4.3 and Appendix A. Within each grouping of 21 samples the melt parameters and sample placement were assigned using the random number generator in Microsoft excel. Note that to reduce the fresh powder consumption, for the 3% and 7% oxygen conditions, the only parameters that were used were those identified as being within the “dense” process window from the other experiments. During experimentation, it was determined that the gas recirculating fan was malfunctioning during the 5% and 10% trials. Seven selected cases of each experiments were identified as promising and were replicated.

The layer thickness was fixed at 0.025mm, and the laser powder was fixed at 95W (the maximum for this system is 100W). The hatch spacing was varied in discrete steps of 0.03 mm, 0.05 mm, and 0.08 mm. The beam velocity was varied to target a spread of volumetric energy densities trials that heat input models indicated would range from the very porous (due to lack of fusion), very dense (>95% relative density) and over melted (exhibiting swelling, instability and/or keyhole porosity). The scan line length is an important parameter that contributes to the local heat inputs. Based on the initial trials with Cr-166 powder, a scan line length of 10mm was chosen for this experiment. This breaks the melting of each layer into multiple 10mm x 10mm patches or islands, the location of these patches is shifted from layer to layer by a set amount. Table 4.3 details the parameters associated with the scan line length and islanding procedure.

Table 4.3: Typical LPBF processing parameters utilized for each gas mixture (Ar, Ar+3%O2, Ar+5% O2, Ar+7%O2 and Ar+10%O2).

Hatch Spacing (mm)	Layer Thickness (mm)	Beam Power (J/s)	Beam Velocity (mm/s)	Volumetric Energy Density (J/mm <sup>3</sup> )
.03	.025	95	1,050.00	75.00
.03	.025	95	1,700.00	225.00
.03	.025	95	380.00	200.00
.03	.025	95	434.29	175.00
.03	.025	95	506.67	150.00
.03	.025	95	608.00	125.00
.03	.025	95	760.00	100.00
.05	.025	95	1,050.00	250.00
.05	.025	95	337.78	225.00
.05	.025	95	380.00	200.00
.05	.025	95	434.29	175.00
.05	.025	95	506.67	150.00
.05	.025	95	608.00	125.00
.05	.025	95	760.00	100.00
.08	.025	95	304.00	250.00
.08	.025	95	337.78	225.00
.08	.025	95	380.00	200.00
.08	.025	95	434.29	175.00
.08	.025	95	506.67	150.00
.08	.025	95	608.00	125.00
.08	.025	95	760.00	100.00

Table 4.4: Scan line length and islanding parameters used in this study, the X and Y size determine the scan line length. The X and Y step determine how much this pattern shifts from one layer to the next and the angle of rotation is the angle of the island about the z axis relative to the sample X and Y axes.

Parameter	Dimension
X Size	10 mm
X step	2.5mm
Y size	10 mm
Y step	2.5mm
Angle of Rotation	45 deg

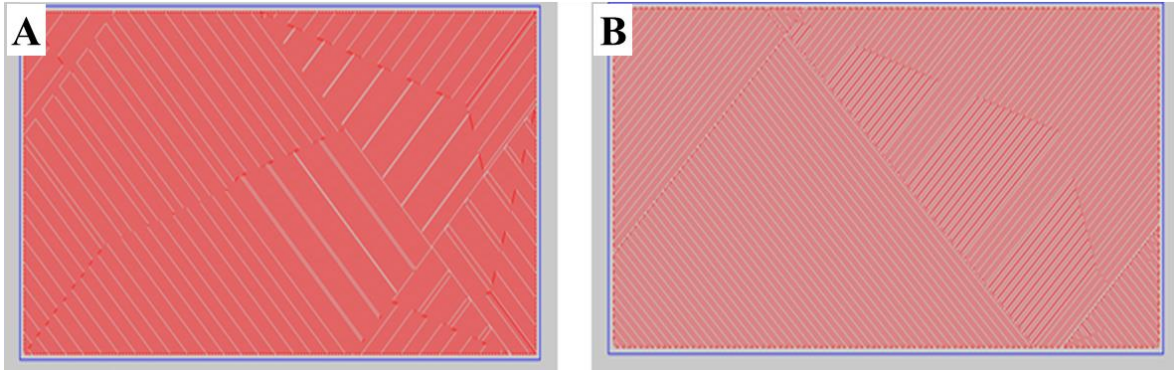


Figure 4.6: Example of the toolpath output showing the 10mmx 10mm islands on a single layer of a 7.5 x 15mm sample. Left sample has a 30µm hatch spacing (A) and right sample has 80 µm hatch spacing (B).

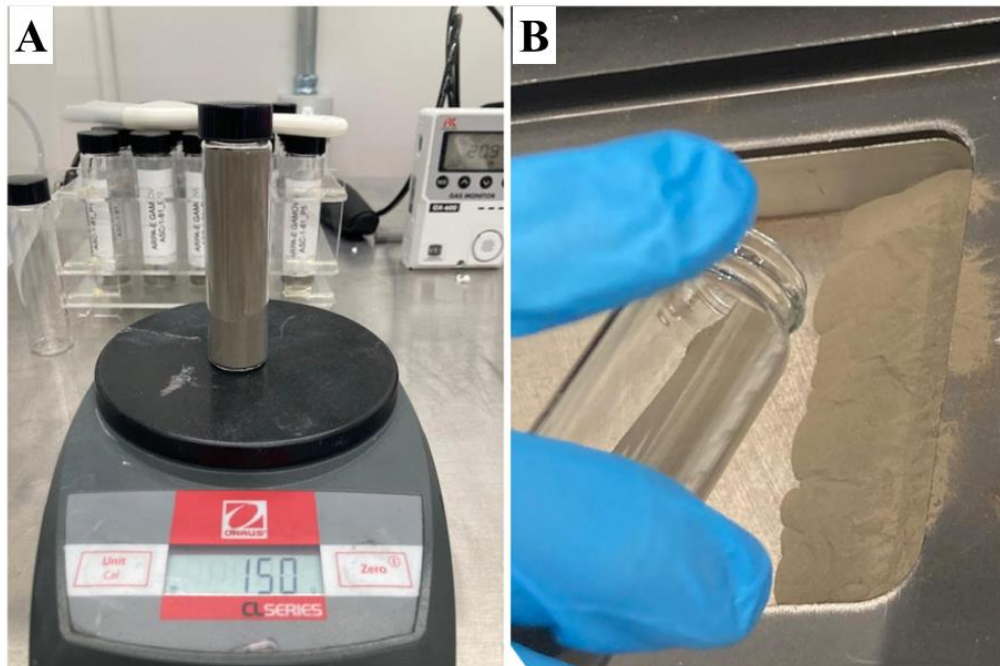


Figure 4.7: Photograph of the 150g vial of ASC-1-81 powder used for each experiment (A) and photograph showing how the powder was loaded into the LPBF powder deposition chamber (B).

The chamber gas flow, at the surface of the powder-bed moves from left to right as evidenced by the direction of the weld spatter in Figure 4.8A. Figure 4.8 B shows one of the sample inserts after removal from the powder bed with seven samples.

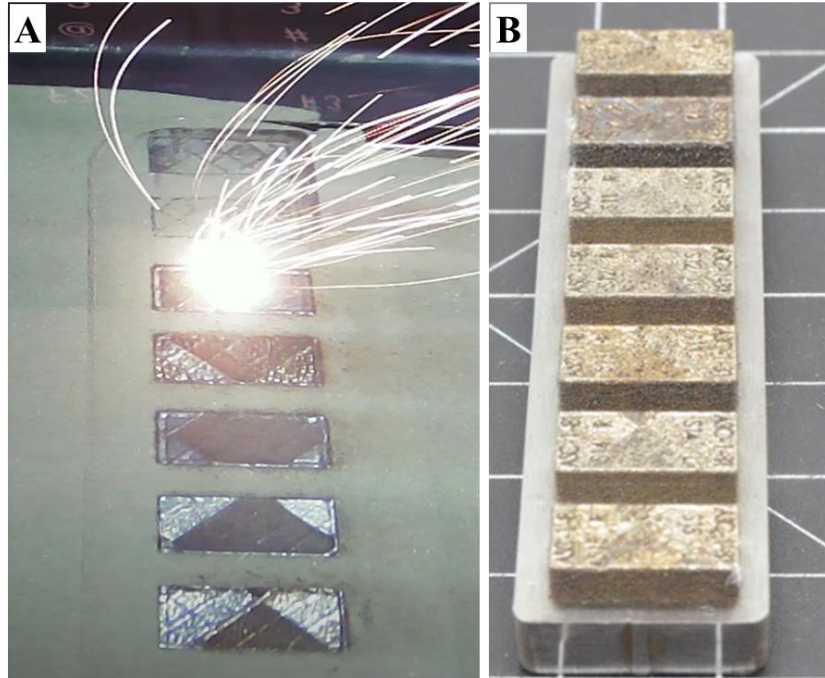


Figure 4.8: Photographs showing an example of the samples being processed during LPBF (A), and after removal of the sample insert (B).

## 4.4 Discussion

### 4.4.1 Powder Characterization

The internal structure of the powder particles was examined by TEM to determine the distribution of elements and to confirm the absence of Y-Ti dispersoids in the precursor powder. Figure 4.10 A shows a TEM image of a liftout from a typical median-sized particle. The arrows point to regions along grain boundaries where continuous pockets rich in Y were observed. These were often associated with discontinuous regions rich in Y with spherical and elongated morphologies. Previous studies using Cr-166 compositions identified yttrium as elemental yttrium at the grain boundaries, in solution in the matrix, or as a stable intermetallic compound  $Y_2Fe_{17}$  [9–11]. The labeled boxes in Figure 4.9A refer to regions inspected with high-angle annular dark-field (HAADF) imaging and EDS maps of Fe, Cr, Ti, Y, and O in Figures 4.9 B, C & D. Figure 4.10 shows a region through the surface of the powder particle. The oxide crust was observed to be

continuous and consisted of a top layer of Cr and O, followed by a thin subsurface layer of Ti, Y, and O, where both layers combined, were less than 50 nm as measured by an EDS line scan in Figure 4.10 E. During gas atomization, the interaction of the O<sub>2</sub> - rich gas stream with the liquid droplet resulted in the formation of a kinetically favored oxide shell/skin rich in Cr<sub>2</sub>O<sub>3</sub>. Since GARS powders are intentionally oxidized during atomization, the oxide crust is often slightly thicker than traditional steel powder. In Cr-166 compositions, the continuous surface layer of Cr-O was typically < 150 nm [9].

Figure 4.9 C shows an area near the surface and reveals the presence of Y near a grain boundary. From the EDS maps, it would appear that these same regions are lacking in Fe, Cr, and O. Figure 4.9D shows a region on the interior of the particle. The EDS maps show that the internal features, indicated by the red arrows, are depleted in Cr, Ti, and O, indicating mixed Y and Fe-Y rich phases regions. These regions were identified as Y<sub>2</sub>Fe<sub>17</sub>. The bulk of the reactive Y & Ti elements were observed to be available in submicron sizes individually or as intercellular Y containing intermetallic, which is critical to the process where they may be available for reaction with the Cr-oxide shell, which acts as a chemical reservoir during LPBF to form nano-scale oxides in the melt pool.

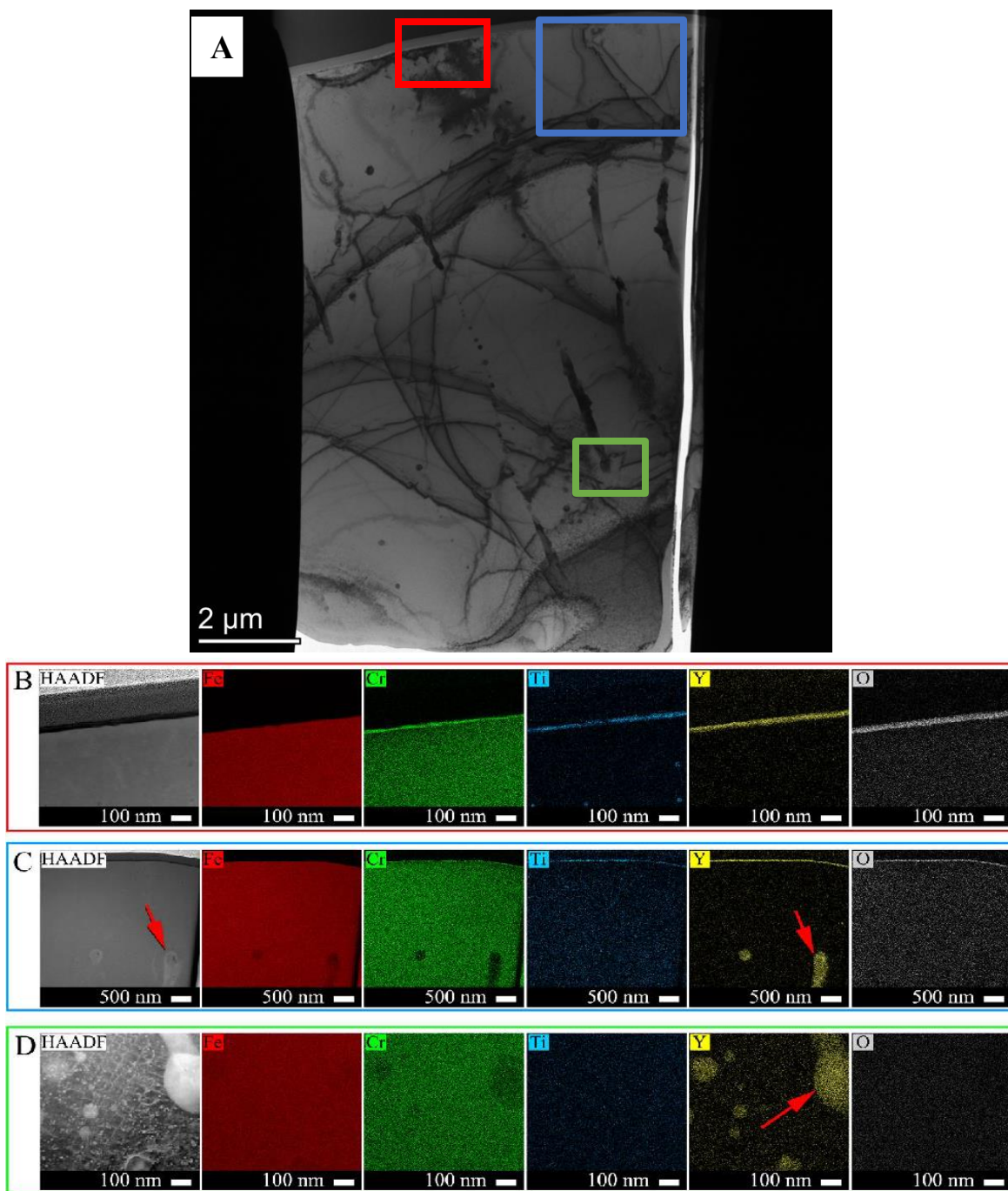


Figure 4.9: TEM image of a liftout harvested from a powder particle (A). The arrows indicate larger areas rich in Y, and the red arrows indicate discontinuous regions rich in Y. The labeled boxes indicate areas analyzed with STEM/EDS (B,C, & D). The STEM/EDS images highlight the distribution of elements in the shell of the powder (B) and the interior (C & D).

X-ray diffraction (XRD) pioneered in 1912 by Max Von Laue, is a tool that is used for identifying and quantitative analyze crystalline peaks in material (as each crystal is a regularly spaced atom, it acts as center of scattering.), which can be used to identify the presence of intermetallic and or elemental composition within the powder or solid sample [176]. When high energy electrostatic and electromagnetic x-ray beams with a wavelength between  $10^{-3}$  to  $10^1$  nm strike the crystal, energy from the impact causes electrons from the outermost shell to eject, which causes a vacancy, which is filled by the transfer of an electron from higher energy levels to lower energy level causing the emission of a photon [176]. The emitted photon wavelength is captured, and information can be obtained from analysis of diffraction peaks which are affected by crystal size, shape, and orientation [177]. XRD pattern was performed on the GARS powder, and LPBF fabricated solid to accurately identify and quantify the presence of nano oxides on the surface of the powder and on the cross-section of the as printed solid sample. Another reason to perform XRD was to identify and quantify the phase shift of intermetallic in powder and solid samples. Results from the analysis are shown in Figure 4.10 A from  $10-80^\circ 2\theta$  with 0.013 step size. The ferrite Fe peaks dominate the spectra, and the effect of the laser PBF on the solid spectrum is observed in the peak positions and relative intensity. The solid sample exhibited peak shifts of -0.09, -0.22, and  $-0.25^\circ$ , for (110), (200), and (211), respectively, as well as the increased intensity in the (200) peak. These effects are most likely related to residual stress in the solid samples from thermal cycling during fabrication. The XRD pattern of the powder showed minor changes compared with powder diffraction standards [00-006-0696].

The insert in Figure 4.10 A shows a scan between  $30^\circ$  and  $44^\circ 2\theta$  that highlights a peak at  $40.2^\circ$  associated with un-melted W in the powder and, barely visible at  $42.8$  degrees, is one of the two main peaks associated with  $Y_2Fe_{17}$ . These small and broad peaks associated with small phase

fractions are difficult to resolve from background signal with standard Bragg Brentano XRD setups, even with long scans and small step sizes. High Energy X-Ray Diffraction (HE-XRD) is a technique that over the years has been used for faster data acquisition for 3D structures. HE-XRD uses high energy sources and devices to generate high-flux high-energy photons ( $>100\text{keV}$ ) that can penetrate through thick materials and bulk environments [178]. There are many advantages of HE-XRD over XRD such as high penetration of bulk material and smaller scattering angle allowing for large range of lattice spacing [178,179]. HE-XRD on GARS powder was performed at advanced photon source (APS) at Argonne National Lab. As Brentano XRD setup was unable to identify with higher certainty and confidence the presence of oxides and W peak against the bulk BCC Fe background, HE-XRD was performed on the powder to resolve this issue, which clearly identified the presence of the  $\text{Y}_2\text{Fe}_{17}$  intermetallic peak was confirmed using HE-XRD. Figure 4.10 B shows the APS HE-XRD data between  $8^\circ$  -  $30^\circ$   $2\theta$ . Here the main peaks for  $\text{Y}_2\text{Fe}_{17}$  located at  $42.507^\circ$  (220) and  $42.795^\circ$  (303), are clearly visible against the background BCC Fe. These data corroborate the previous TEM powder characterization and confirm the presence of Y-containing phases that then dissociate in the LPBF melt pool. In order to investigate the formation of nano-scale oxides from the Cr-166 powders, TEM analysis was conducted to identify the nano-dispersoid elemental composition and size.

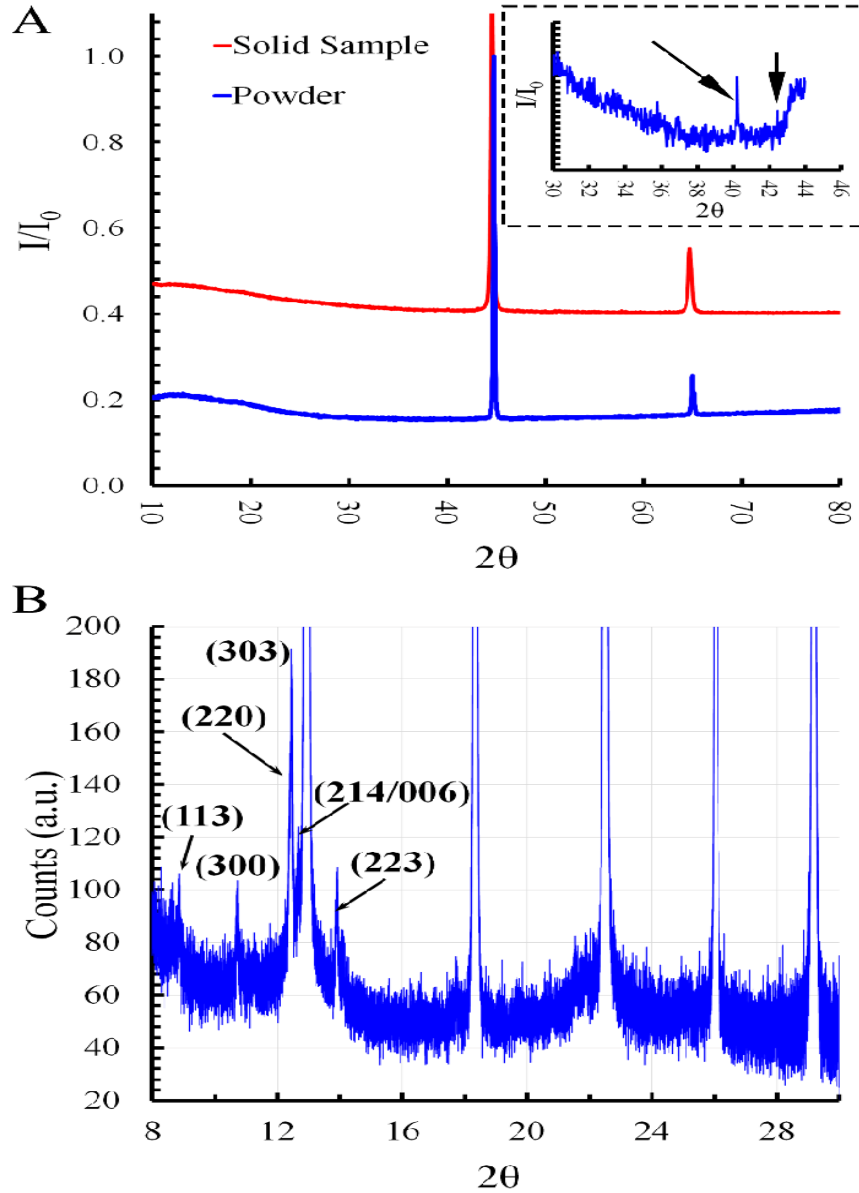


Figure 4.10: XRD results between  $10^\circ$  and  $80^\circ$   $2\theta$  for the GARS powders and LPBF fabricated solids (A). The inset in 'A' shows a higher resolution scan between  $30^\circ$  and  $44^\circ$   $2\theta$ . HE-XRD scans from APS beamline 11B confirm the presence of the  $Y_2Fe_{17}$  in the powder (B).

#### 4.4.2 Solid Sample Characterization

For each steel insert containing seven LPBF samples, the steel insert was cut with a liquid cooled alumina blade (for metallurgical prep). To improve the efficiency of sample prep, where possible samples were cut from the insert in pairs. As shown in Figure 4.11, the LPBF samples were then cross-sectioned perpendicular to the long dimension (resulting in a 7.5mm x 4 mm area

cross-section for each test condition). A 4mm thick slice of this cross-section was prepared from the right half of the sample for metallurgical evaluation. This was potted in 25mm diameter cold-mount epoxy (MarkV). The samples were progressively ground and polished using a Beuhler Ecomet 30 Automatic polisher. The rest of the right-hand sample was retained for future study. The left hand samples were progressively ground to 600grit and used for microhardness indentation studies.

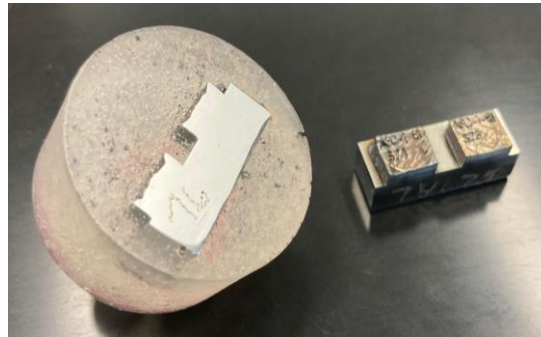


Figure 4.11: Photograph showing a pair of LPBF samples after extraction from the insert and sectioning (right) and after cold mounting, grinding, and polishing.

The sample cross-sections were imaged on a digital optical microscope (Hirox) at 100X magnification. Tiled images were generated from each sample using the built-in Hirox tiling software. The tiled images were exported in .tif format to imageJ. The region of interest of the sample (7.5mm x 3.5mm) was cropped excluding the sample edges. The images were thresholded using the auto-threshold feature (note  $\pm 15\%$  variation in the thresholding was also carried out and only resulted in  $\sim \pm 2\%$  in the relative density measurements). The imageJ particle analysis toolpak was then used to calculate the area fraction of the observed porosity in the cross section and subtracted from the total area to obtain the 2D relative density of the samples (note this is the value most commonly reported in the AM literature) [180,181].

Figure 4.12 shows a collage of the tiled images from the samples fabricated in the “Argon” atmosphere group as an example. The first column shows samples fabricated with a 0.03mm hatch

spacing, the middle column shows samples fabricated with a 0.05mm hatch spacing and the third column shows samples fabricated with a 0.08mm hatch spacing. The beam speed variable decreases from the top row to the bottom row. To reiterate, the purpose of these experiments was to span the entire process space, so it was intended that some samples fail, some samples be porous, and that some samples fall within the process window. Sample S11, for instance, has a large hatch spacing and a high beam speed, consequently the energy input was very low and the sample was porous. From these images, and the associated relative densities, we can also see that samples S2, S3 and S10 show considerable promise. These samples had a relative density of above >98% and analysis of recorded video revealed that these samples were stable throughout the printing process and were hence crucial to identify the feasible process space. Further microCT analysis was performed on samples S2 and S10 to confirm the result obtained via optical density analysis.

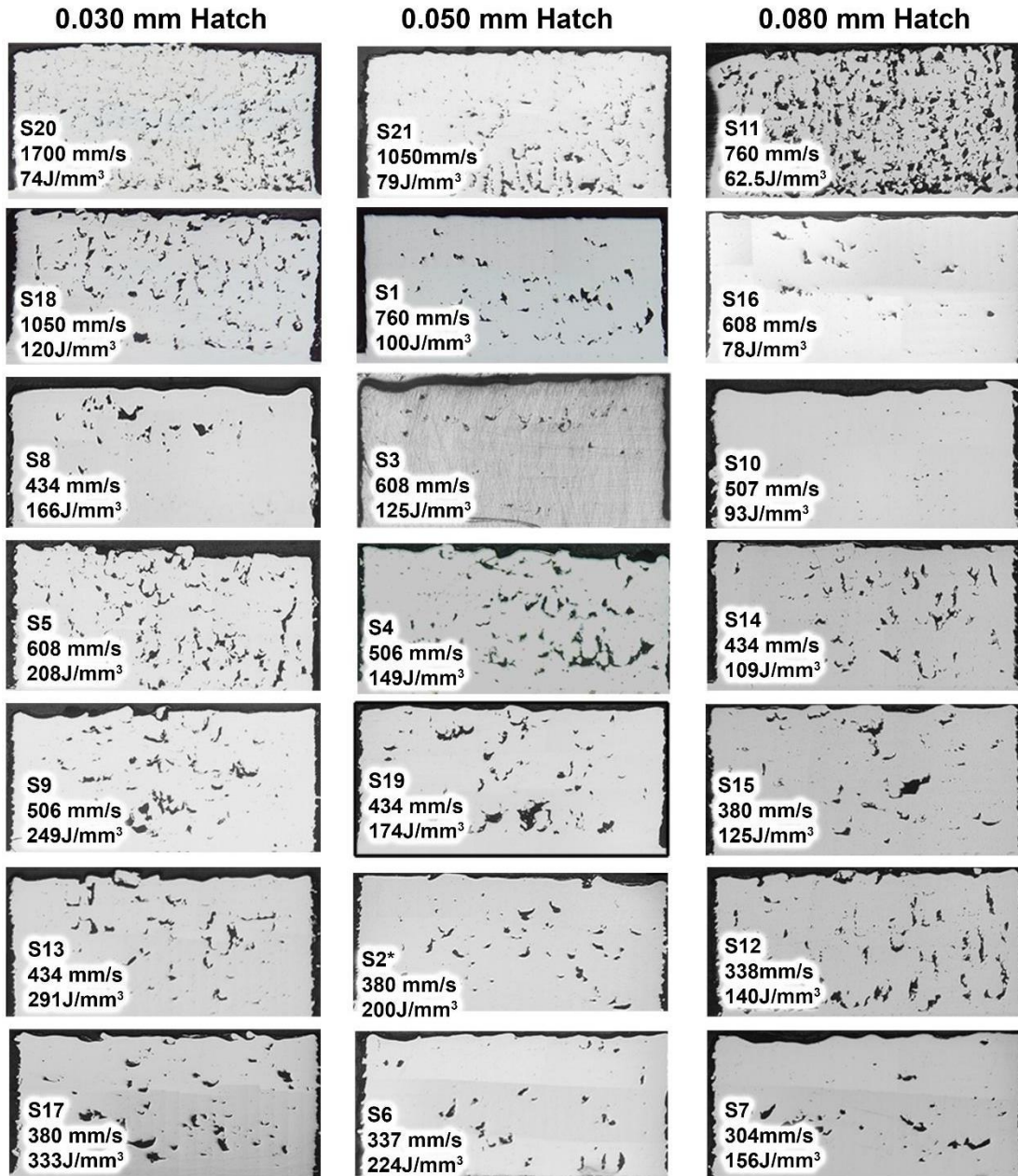


Figure 4.12: Optical microscope image tiles from the “Argon” atmosphere case across various speed and hatch spacing combinations.

The numerical value in the bottom left corner of each tile in Figure 4.12 is the volumetric energy density. The volumetric energy density,  $E(\text{J}/\text{mm}^3)$ , is often represented by the simple expression,  $E = P/vht$ , where  $P$  is the laser beam power,  $v$  is the beam velocity (mm/s),  $h$  is the hatch offset (mm), and  $t$  is the layer thickness (mm), and is a common means by which to visualize the

processing space for a given alloy or set of conditions. The plot in Figure 4.13 shows the influence of the volumetric energy density on the optically measured 2D relative density of all samples across all parameters and atmospheric conditions. There is a convex trend that appears where below some critical value, the relative density drops sharply. Analyzing the graph, it can be noticed that the value in this case is roughly 100 J/mm<sup>3</sup>. Then a stable region in which high density can be achieved followed by a high energy density region in which the relative density is reduced either by process instabilities (e.g. sample swelling) or the formation of keyhole porosity (from evaporated metal). This graph helps to identify a suitable working process space which is devoid of any process defects and is also dense and hard.

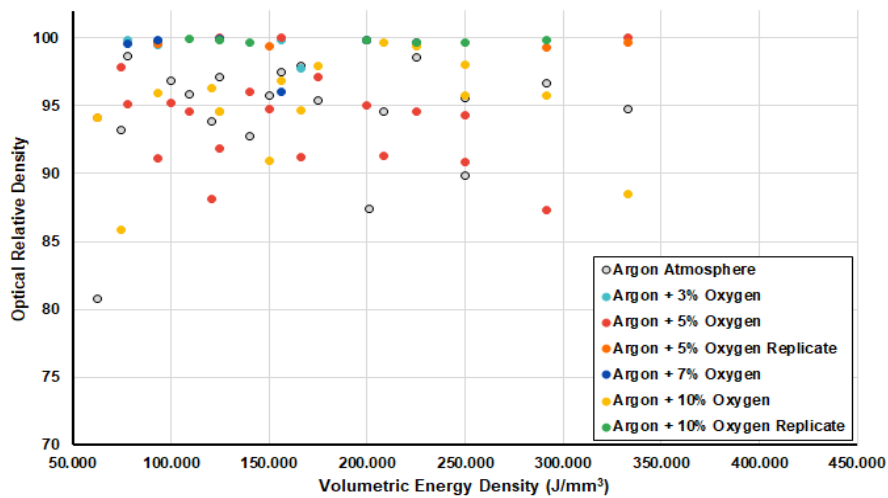


Figure 4.13: Measured optical relative density as a function of the volumetric energy density ( $E=P/vht$  J/mm<sup>3</sup>).

The following Figures (4.14-4.18) show maps of the volumetric energy density (J/mm<sup>3</sup>) as a function of beam velocity for each of the atmospheric conditions that was studied. Lines of constant hatch spacing are plotted and the experimental data are colored according to the measured relative density. These data provide a compiled visual representation of the entire processing space and identify the most promising regions of interest for further evaluation. As it can be seen from the graphs, for all the conditions, the optimal beam speed and hatch spacing that yield good results

(>99% RD) lie in between 400 - 600 mm/sec and 0.05mm respectively. In the case of Argon (Figure 4.14) a region along the 0.05mm hatch spacing line with beam velocities between 400 mm/s and 800mm/s resulted in samples with the highest relative density (>99%). The samples in the Ar+3%O<sub>2</sub> experiment (Figure 4.15) all exceeded 99% relative density, note again that these samples and those in the Ar+7% experiment (Figure 4.17) were intentionally carried out using only the “best” parameters from previous trials. The data in Figure 4.16, for the Ar+5% case follow a similar pattern to the Ar case, here again the highest density samples are typically found along the 0.05mm hatch line. The data from the Ar + 10% experiments tended to be much more scattered with several samples achieving high relative density.

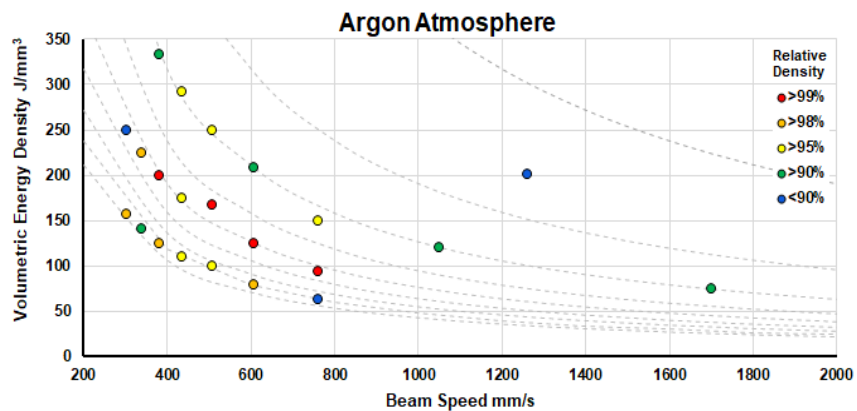


Figure 4.14: Plot of the volumetric energy density ( $E=P/vht$  J/mm<sup>3</sup>) as a function of the beam velocity for LPBF samples produced in an Argon atmosphere.

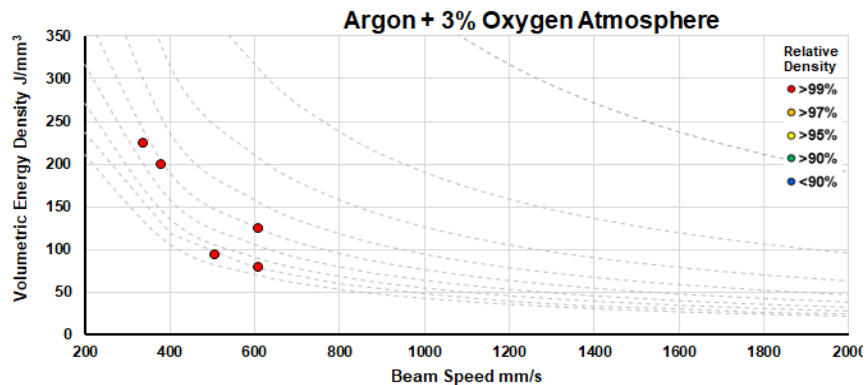


Figure 4.15: Plot of the volumetric energy density ( $E=P/vht$  J/mm<sup>3</sup>) as a function of the beam velocity for LPBF samples produced in an Argon + 3% oxygen atmosphere.

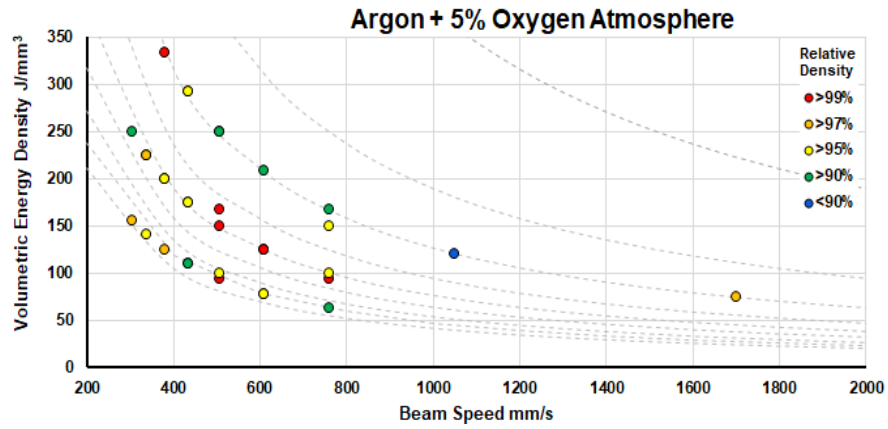


Figure 4.16: Plot of the volumetric energy density ( $E=P/vht$  J/mm<sup>3</sup>) as a function of the beam velocity for LPBF samples produced in an Argon + 5% oxygen atmosphere

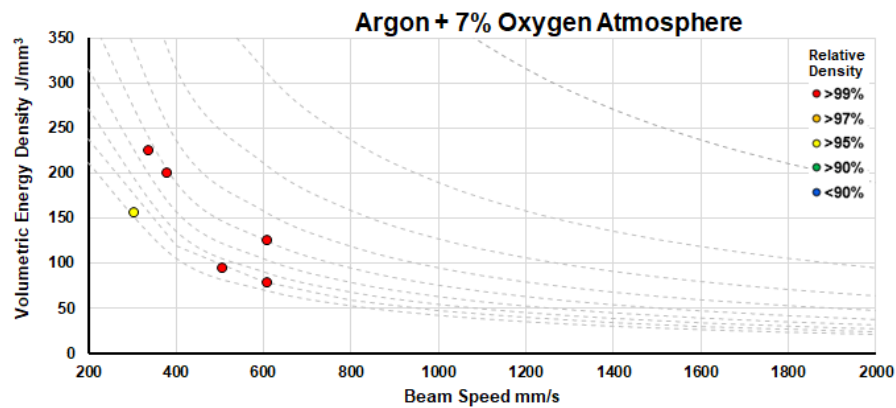


Figure 4.17: Plot of the volumetric energy density ( $E=P/vht$  J/mm<sup>3</sup>) as a function of the beam velocity for LPBF samples produced in an Argon + 7% oxygen atmosphere

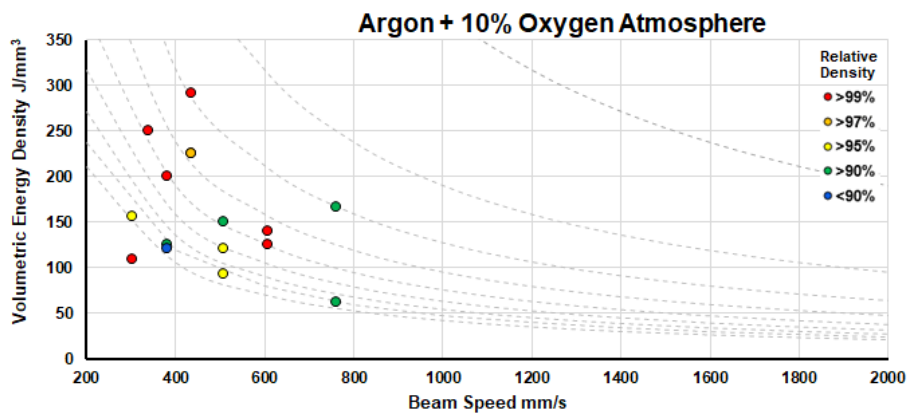


Figure 4.18: Plot of the volumetric energy density ( $E=P/vht$  J/mm<sup>3</sup>) as a function of the beam velocity for LPBF samples produced in an Argon + 10% oxygen atmosphere

Relative optical density gives an idea of what the density of the sample might be but as it is the representation of only a single slice, it is not a representative data set. In order to create a process map, around 100+ samples were successfully fabricated. To relate optical density to actual part density, selected samples were microCT imaged using the ZEISS Xradia 510 Versa X-ray microscope using the following parameters: Objectives: 0.4X, Pixel Size: 6.0546 microns, Voltage: 160 kV, Power: 10 W & Exposure Time: 7s. As doing microCT of a single sample is time consuming and expensive, from the tiled images of the cross sections, three samples were selected for initial micro-CT analysis. S10 (Figure 4.19) and S2 (Figure 4.20) were chosen because they both exhibited high relative density in the optical cross sections. Sample S71 (Figure 4.22) also exhibited high density, but also indications of keyhole (high energy) induced porosity in regions and was investigated further. Figure 4.19 shows several views of Sample S10 which was produced in an Argon atmosphere with a hatch spacing of 0.08mm and a beam speed of 507mm/s. In this instance, it is evident that the sample is indeed highly dense, (note that the voxel resolution is  $\sim 6\mu\text{m}$ , therefore defects below this size are not detectable using this method). Subsequent SEM imaging reveals the absence of micro-scale porosity. The micro CT imaging of sample S2 is shown in Figure 4.20. This sample was also processed in argon, with a beam speed of 380mm/s and a hatch spacing of 0.05mm. Both the micro CT and the optical images showed regions of high density, however, the microCT also identified discrete pockets of large porosity. Subsequent review of the fabrication video (Figure 4.21) taken during processing shows that these defects most likely occurred as a result of a powder spreading error. That is the pores are less likely associated with the process maps compared with a general process instability that could be optimized in future trials.

Figure 4.22 shows sample S71 which was processed in a 10% oxygen atmosphere with 0.05mm hatch spacing and 338 mm/s beam speed. In this case, relatively large pores, circular pores were observed toward the edges of the sample, this is typically indicative of the formation of keyhole porosity which is the result of excessive laser heat input. When the process parameters are on the edge of the keyhole space, the pores are most commonly located at the periphery of the part where the beam reaches the part edge and reverses on its self. The short time gap for this overlap causes a significantly higher local energy input in these regions. In examining the keyhole porosity in sample S71 Figure 4.22 D-F it is evident that the steady-state regions are dense and pore free, especially within the 10mm x 10mm island areas, however along the periphery of the sample and the periphery of the island region many instances of keyhole porosity are observed. Figure 4.22G-I is a 3D reconstructed image of pores w.r.t to the scanned part. It is again evident from the reconstructed images that the keyholing is prominent around areas of laser overlap. Figure 4.22G is a representation of pore size in the as scanned sample. Pore sizes vary from 16.98um to 1064.67um. He et al. studied the effect of oxygen concentration on weld pool and keyholing on SS 304 in a laser beam welding system. In their experiment, using a mathematical model, they simulated the effect of varying concentrations of oxygen from 0 – 20% and the effect that it has on flow within the melt pool. He et al. observed that with an increase in oxygen concentration in the shielding gas, the critical temperature point of the weld increased, which suppressed the temperature gradient causing it to change. They are theorizing that this change in the temperature gradient prevents melt pool flow near the keyhole wall, thus suppressing the collapse of porosity formation [182]. Leung et al. reported a similar observation where they studied the effect of defect formation with different levels of powder oxidation in a laser additive manufacturing system. They are theorizing that oxide films at the pore surface might act as a gas pocket, thus altering the

interfacial energy in the molten pool by altering the Marangoni driven forces, which in turn restricts the melt pool movement [183]. Bertoli et al. on the other hand, reported no apparent change in the melting behavior of 316L powder prepared by GA (Gas Atomization) and WA (Water atomization), with WA powder having higher surface oxygen and sulfur level [184]. As all three samples S2, S10 and S71 were printed with the same process parameter but different atmospheric conditions, it supports what is reported in various other literature. All of these and other research are mainly focused on oxidation in chamber or surface oxidation level in powder to demonstrate a correlation between oxygen and or sulfur content to defect formation. For the particular set of experiments using GARS powder conducted at CAMAL in NC State University, as both the powder and chamber have oxygen concentration, a detailed CFD and heat transfer mathematical model needs to be analyzed that takes into consideration the effect of oxygen from surface as well as environment to the melt pool flowability. The takeaway from these data are that while this specific example was outside the process space, further optimization of the beam scan pattern and turn-around shuttering profiles could result in very high density samples under these conditions.

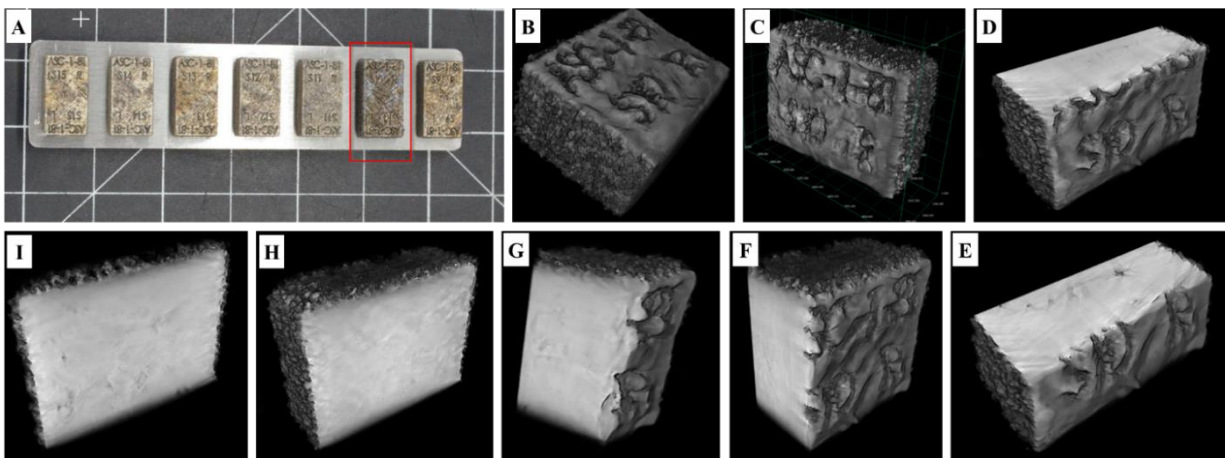


Figure 4.19: Photograph of sample S10 from on the steel build insert (A) and microCT images showing high sample density (B-I)

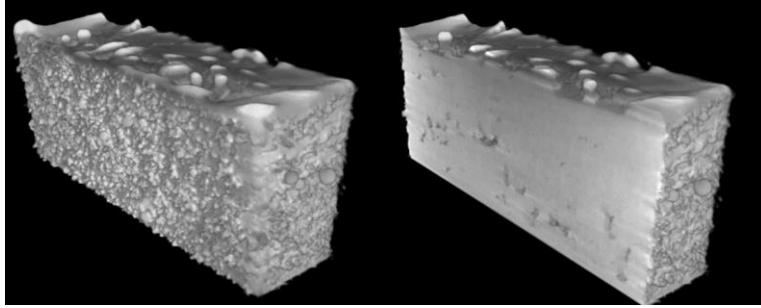


Figure 4.20: microCT images showing regions of high density and pockets of large scale porosity in sample S2 that are likely the result of a layer spreading defect.

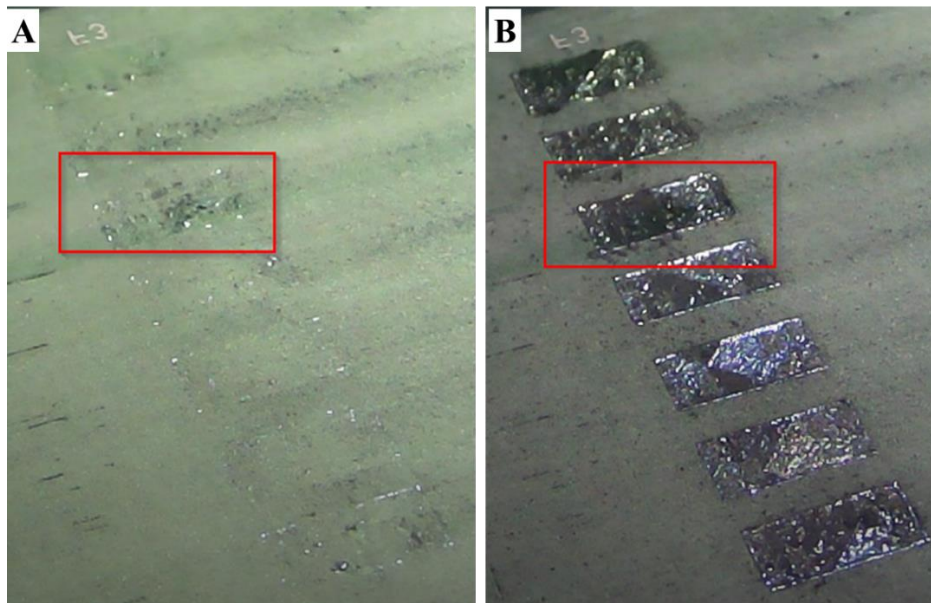


Figure 4.21: Highlighted box shows sample S2 after powder application (A) and the final printed layer (B).

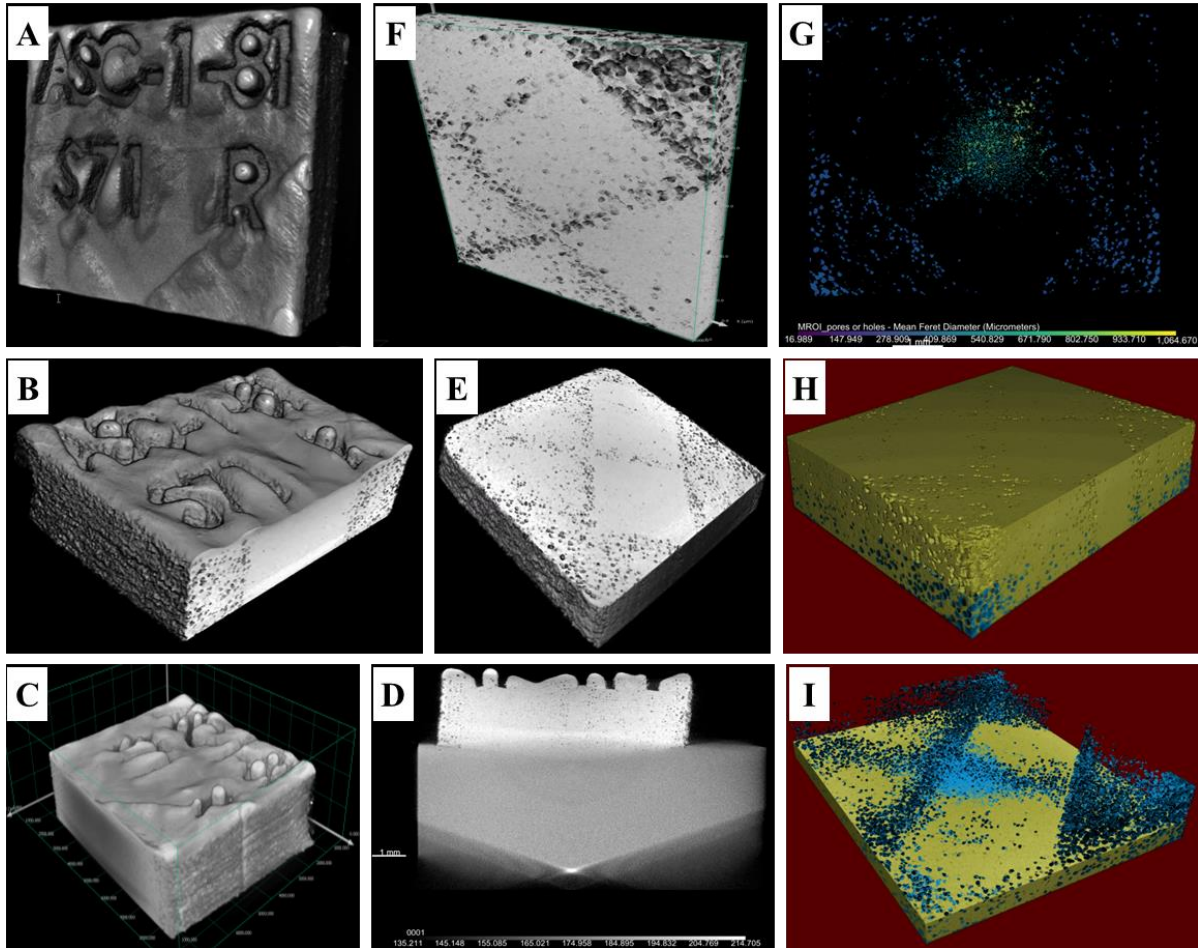


Figure 4.22: MicroCT images of S71 showing high sample density (A-D). The extensive keyhole porosity in E-I is only apparent at the periphery of the scan line length islanding regions indicating that the steady state parameters for S71 are within the process window.

A LECO M400 Microhardness tester with a diamond indenter was used for microhardness measurements which were obtained from a sectioned region of each sample. 12 indentations were taken from each sample using a 500 gram force load was used for a dwell time of 10 seconds. Vickers hardness was calculated using digital optical microscope images of each indentation. Figure 4.23 shows the average and standard deviation for all samples grouped by the atmospheric condition. In all cases the hardness values ranging from >200HV are significantly higher than those reported previously in the AM literature. In chapter 3, for Cr-166 powder Horn et al., reported an average hardness data of  $147.0\text{HV} \pm 27.2$  from the argon region,  $148.3\text{HV} \pm 25.4$  for the region

produced in 1%O<sub>2</sub>, 160.8 HV ± 17.8 for the region produced in 5% O<sub>2</sub>, and 170 HV±10.7 for the region produced in air [99]. This is significantly lower than the values obtained from ASC-1-81 powder batch. It can be noted that for Cr-166 powder batch, there was a visible trend in the increase of hardness value with increase in oxygen condition in the print chamber. For ASC-1-81 powder, there is no significant variation in the results. Horn et al using Cr-166 powder had theorized that an increase in oxygen in the chamber favored the formation of chromium rich oxides over yttrium and titanium oxides [99]. For GARS ASC-1-81 batch, as the powder already has a Y-Ti-O rich crust (Figure 4.9), it can be theorized that instead of forming a stable oxide inside the melt pool, Yttrium and Titanium oxide are already present in the oxide stage in the powder. SEM images of solid samples S2 (Figure 4.26) and S64 (Figure 4.27) which were fabricated in Argon and 10% O<sub>2</sub> respectively condition shows Chromium oxide rich areas along with Yttrium and Titanium oxides. As even the samples fabricated in Argon are Chromium oxide rich, this hypothesis might explain why all the samples fabricated under different chamber conditions have similar hardness values.

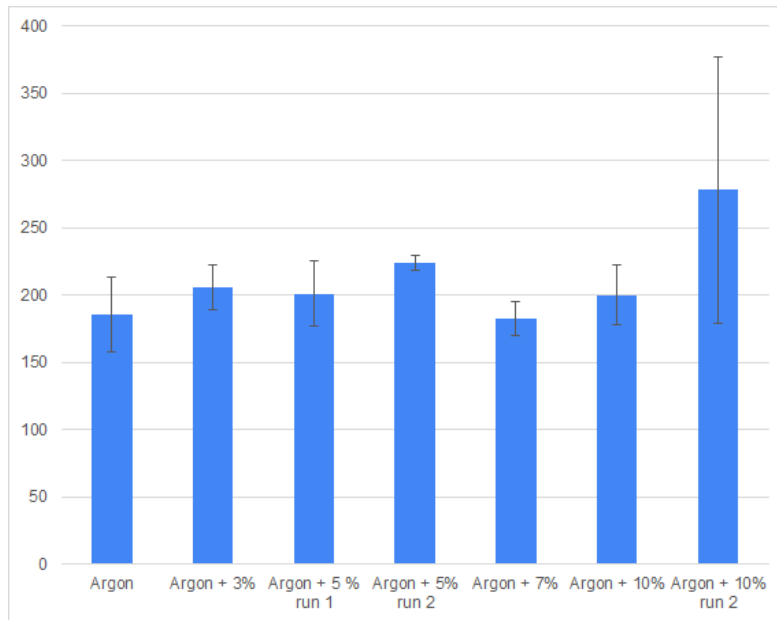


Figure 4.23: Bar graph showing the hardness of all samples (S1-S92) grouped by the atmospheric condition during LPBF (error bars indicate one +/- standard deviation from the mean).

Scanning electron microscope images were acquired for two of the LPBF samples. Figure 4.24 shows a representative backscatter (compo) image of a region of sample.

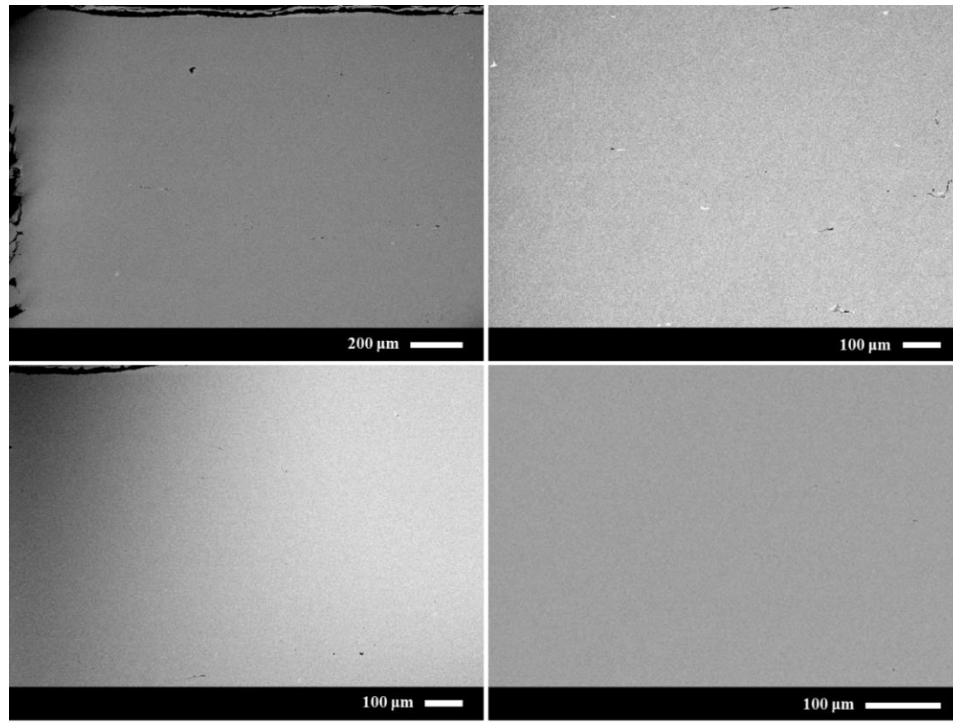


Figure 4.24: Representative backscatter electron microscope image from sample S2 produced in an argon atmosphere during LPBF.

Figure 4.25 shows a region that contains 5-10 $\mu$ m wide Y-Ti-O oxides indicated by the yellow arrows and visible as bright white regions in the backscatter image. This observation was similar to the previous Cr-166 trials, but in this case the oxides are much smaller and much less prevalent. Using imageJ to isolate the oxides, the 2D area fraction of the oxides is <0.015%, significantly less than the previous trials. Microscale porosity not resolved by the optical microscopy is highlighted by the yellow circles in Figure 4.25. As was observed in the Cr-166 trials, the regions rich in microscale oxides are often associated with-or in the vicinity of lack of fusion defects.

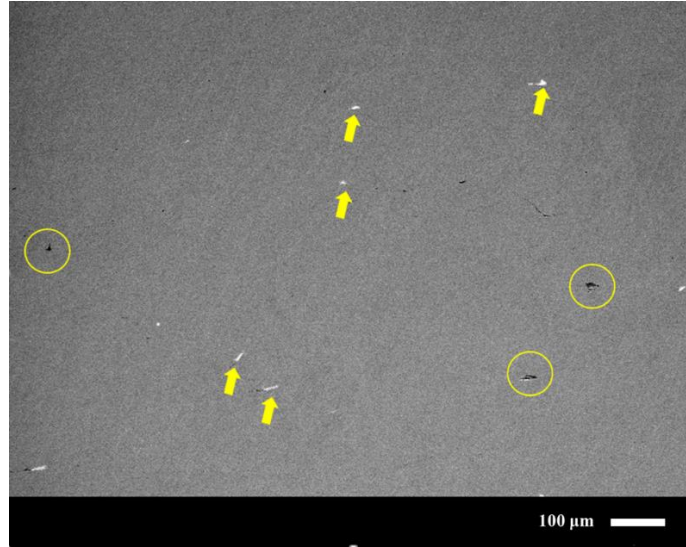


Figure 4.25: Backscatter electron microscope image from sample S2 from a region exhibiting micro-scale Y-Ti-O inclusions indicated by yellow arrows. Microscale lack of fusion porosity was also observed, but was not prevalent, and is indicated by the yellow circles.

As indicated by the micro-CT data, while sample S2 overall exhibited a high relative density, there were pockets of larger scale pores. Figure 4.26 shows a backscatter electron image of one of these regions with the associated energy dispersive spectroscopy (EDS) maps showing a Ti-Y-O region in the vicinity of one of the lack of fusion defects.

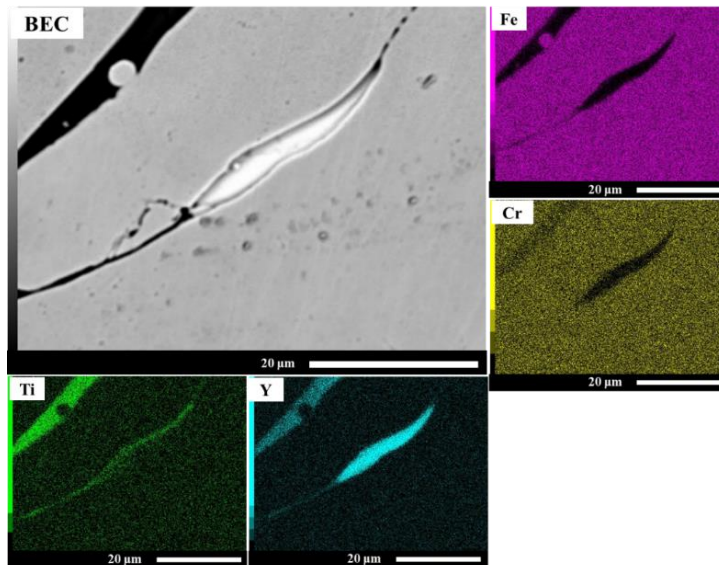


Figure 4.26: Backscatter electron microscope image from sample S2 from a region exhibiting micro-scale oxide inclusions in the vicinity of lack of fusion defects and, the EDS maps indicate these are rich in Ti-Y-O.

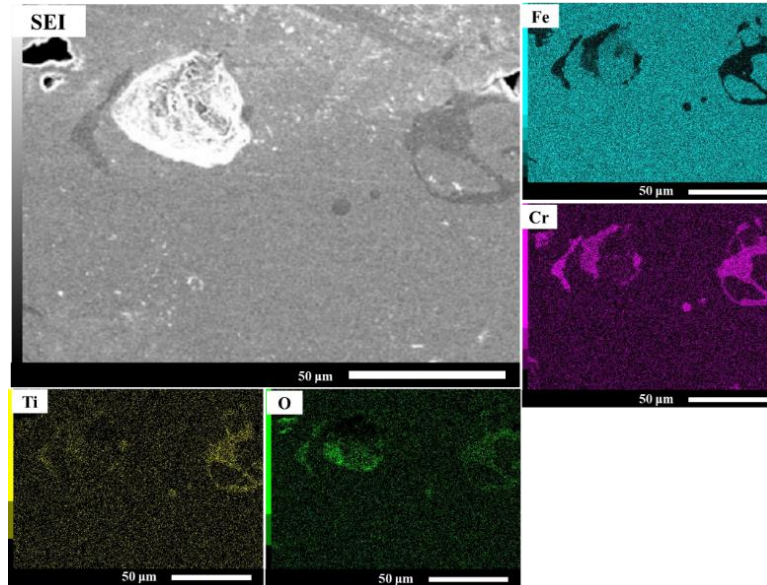


Figure 4.27: Secondary electron microscope image from sample S64 from a region exhibiting micro-scale oxide inclusions in the vicinity of lack of fusion defects, the EDS maps indicate these are rich in Cr-Ti-O.

An EBSD reconstructed IPF map of a typical solid, S2 is shown in Figure 4.28 where the anisotropic grains are observed in the build direction, typical of AM fabricated materials. Crystallographic texture is observed in the  $\langle 111 \rangle$  and  $\langle 101 \rangle$  directions as indicated by the red and blue grains in Figure 4.28 and in the 001 pole figure.

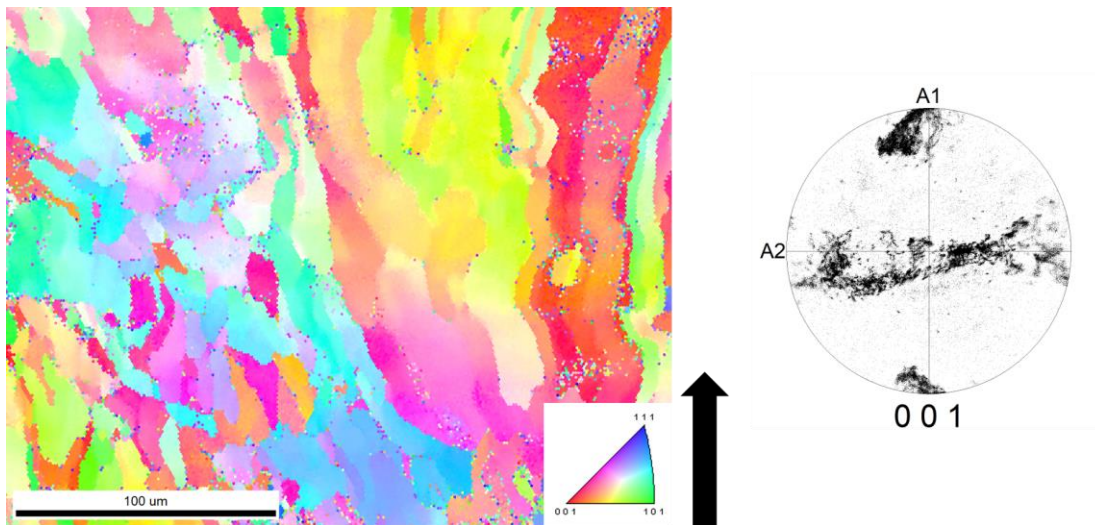


Figure 4.28: Electron Backscatter Diffraction image of representative ASC1 1-81 Solid fabricated with LPBF (500x 0.4um step). Reconstructed IPF Map (left) and Pole Figure (right).

Figure 4.27 shows the backscatter SEM image and associated EDS maps for sample S64 that was produced in the argon +10% oxygen atmosphere. It has been theorized that due to abundance of oxygen in the 10% oxygen atmosphere condition, thermodynamically the sample favors the formation of chrome-oxides which are visible as the dark gray regions in the backscatter image and confirmed by EDS.

Figure 4.29 is a HAADF image showing the FIB liftout from Sample S10 and one of several locations used for oxide measurement identified by the rectangle in A. Figure 4.29 B shows thickness maps of the TEM lift-outs which were obtained using Electron Energy Loss Spectroscopy (EELS) used to calculate particle densities. The STEM/EDS images shown in Figure 4.29 C identify spherical oxide particles are depleted of Fe and rich in Ti and Y. No Fe-Y phases were observed in any liftouts or in any SEM analyses. Thickness was calculated using the zero loss method using the Digital Micrograph script developed by Malis et al. [159]. The electron Mean Free Path (MFP) was obtained for the regions of interest and converted into a thickness using the method which relies on the mean atomic number based on the composition. The error in thickness measurement is estimated to be ~10%. Figure 4.30 D shows the size distribution of measured particles by TEM, where the 10<sup>th</sup> and 90<sup>th</sup> size percentiles range from 17 – 57 nm with a median value of 34 nm and oxide density of  $1.8 \times 10^{20} / \text{m}^3$ .

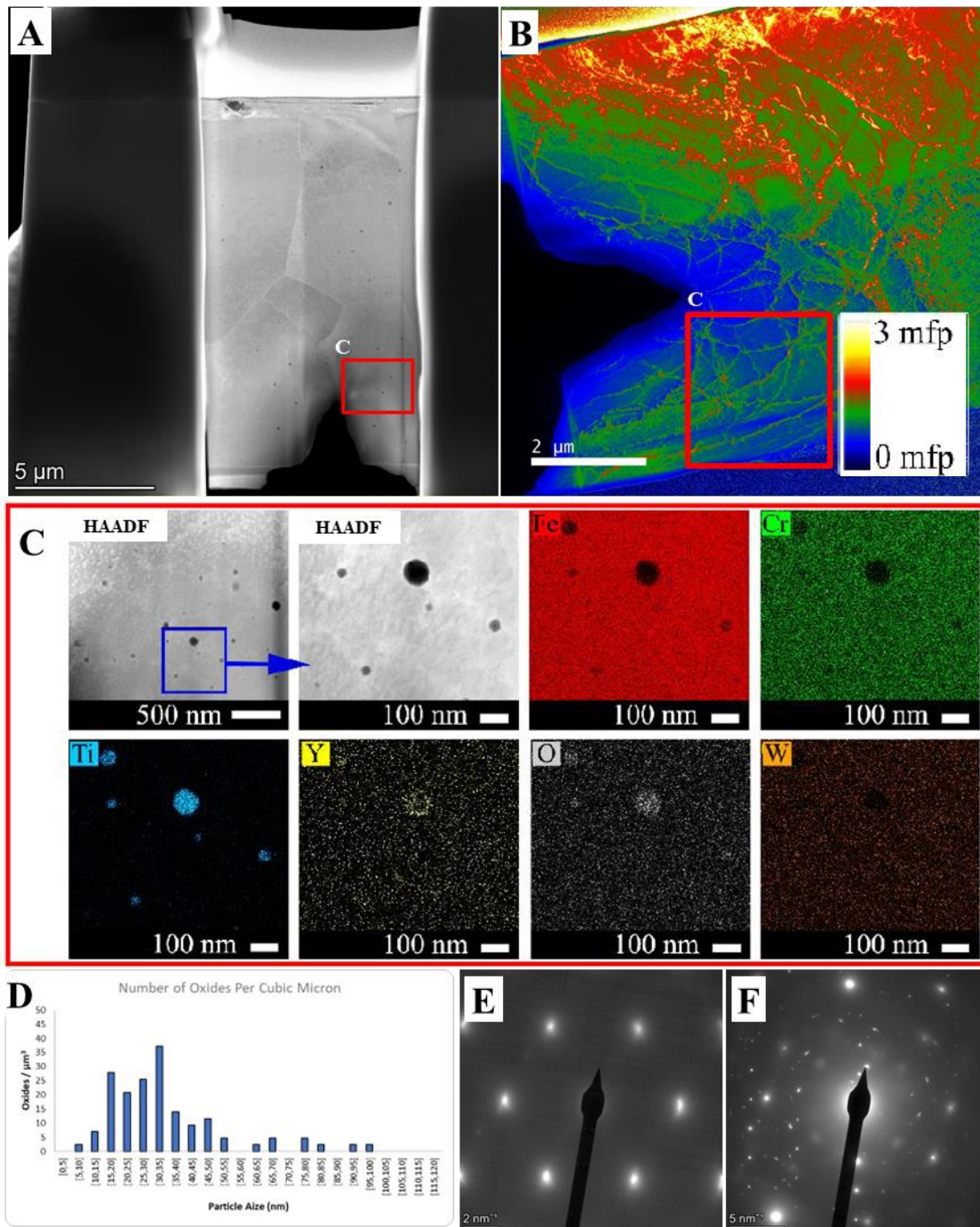


Figure 4.29: HAADF image of the liftout (A), the red box indicates the region of the STEM/EDS analysis shown in (C). EELS mfp map used to calculate the liftout thickness in the region of interest (B). The size distribution of oxides combined from multiple measurements on the liftout (D), and SAED patterns identifying the BCC Fe matrix and the Ti<sub>2</sub>Y<sub>2</sub>O<sub>7</sub> particles.

The inset SAED maps in Figures 4.29 E and 4.29 F identify the BCC Fe matrix (E) and the nano-oxide pyrochlore phase,  $Ti_2Y_2O_7$  (F), which also captures a small amount of the matrix symmetry mixed within the pattern. This oxide phase is consistent with studies in Fe-14YWT and similar alloys where the MA alloyed yttria and rutile particles transform into complex Ti-Y-O oxides during high temperature processing such as thermo-mechanical processing and hot isostatic processing (HIP). Studies by Rieken et al. reported that GARS powders with similar compositions formed  $Ti_2Y_2O_7$  after HIP due to favorable free energy of formation at high temperature [9–11]. In our study, the observation of spherical oxides in the fabricated solid indicates the intermetallic  $Y_2Fe_{17}$  and chromium oxide crust initially observed in the GARS powder, successfully disassociated in the laser PBF melt pool and reacted to form the intended nano oxide particles rich in Ti and Y.

#### 4.4.3 Large Block Fabrication

After analyzing the process space map, SEM and MicroCT data, 15mm x 15mm x 25 mm samples were produced using process parameters within the dense processing space for the inert and reactive environment. Figure 4.30 shows photographs of the as-fabricated samples produced by LPBF in inert environment (A) and in reactive environment Argon + 3% O<sub>2</sub> (B). Note, the sample on the right was cross-sectioned before the image was taken.

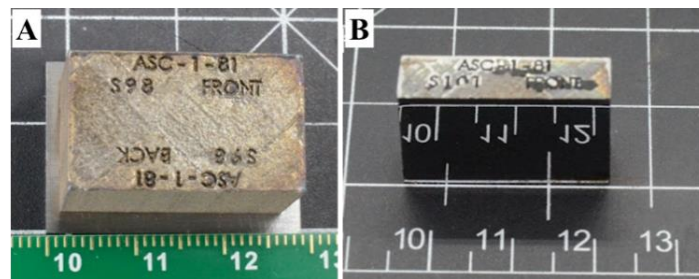


Figure 4.30: Photograph of two LPBF fabricated test articles with dimensions 25 x 15 x 15 mm. Samples were built using 608mm/sec and a hatch spacing of 50um. Sample on the left was fabricated in inert environment (A) and in reactive Argon + 3% O<sub>2</sub> (B)

Figure 4.31 is a stitched back scatter electron image (BSE) taken on Thermo Fischer Helios 5 Hydra CX. Regions of micro porosity are highlighted in 4.31 (B). It is evident that the pores are minuscule in comparison to the big block. The sample produced was  $\geq 99\%$  relatively dense thus confirming the scalability of the identified parameter from the process space.

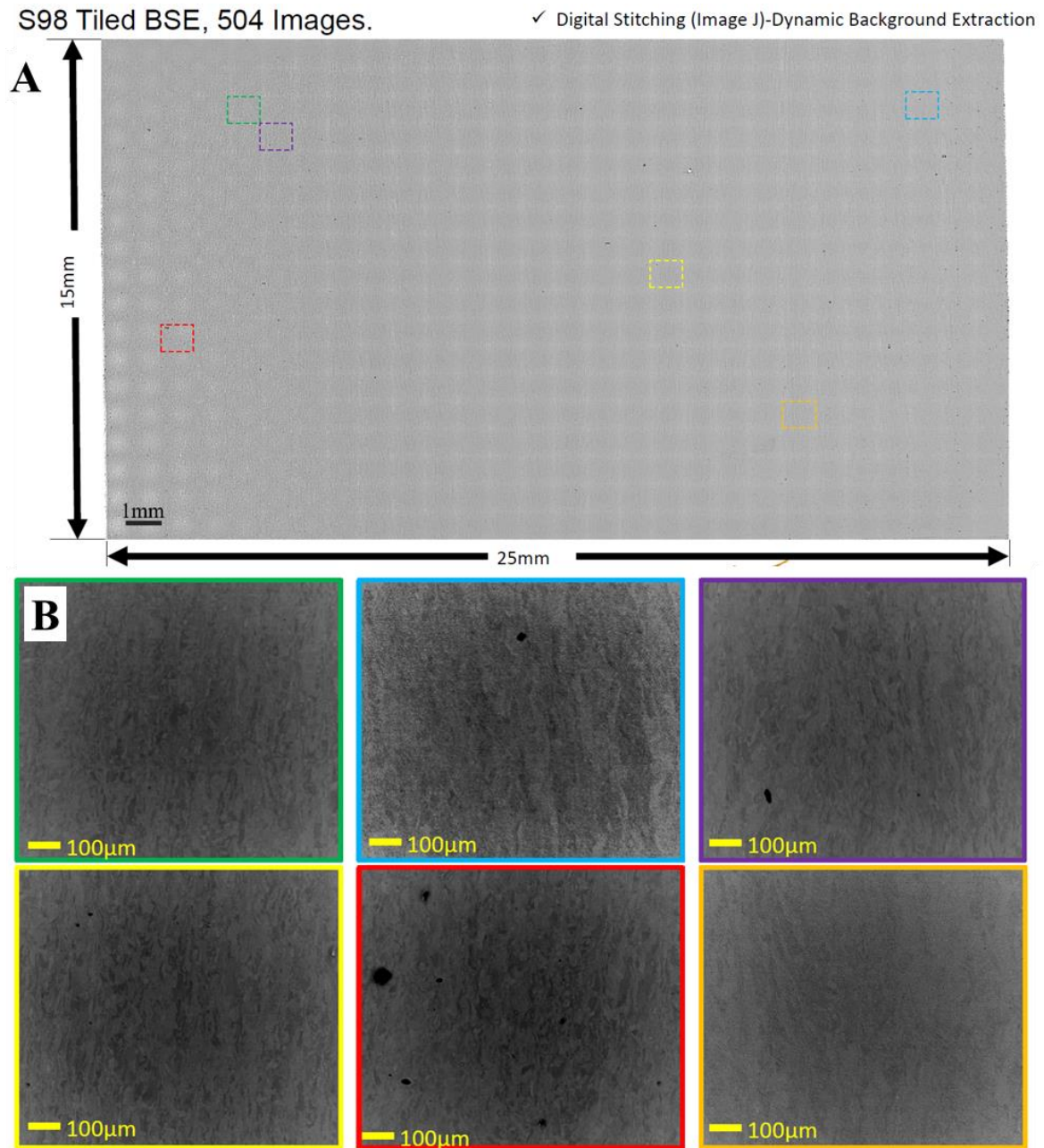


Figure 4.31: BSE tiled image of S98 (15mm x 15mm x 25mm) sample printed in inert environment (A) and zoomed in image of areas depicting porosity in the micron level (B)

Figure 4.32A is an inverse pole figure (ipf) map of a representative low magnification area accompanied by a pole figure showing crystallographic texture in the  $\langle 100 \rangle$  direction and is typical of AM- fabricated materials with epitaxial grain growth. Figure 4.32 B is a backscatter SEM image at a high magnification that reveals a matrix with structures of slender grain boundaries, with the grains in the range of 3-5  $\mu\text{m}$ . in width. These particles were observed to be non-agglomerated and homogeneously distributed throughout the matrix and not preferentially located along grain boundaries.

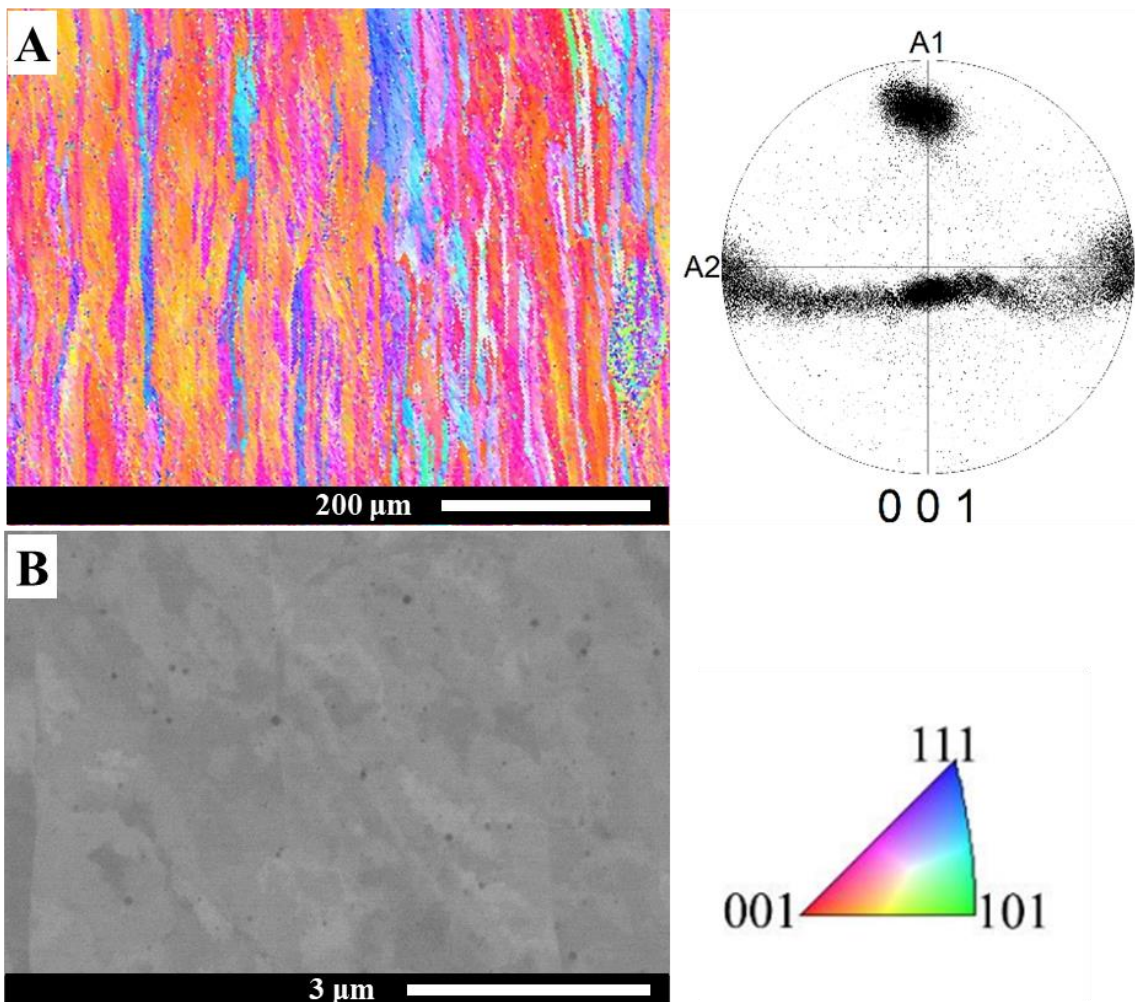


Figure 4.32: EBSD low magnification inverse pole figure (ipf) map for S98 showing a strong texture in the  $\langle 100 \rangle$  direction (A), and a high magnification backscatter SEM image of a region enlarged from Figure 4.31 B showing a distribution of low-density particles (B).

#### 4.4.4 Tensile Tests

The same parameter used to fabricate 15mm x 15mm x 25mm prismatic samples was used to fabricate 14mm x 80mm x 8mm tensile samples in inert atmosphere. Figure 4.33 depicts the as-fabricated tensile sample in the horizontal direction. Samples were fabricated in the horizontal orientation due to the limited quantity of powder. As a result, the columnar grains are oriented perpendicular to the loading direction. Tensile specimens harvested from the 14 mm x 80 mm x 8 mm were tested to failure. Figure 4.34 (A) depicts the CAD model of the tensile bar, and 4.34 (B) depicts the as EDM cut bars with a gauge width of 3mm.

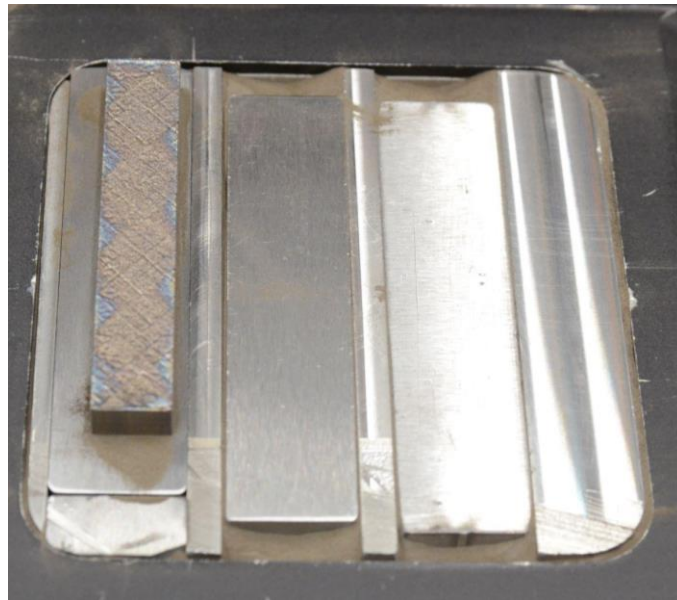


Figure 4.33: Photograph of LPBF fabricated tensile bar stock with dimensions 14mm x 80mm x 8mm.

Figure 4.35 depicts the samples being subjected to uniaxial loading in tension at room temperature on an ATS model 1620C by Applied Test Systems Inc with a crosshead speed of 0.1mm/s and a 5kN autocorrected load cell. Digital Image Correlation (DIC) was performed to map surface displacement fields during testing and calculate strain using GOM correlate (2021 Hotfix 3, Rev 144264). A black and white speckle pattern was applied to the gauge section and images were recorded using a Sony IMX74 monochromatic grasshopper 3 USB 3 (Model: GS3-

U3-23S6M-C) with a 2.3 MP camera at a rate of 1 frame per second. Figure 4.36 shows the progression of DIC strain development for the entire test phase from start (0min), mid (45 min), and just before fracture at 95min. GOM correlate uses DIC and point tracking algorithm to contactlessly measure strain and displacement over elastic and plastic phases. To analyze the sample, a surface component was selected such that the entire area of interest (gauge area) was highlighted, and using the virtual extensometer feature (used to track strain along the selected gauge area), the software generated the strain map (Figure 4.36) along Y direction for the tensile bar. Using the strain values generated by the virtual extensometer, and the stress values from the UTS tester, we generated the stress-strain plot as well as measured the yield strength of the sample. The average UTS and yield strength was 474MPa and 312MPa respectively, and the total elongation was 26.8%. This value is below the ~600MPa value reported by Rieken et al for GARS-166 samples fabricated using HIP [9]. A sample coupon was cut along the build direction to measure the microhardness value of the as-fabricated sample in multiple locations. The average Vickers hardness value of the sample was measured at 236.6 HV.

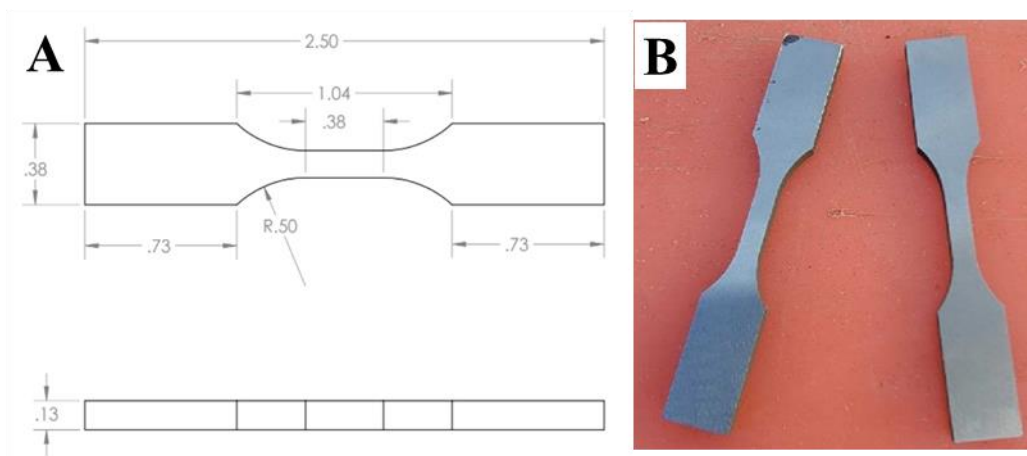


Figure 4.34: Photograph of the CAD model of the tensile bar (A), as EDMed 2 tensile bars from the large tensile sample (B).

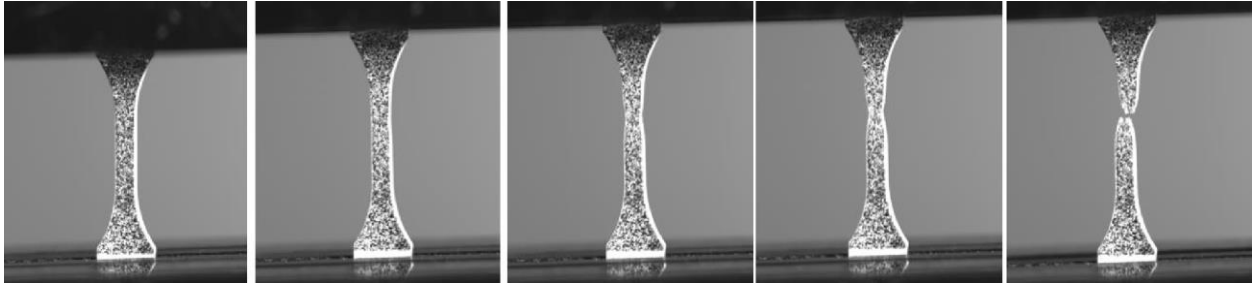


Figure 4.35: Grasshopper images of tensile sample being pulled in the lateral direction. As mentioned, pulling direction was perpendicular to the build direction.

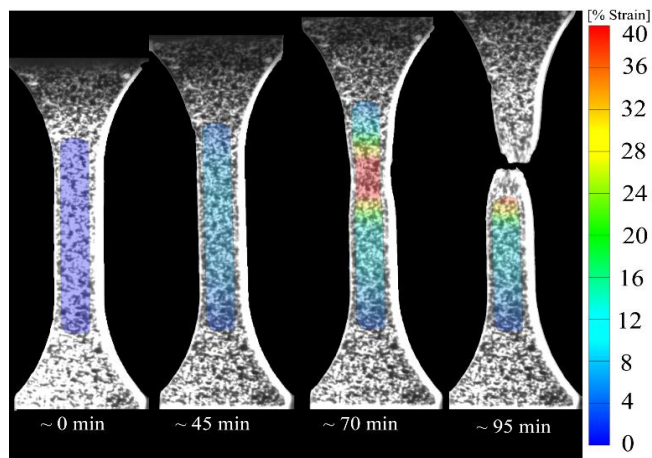


Figure 4.36: DIC maps showing the development of strain in the tensile sample from the start of the test until failure.

#### 4.5 Summary and Conclusions

This study demonstrated the *in-situ* formation of nano-scale oxides in the LPBF melt pool from precursor 14YWT GARS powders. TEM analysis and HE-XRD of the GARS precursor powders showed that Y was present in the powder in the form of  $Y_2Fe_{17}$  intermetallic. FIB cross-section and subsequent chemical map of the powder crust also revealed the presence of Y and Ti on the powder crust along with presence of Cr. During LPBF, the Cr-rich oxide layer on the surface of the powder served as a chemical reservoir, providing a controlled stoichiometry of oxygen for the reaction of Y and Ti. To understand the effect of oxygen addition to the effect on mechanical properties, trials were conducted in control environment of Argon as well as under varying oxygen

concentration (2%, 3%, 5%, 7% and 10% by wt). As Concept Laser M100R was limited with a 100W laser, process parameters such as hatch spacing, and laser beam speed were varied to achieve a wider process space with different energy densities to identify under melt, dense and over melt conditions. The parameter map produced in this study identified a stable process space that resulted in a dense microstructure (~99.8% optical relative density) that was free of large-scale microstructural defects. Most of the samples were dense which was proved by relative optical density and well as microCT analysis. The porosity on some of the sample was attributed to poor powder spread and also due to issues arising due to lack of gas re-circulation. Subsequent re-print of some of the affected samples revealed good relative density. Analyzing the volumetric energy density plot, it can be inferred that for all the cases that were examined, a stable process region was mostly obtained between 400-650mm/sec beam speed and 0.05mm hatch spacing. Analyzing the microCT data for samples with high relative optical density revealed dense samples with small and sporadic porosity. Sample S71 indicated the presence of keyhole porosity which is caused by excessive laser heat input. MicroCT analysis revealed a dense region in the steady-state region of the 10 x 10mm island hatch size while keyhole porosity was observed along the edge of the island i.e at the point where the beam turning back. Vickers microhardness data of the samples did not reveal a significant change in hardness values for samples fabricated in argon vs under varying oxygen environment. Previous analysis by Horn et al. on Cr-166 samples concluded that when the oxygen concentration in the chamber increases, all of the chrome forms chrome oxide along with yttrium and titanium oxide. It is this excess of chrome oxide which might be affecting the hardness of the part. EBSD data of S2 small sample revealed the presence of anisotropic grains observed in the build direction. This is in general agreement with what has been reported in other AM literature.

XRD analysis of the solid samples also revealed a peak shift in the solid sample exhibited of  $-0.09$ ,  $-0.22$ , and  $-0.25^\circ$ , for (110), (200), and (211), respectively, as well as the increased intensity in the (200) peak. These effects are most likely related to residual stress in the solid samples from thermal cycling during fabrication. High magnification backscatter SEM and STEM/EDS analysis of the LPBF produced solids confirmed that this reaction resulted in a homogenous distribution of nano-scale  $\text{Ti}_2\text{Y}_2\text{O}_7$  oxides 17 – 57 nm. EELS thickness maps were used in combination with the TEM results to estimate the oxide density of  $1.8 \times 10^{20} / \text{m}^3$ . Once a suitable process space was identified, dense and, large-pore free big blocks were successfully printed in argon and under 3%  $\text{O}_2$  to show feasibility of the identified process parameter. High magnification SEM image of the S98 block revealed the presence of nano oxides dispersed and a matrix with structures of slender grain boundaries, with the grains in the range of 3-5  $\mu\text{m}$  in width.

Preliminary mechanical tests were conducted on sample which was printed using the same parameter that was used to fabricate the S98 big block. Two tensile bars were EDM cut from the larger stock piece and tested until failure. The average UTS and yield strength was 474MPa and 312MPa respectively. A sample coupon was extracted from the bar and the average Vickers hardness measurement was 236.6 HV. Although this is below the 600MPa reported by Rieken, further analysis into process space and how they affect oxide size and density formation is critical to improve mechanical characteristics of the as-fabricated sample.

The oxide sizes measured from this reported study are larger than those often reported in more traditional MA ODS alloys, usually ranging from 3-25 nm. However, the benefits of circumventing the MA step warrant further investigation. In contrast to previous AM trials on MA-processed ODS particulate that resulted in agglomeration of pre-existing  $\text{Y}_2\text{O}_3$ , the GARS powder used in this study was demonstrated to resist nano-oxide agglomeration by separating dispersed

oxygen sources (metastable oxides on powder surfaces) from nano-oxide formation sites (dissolved intermetallic fragments). The mechanisms leading to the observed oxide size and density are not fully understood and further research will be required to elucidate the influence of LPBF process parameters, powder size and GARS composition on the size and distribution of oxides.

#### **4.6 Future Work**

As reported, the average UTS values of the ASC-1-81 samples is below that has been reported in literature as well as by Rieken. Also some of the samples produced under added oxygen environment had keyhole porosity along the periphery of the island hatch pattern. The oxide size reported in this study is also larger than the ones reported in literature. To mitigate this, a CFD and heat transfer model needs to be developed to study the movement/flow of melt pool under varying oxygen and process parameter conditions. This could help identify 1) how keyhole porosity is affected with increase in chamber atmosphere along with the presence of oxygen from powder surface and, 2) how yttrium oxides are formed inside the melt pool as an effect of change in Marangoni convection caused due to excessive oxygen inside the melt pool and the print chamber.

FEA simulation needs to be developed to investigate the effect of grain size and NC accumulation along the grain boundary on relative hardness of the samples. As has been reported in literature, a larger oxide reduces the overall strength of part. An FEA simulation detailing the effect of grain size and oxide size based on process parameters can help identify the optimal process window to achieve higher hardness values.

An intensive study on different powder chemistry including the effect on change in amount of elemental Yttrium, titanium as well as the amount of oxygen added during GARS (oxygen PPM on surface on powder) is necessary to fully understand the factors affecting oxide density and

distribution. This study needs to be coupled with change in build atmospheric condition to investigate the optimal oxygen required to get a oxide density in the range of  $10^{21} - 10^{22} / \text{m}^3$ .

## REFERENCES

- [1] Ribis, J., and Lozano-Perez, S., 2014, “Nano-Cluster Stability Following Neutron Irradiation in MA957 Oxide Dispersion Strengthened Material,” *Journal of Nuclear Materials*, **444**(1), pp. 314–322.
- [2] Certain, A., Kuchibhatla, S., Shutthanandan, V., Hoelzer, D. T., and Allen, T. R., 2013, “Radiation Stability of Nanoclusters in Nano-Structured Oxide Dispersion Strengthened (ODS) Steels,” *Journal of Nuclear Materials*, **434**(1), pp. 311–321.
- [3] Lescoat, M.-L., Ribis, J., Chen, Y., Marquis, E. A., Bordas, E., Trocellier, P., Serruys, Y., Gentils, A., Kaïtasov, O., de Carlan, Y., and Legris, A., 2014, “Radiation-Induced Ostwald Ripening in Oxide Dispersion Strengthened Ferritic Steels Irradiated at High Ion Dose,” *Acta Materialia*, **78**, pp. 328–340.
- [4] Zinkle, S. J., and Was, G. S., 2013, “Materials Challenges in Nuclear Energy,” *Acta Materialia*, **61**(3), pp. 735–758.
- [5] Odette, G. R., Cunningham, N. J., Stan, T., Alam, M. E., and De Carlan, Y., 2019, “Chapter 12 - Nano-Oxide Dispersion-Strengthened Steels,” *Structural Alloys for Nuclear Energy Applications*, G.R. Odette, and S.J. Zinkle, eds., Elsevier, Boston, pp. 529–583.
- [6] Odette, G. R., 2018, “On the Status and Prospects for Nanostructured Ferritic Alloys for Nuclear Fission and Fusion Application with Emphasis on the Underlying Science,” *Scripta Materialia*, **143**, pp. 142–148.
- [7] Lu, L., and Zhang, Y. F., 1999, “Influence of Process Control Agent on Interdiffusion between Al and Mg during Mechanical Alloying,” *Journal of Alloys and Compounds*, **290**(1), pp. 279–283.
- [8] Jones, A. R., 2001, “Mechanical Alloying,” *Encyclopedia of Materials: Science and Technology*, K.H.J. Buschow, R.W. Cahn, M.C. Flemings, B. Ilschner, E.J. Kramer, S. Mahajan, and P. Veyssi re, eds., Elsevier, Oxford, pp. 1–5.
- [9] Rieken, J., 2011, “Gas Atomized Precursor Alloy Powder for Oxide Dispersion Strengthened Ferritic Stainless Steel,” *Graduate Theses and Dissertations*.
- [10] Rieken, J. R., Anderson, I. E., and Kramer, M. J., 2010, “Microstructure Evolution of Gas-Atomized Iron-Base Ods Alloys,” *Int. J. Powder Metall.*, **46**(6), pp. 17–31.
- [11] Rieken, J. R., Anderson, I. E., Kramer, M. J., Odette, G. R., Stergar, E., and Haney, E., 2012, “Reactive Gas Atomization Processing for Fe-Based ODS Alloys,” *Journal of Nuclear Materials*, **428**(1), pp. 65–75.
- [12] McClintock, D. A., 2008, “Mechanical Properties of an Irradiated Nanocluster Strengthened High-Chromium Ferritic Alloy.”

- [13] McClintock, D., Hoelzer, D., Sokolov, M., and Nanstad, R., 2009, “Mechanical Properties of Neutron Irradiated Nanostructured Ferritic Alloy 14YWT,” *Journal of Nuclear Materials - J NUCL MATER*, **386**, pp. 307–311.
- [14] Hirata, A., Fujita, T., Liu, C. T., and Chen, M. W., 2012, “Characterization of Oxide Nanoprecipitates in an Oxide Dispersion Strengthened 14YWT Steel Using Aberration-Corrected STEM,” *Acta Materialia*, **60**(16), pp. 5686–5696.
- [15] Brandes, M. C., Kovarik, L., Miller, M. K., Daehn, G. S., and Mills, M. J., 2012, “Creep Behavior and Deformation Mechanisms in a Nanocluster Strengthened Ferritic Steel,” *Acta Materialia*, **60**(4), pp. 1827–1839.
- [16] Hayashi, T., Sarosi, P. M., Schneibel, J. H., and Mills, M. J., 2008, “Creep Response and Deformation Processes in Nanocluster-Strengthened Ferritic Steels,” *Acta Materialia*, **56**(7), pp. 1407–1416.
- [17] Cunningham, N. J., Wu, Y., Etienne, A., Haney, E. M., Odette, G. R., Stergar, E., Hoelzer, D. T., Kim, Y. D., Wirth, B. D., and Maloy, S. A., 2014, “Effect of Bulk Oxygen on 14YWT Nanostructured Ferritic Alloys,” *Journal of Nuclear Materials*, **444**(1), pp. 35–38.
- [18] He, J., Wan, F., Sridharan, K., Allen, T. R., Certain, A., Shutthanandan, V., and Wu, Y. Q., 2014, “Stability of Nanoclusters in 14YWT Oxide Dispersion Strengthened Steel under Heavy Ion-Irradiation by Atom Probe Tomography,” *Journal of Nuclear Materials*, **455**(1), pp. 41–45.
- [19] Parish, C. M., White, R. M., LeBeau, J. M., and Miller, M. K., 2014, “Response of Nanostructured Ferritic Alloys to High-Dose Heavy Ion Irradiation,” *Journal of Nuclear Materials*, **445**(1), pp. 251–260.
- [20] Kim, J. H., Byun, T. S., Hoelzer, D. T., Park, C. H., Yeom, J. T., and Hong, J. K., 2013, “Temperature Dependence of Strengthening Mechanisms in the Nanostructured Ferritic Alloy 14YWT: Part II—Mechanistic Models and Predictions,” *Materials Science and Engineering: A*, **559**, pp. 111–118.
- [21] Krauss, G., 1990, “Steels: Heat Treatment and Processing Principles,” undefined.
- [22] Ukai, S., Harada, M., Okada, H., Inoue, M., Nomura, S., Shikakura, S., Asabe, K., Nishida, T., and Fujiwara, M., 1993, “Alloying Design of Oxide Dispersion Strengthened Ferritic Steel for Long Life FBRs Core Materials,” *Journal of Nuclear Materials*, **204**, pp. 65–73.
- [23] Huh, M. J., Kim, S. B., Paik, K. W., and Kim, Y. G., 1997, “Effect of Mo Substitution by W on Impact Property of Heat Affected Zone in Duplex Stainless Steels,” *Scripta Materialia*, **36**(7).

- [24] Ukai, S., 2012, “4.08 - Oxide Dispersion Strengthened Steels,” *Comprehensive Nuclear Materials*, R.J.M. Konings, ed., Elsevier, Oxford, pp. 241–271.
- [25] Fournier, B., Steckmeyer, A., Rouffie, A.-L., Malaplate, J., Garnier, J., Ratti, M., Wident, P., Ziolk, L., Tournie, I., Rabeau, V., Gentzbittel, J. M., Kruml, T., and Kubena, I., 2012, “Mechanical Behaviour of Ferritic ODS Steels – Temperature Dependency and Anisotropy,” *Journal of Nuclear Materials*, **430**(1), pp. 142–149.
- [26] Zhao, Q., Yu, L., Liu, Y., Huang, Y., Ma, Z., Li, H., and Wu, J., 2017, “Microstructure and Tensile Properties of a 14Cr ODS Ferritic Steel,” *Materials Science and Engineering: A*, **680**, pp. 347–350.
- [27] Alinger, M. J., Odette, G. R., and Hoelzer, D. T., 2004, “The Development and Stability of Y–Ti–O Nanoclusters in Mechanically Alloyed Fe–Cr Based Ferritic Alloys,” *Journal of Nuclear Materials*, **329–333**, pp. 382–386.
- [28] Kumar, D., Prakash, U., Dabhade, V. V., Laha, K., and Sakthivel, T., 2018, “Influence of Yttria on Oxide Dispersion Strengthened (ODS) Ferritic Steel,” *Materials Today: Proceedings*, **5**(2, Part 1), pp. 3909–3913.
- [29] Gil, E., Ordás, N., García-Rosales, C., and Iturriza, I., 2015, “Microstructural Characterization of ODS Ferritic Steels at Different Processing Stages,” *Fusion Engineering and Design*, **98–99**, pp. 1973–1977.
- [30] London, A. J., Santra, S., Amirthapandian, S., Panigrahi, B. K., Sarguna, R. M., Balaji, S., Vijay, R., Sundar, C. S., Lozano-Perez, S., and Grovenor, C. R. M., 2015, “Effect of Ti and Cr on Dispersion, Structure and Composition of Oxide Nano-Particles in Model ODS Alloys,” *Acta Materialia*, **97**, pp. 223–233.
- [31] Dadé, M., Malaplate, J., Garnier, J., De Geuser, F., Barcelo, F., Wident, P., and Deschamps, A., 2017, “Influence of Microstructural Parameters on the Mechanical Properties of Oxide Dispersion Strengthened Fe-14Cr Steels,” *Acta Materialia*, **127**, pp. 165–177.
- [32] Wang, L., Bai, Z., Shen, H., Wang, C., and Liu, T., 2017, “Creation of Y<sub>2</sub>Ti<sub>2</sub>O<sub>7</sub> Nanoprecipitates to Strengthen the Fe-14Cr-3Al-2W Steels by Adding Ti Hydride and Y<sub>2</sub>O<sub>3</sub> Nanoparticles,” *Journal of Nuclear Materials*, **488**, pp. 319–327.
- [33] Ukai, S., and Fujiwara, M., 2002, “Perspective of ODS Alloys Application in Nuclear Environments,” *Journal of Nuclear Materials*, **307–311**, pp. 749–757.
- [34] Norgett, M. J., Robinson, M. T., and Torrens, I. M., 1975, “A Proposed Method of Calculating Displacement Dose Rates,” *Nuclear Engineering and Design*, **33**(1), pp. 50–54.

- [35] Nordlund, K., Zinkle, S. J., Sand, A. E., Granberg, F., Averbach, R. S., Stoller, R. E., Suzudo, T., Malerba, L., Banhart, F., Weber, W. J., Willaime, F., Dudarev, S. L., and Simeone, D., 2018, "Primary Radiation Damage: A Review of Current Understanding and Models," *Journal of Nuclear Materials*, **512**, pp. 450–479.
- [36] Odette, G. R., and Nanstad, R. K., 2009, "Predictive Reactor Pressure Vessel Steel Irradiation Embrittlement Models: Issues and Opportunities," *JOM*, **61**(7), pp. 17–23.
- [37] Allen, T., Busby, J., Meyer, M., and Petti, D., 2010, "Materials Challenges for Nuclear Systems," *Materials Today*, **13**(12), pp. 14–23.
- [38] Klueh, R. L., Shingledecker, J. P., Swindeman, R. W., and Hoelzer, D. T., 2005, "Oxide Dispersion-Strengthened Steels: A Comparison of Some Commercial and Experimental Alloys," *Journal of Nuclear Materials*, **341**(2), pp. 103–114.
- [39] Wharry, J. P., Swenson, M. J., and Yano, K. H., 2017, "A Review of the Irradiation Evolution of Dispersed Oxide Nanoparticles in the b.c.c. Fe-Cr System: Current Understanding and Future Directions," *Journal of Nuclear Materials*, **486**, pp. 11–20.
- [40] Garner, F. A., Toloczko, M. B., and Sencer, B. H., 2000, "Comparison of Swelling and Irradiation Creep Behavior of Fcc-Austenitic and Bcc-Ferritic/Martensitic Alloys at High Neutron Exposure," *Journal of Nuclear Materials*, **276**(1), pp. 123–142.
- [41] Serrano, M., García-Junceda, A., Hernandez, R., and Hernández-Mayoral, M., 2014, "On Anisotropy of Ferritic ODS Alloys," *Materials Science and Technology*, **30**, pp. 1664–1668.
- [42] Steckmeyer, A., Rodrigo, V. H., Gentzmittel, J. M., Rabeau, V., and Fournier, B., 2012, "Tensile Anisotropy and Creep Properties of a Fe–14CrWTi ODS Ferritic Steel," *Journal of Nuclear Materials*, **426**(1), pp. 182–188.
- [43] Kasada, R., Lee, S. G., Isselin, J., Lee, J. H., Omura, T., Kimura, A., Okuda, T., Inoue, M., Ukai, S., Ohnuki, S., Fujisawa, T., and Abe, F., 2011, "Anisotropy in Tensile and Ductile–Brittle Transition Behavior of ODS Ferritic Steels," *Journal of Nuclear Materials*, **417**(1), pp. 180–184.
- [44] Masuda, H., Tobe, H., Sato, E., Sugino, Y., and Ukai, S., 2019, "Diffusional Mass Flux Accommodating Two-Dimensional Grain Boundary Sliding in ODS Ferritic Steel," *Acta Materialia*, **176**, pp. 63–72.
- [45] Seol, J. B., Haley, D., Hoelzer, D. T., and Kim, J. H., 2018, "Influences of Interstitial and Extrusion Temperature on Grain Boundary Segregation, Y–Ti–O Nanofeatures, and Mechanical Properties of Ferritic Steels," *Acta Materialia*, **153**, pp. 71–85.

- [46] Ashby, M. F., 1970, “The Deformation of Plastically Non-Homogeneous Materials,” *The Philosophical Magazine: A Journal of Theoretical Experimental and Applied Physics*, **21**(170), pp. 399–424.
- [47] Hsiung, L. L., Fluss, M. J., and Kimura, A., 2010, “Structure of Oxide Nanoparticles in Fe–16Cr MA/ODS Ferritic Steel,” *Materials Letters*, **64**(16), pp. 1782–1785.
- [48] Leo, J. R. O., Pirfo Barroso, S., Fitzpatrick, M. E., Wang, M., and Zhou, Z., 2019, “Microstructure, Tensile and Creep Properties of an Austenitic ODS 316L Steel,” *Materials Science and Engineering: A*, **749**, pp. 158–165.
- [49] Arzt, E., 2001, “Creep of Oxide-Dispersion Strengthened Alloys,” *Encyclopedia of Materials: Science and Technology*, K.H.J. Buschow, R.W. Cahn, M.C. Flemings, B. Ilchner, E.J. Kramer, S. Mahajan, and P. Veysseyre, eds., Elsevier, Oxford, pp. 1800–1805.
- [50] Mao, X., Oh, K. H., Kang, S. H., Kim, T. K., and Jang, J., 2015, “On the Coherency of Y<sub>2</sub>Ti<sub>2</sub>O<sub>7</sub> Particles with Austenitic Matrix of Oxide Dispersion Strengthened Steel,” *Acta Materialia*, **89**, pp. 141–152.
- [51] Askeland, D. R., 1996, “Dispersion Strengthening by Phase Transformation and Heat Treatment,” *The Science and Engineering of Materials*, D.R. Askeland, ed., Springer US, Boston, MA, pp. 316–349.
- [52] Song, P., Morrall, D., Zhang, Z., Yabuuchi, K., and Kimura, A., 2018, “Radiation Response of ODS Ferritic Steels with Different Oxide Particles under Ion-Irradiation at 550 °C,” *Journal of Nuclear Materials*, **502**, pp. 76–85.
- [53] Hamilton, M. L., Gelles, D. S., Lobsinger, R. J., Paxton, M. M., and Brown, W. F., 2000, “Fabrication Technology for ODS Alloy MA957,” Other Information: PBD: 16 Mar 2000 [Online]. Available: <https://digital.library.unt.edu/ark:/67531/metadc702758/>. [Accessed: 04-May-2022].
- [54] Scattergood, R. O., and Bacon, D. J., 1975, “The Orowan Mechanism in Anisotropic Crystals,” *The Philosophical Magazine: A Journal of Theoretical Experimental and Applied Physics*, **31**(1), pp. 179–198.
- [55] Orowan, E., 1934, “Zur Kristallplastizität. III,” *Z. Physik*, **89**(9), pp. 634–659.
- [56] Hirth, J. P., 1985, “A Brief History of Dislocation Theory,” *Metall Mater Trans A*, **16**(12), pp. 2085–2090.
- [57] Bacon, D. J., Kocks, U. F., and Scattergood, R. O., 1973, “The Effect of Dislocation Self-Interaction on the Orowan Stress,” *The Philosophical Magazine: A Journal of Theoretical Experimental and Applied Physics*, **28**(6), pp. 1241–1263.

- [58] Martin, J. W., 1980, *Micromechanisms in Particle-Hardened Alloys*, Cambridge ; New York : Cambridge University Press, [1980].
- [59] Aikin, R. M., and Christodoulou, L., 1991, “The Role of Equiaxed Particles on the Yield Stress of Composites,” *Scripta Metallurgica et Materialia*, **25**(1), pp. 9–14.
- [60] Smallman, R. E., and Ngan, A. H. W., 2014, “Chapter 13 - Precipitation Hardening,” *Modern Physical Metallurgy (Eighth Edition)*, R.E. Smallman, and A.H.W. Ngan, eds., Butterworth-Heinemann, Oxford, pp. 499–527.
- [61] Benjamin, J. S., 1970, “Dispersion Strengthened Superalloys by Mechanical Alloying,” *Metall Mater Trans B*, **1**(10), pp. 2943–2951.
- [62] McPherson, M., 2019, “Development of Ni-Based Oxide Dispersion Strengthened (ODS) Powder Particles for Metal Additive Manufacturing (AM) Applications,” Graduate Theses, Dissertations, and Problem Reports.
- [63] Baheti, V., Abbasi, A. M. R., and Militky, J., 2012, “Nourn,” *World Journal of Engineering*, **9**, pp. 45–50.
- [64] Maurice, D., and Courtney, T. H., 1994, “Modeling of Mechanical Alloying: Part I. Deformation, Coalescence, and Fragmentation Mechanisms,” *Metall Mater Trans A*, **25**(1), pp. 147–158.
- [65] Kwon, N.-H., Kim, G.-H., Song, H. S., and Lee, H.-L., 2001, “Synthesis and Properties of Cubic Zirconia–Alumina Composite by Mechanical Alloying,” *Materials Science and Engineering: A*, **299**(1), pp. 185–194.
- [66] Zhang, K. B., Fu, Z. Y., Zhang, J. Y., Wang, W. M., Lee, S. W., and Niihara, K., 2010, “Characterization of Nanocrystalline CoCrFeNiTiAl High-Entropy Solid Solution Processed by Mechanical Alloying,” *Journal of Alloys and Compounds*, **495**(1), pp. 33–38.
- [67] Nouri, A., Hodgson, P., and Wen, C., 2011, “Effect of Ball-Milling Time on the Structural Characteristics of Biomedical Porous Ti-Sn-Nb Alloy,” *Materials Science and Engineering C*, **31**, pp. 921–928.
- [68] Korb, G., Rühle, M., and Martinz, H.-P., 2015, “New Iron-Based ODS-Superalloys for High Demanding Applications,” *American Society of Mechanical Engineers Digital Collection*.
- [69] Wu, Q., Li, M., Guo, Y., Shan, J., Wang, H., and Chang, Y., 2020, “Microstructural Evolution and Mechanical Properties of Friction Stir Welded 12Cr-ODS Steel,” *Nuclear Materials and Energy*, **25**, p. 100804.

- [70] Karak, S. K., Dutta Majumdar, J., Witczak, Z., Lojkowski, W., and Manna, I., 2013, "Microstructure and Mechanical Properties of Nano-Y<sub>2</sub>O<sub>3</sub> Dispersed Ferritic Alloys Synthesized by Mechanical Alloying and Consolidated by Hydrostatic Extrusion," *Materials Science and Engineering: A*, **580**, pp. 231–241.
- [71] Rajan, K., Sarma, V. S., Kutty, T. R. G., and Murty, B. S., 2012, "Hot Hardness Behaviour of Ultrafine Grained Ferritic Oxide Dispersion Strengthened Alloys Prepared by Mechanical Alloying and Spark Plasma Sintering," *Materials Science and Engineering: A*, **558**, pp. 492–496.
- [72] Auger, M. A., Huang, Y., Zhang, H., Jones, C. A., Hong, Z., Moody, M. P., Roberts, S. G., and Grant, P. S., 2018, "Microstructural and Mechanical Characterisation of Fe-14Cr-0.22Hf Alloy Fabricated by Spark Plasma Sintering," *Journal of Alloys and Compounds*, **762**, pp. 678–687.
- [73] Laurent-Brocq, M., Legendre, F., Mathon, M.-H., Mascaro, A., Poissonnet, S., Radiguet, B., Pareige, P., Loyer, M., and Leseigneur, O., 2012, "Influence of Ball-Milling and Annealing Conditions on Nanocluster Characteristics in Oxide Dispersion Strengthened Steels," *Acta Materialia*, **60**(20), pp. 7150–7159.
- [74] Ukai, S., and Ohtsuka, S., 2007, "Nano-Mesosopic Structure Control in 9Cr–ODS Ferritic Steels," *Energy Materials*, **2**(1), pp. 26–35.
- [75] Alinger, M. J., Odette, G. R., and Hoelzer, D. T., 2009, "On the Role of Alloy Composition and Processing Parameters in Nanocluster Formation and Dispersion Strengthening in Nanostuctured Ferritic Alloys," *Acta Materialia*, **57**(2), pp. 392–406.
- [76] Karak, S. K., Majumdar, J. D., Lojkowski, W., Michalski, A., Ciupinski, L., Kurzydłowski, K. J., and Manna, I., 2012, "Microstructure and Mechanical Properties of Nano-Y<sub>2</sub>O<sub>3</sub> Dispersed Ferritic Steel Synthesized by Mechanical Alloying and Consolidated by Pulse Plasma Sintering," *Philosophical Magazine*, **92**(5), pp. 516–534.
- [77] Ponraj, B. V., Dinesh Kumar, A., and Kumaran, S., 2020, "Rapid Synthesis of Oxide Dispersion Strengthened Ferritic Alloys through Spark Plasma Sintering," *Materials Today: Proceedings*, **27**, pp. 2661–2666.
- [78] Dawson, H., Serrano, M., Hernandez, R., Cater, S., and Jimenez-Melero, E., 2017, "Mechanical Properties and Fracture Behaviour of ODS Steel Friction Stir Welds at Variable Temperatures," *Materials Science and Engineering: A*, **693**, pp. 84–92.
- [79] Dietrich, S., Wunderer, M., Huissel, A., and Zaeh, M. F., 2016, "A New Approach for a Flexible Powder Production for Additive Manufacturing," *Procedia Manufacturing*, **6**, pp. 88–95.
- [80] Herzog, D., Seyda, V., Wycisk, E., and Emmelmann, C., 2016, "Additive Manufacturing of Metals," *Acta Materialia*, **117**, pp. 371–392.

- [81] Popovich, A., and Sufiiarov, V., 2016, *Metal Powder Additive Manufacturing*, IntechOpen.
- [82] Heidloff, A., Rieken, J., Anderson, I., Byrd, D., Sears, J., Glynn, M., and Ward, R., 2010, “Advanced Gas Atomization Processing for Ti and Ti Alloy Powder Manufacturing,” *JOM: the journal of the Minerals, Metals & Materials Society*, **62**, pp. 35–41.
- [83] Jahns, K., Bappert, R., Böhlke, P., and Krupp, U., 2020, “Additive Manufacturing of CuCr1Zr by Development of a Gas Atomization and Laser Powder Bed Fusion Routine,” *Int J Adv Manuf Technol*, **107**(5), pp. 2151–2161.
- [84] Lawley, A., 1978, “Preparation of Metal Powders,” *Annual Review of Materials Science*, **8**(1), pp. 49–71.
- [85] Ejim, C. E., Rahman, M. A., Amirfazli, A., and Fleck, B. A., 2010, “Effects of Liquid Viscosity and Surface Tension on Atomization in Two-Phase, Gas/Liquid Fluid Coker Nozzles,” *Fuel*, **89**(8), pp. 1872–1882.
- [86] Eisen, W. B., Ferguson, B. L., German, R. M., Iacocca, R., Lee, P. W., Madan, D., Moyer, K., Sanderow, H., and Trudel, Y., 1998, “Powder Metal Technologies and Applications.”
- [87] Upadhyaya, A., and German, R. M., 1998, “Shape Distortion in Liquid-Phase-Sintered Tungsten Heavy Alloys,” *Metallurgical and Materials Transactions. A, Physical Metallurgy and Materials Science*, **29**(10).
- [88] Lemoisson, F., and Froyen, L., 2005, “12 - Understanding and Improving Powder Metallurgical Processes,” *Fundamentals of Metallurgy*, S. Seetharaman, ed., Woodhead Publishing, pp. 471–502.
- [89] Lawley, A., 1992, *Atomization: The Production of Metal Powders*, Metal Powder Industries Federation.
- [90] Machio, C., Machaka, R., Motsai, T., Chikosha, S., and Rossouw, P., 2018, “Production of Spherical Titanium Based Powders from Powder Metallurgy Bars.”
- [91] Guillen, D. P., Wharry, J. P., and Gandy, D. W., 2017, “Neutron Irradiation of Nuclear Structural Materials Fabricated by Powder Metallurgy with Hot Isostatic Pressing,” *Transactions of the American Nuclear Society*, **116**.
- [92] Perez-de Leon, G., Lamberti, V., Seals, R. D., Abu-Lebdeh, T., and Hamoush, S., 2016, “Gas Atomization of Molten Metal: PartI. Numerical Modeling Conception,” **9**, pp. 303–322.
- [93] Lubanska, H., 1970, “Correlation of Spray Ring Data for Gas Atomization of Liquid Metals,” *JOM*, **22**(2), pp. 45–49.

- [94] Ting, J., and Anderson, I. E., 2004, “A Computational Fluid Dynamics (CFD) Investigation of the Wake Closure Phenomenon,” *Materials Science and Engineering: A*, **379**(1), pp. 264–276.
- [95] Abu-Lebdeh, T., Leon, G., Hamoush, S., Seals, R. D., and Lamberti, V., 2016, “Gas Atomization of Molten Metal: Part II. Applications.”
- [96] Anderson, I., Rieken, J., Meyer, J., Byrd, D., and Heidloff, A., 2011, “Visualization of Atomization Gas Flow and Melt Break-up Effects in Response to Nozzle Design,” *PowderMet 2011*, San Francisco, CA, May 18-21, 2011 [Online]. Available: <https://digital.library.unt.edu/ark:/67531/metadc829723/>. [Accessed: 05-May-2022].
- [97] Park, S., 2020, “Optimization Studies for the Gas Atomization and Selective Laser Melting Processes of Al10SiMg Alloy,” *Electronic Theses and Dissertations*, 2020-.
- [98] Park, J. J., Hong, S. M., Park, E. K., Lee, M. K., and Rhee, C. K., 2012, “Synthesis of Fe Based ODS Alloys by a Very High Speed Planetary Milling Process,” *Journal of Nuclear Materials*, **428**(1), pp. 35–39.
- [99] Horn, T., Rock, C., Kaoumi, D., Anderson, I., White, E., Prost, T., Rieken, J., Saptarshi, S., Schoell, R., DeJong, M., Timmins, S., Napolitano, R., Zhang, D., and Darsell, J., 2022, *Laser Powder Bed Fusion Additive Manufacturing of Oxide Dispersion Strengthened Steel Using Gas Atomized Reaction Synthesis Powder*, ID 3985835, Social Science Research Network, Rochester, NY.
- [100] Pazos, D., Cintins, A., de Castro, V., Fernández, P., Hoffmann, J., Vargas, W. G., Leguey, T., Purans, J., Anspoks, A., Kuzmin, A., Iturriza, I., and Ordás, N., 2018, “ODS Ferritic Steels Obtained from Gas Atomized Powders through the STARS Processing Route: Reactive Synthesis as an Alternative to Mechanical Alloying,” *Nuclear Materials and Energy*, **17**, pp. 1–8.
- [101] Gil, E., Ordás, N., García-Rosales, C., and Iturriza, I., 2016, “ODS Ferritic Steels Produced by an Alternative Route (STARS): Microstructural Characterisation after Atomisation, HIPping and Heat Treatments,” *Powder Metallurgy*, **59**(5), pp. 359–369.
- [102] Ordás, N., Gil, E., Cintins, A., de Castro, V., Leguey, T., Iturriza, I., Purans, J., Anspoks, A., Kuzmin, A., and Kalinko, A., 2018, “The Role of Yttrium and Titanium during the Development of ODS Ferritic Steels Obtained through the STARS Route: TEM and XAS Study,” *Journal of Nuclear Materials*, **504**, pp. 8–22.
- [103] Wilson, F. G., Knott, B. R., and Desforges, C. D., 1978, “Preparation and Properties of Some ODS Fe-Cr-Al Alloys,” *Metall Mater Trans A*, **9**(2), pp. 275–282.
- [104] Oksiuta, Z., Ozieblo, A., Perkowski, K., Osuchowski, M., and Lewandowska, M., 2014, “Influence of HIP Pressure on Tensile Properties of a 14Cr ODS Ferritic Steel,” *Fusion Engineering and Design*, **89**(2), pp. 137–141.

- [105] Svoboda, J., Kunčická, L., Luptáková, N., Weiser, A., and Dymáček, P., 2020, “Fundamental Improvement of Creep Resistance of New-Generation Nano-Oxide Strengthened Alloys via Hot Rotary Swaging Consolidation,” *Materials (Basel)*, **13**(22), p. E5217.
- [106] Klueh, R., Gelles, D., Jitsukawa, S., Kimura, A., Odette, G. R., Schaaf, B., and Victoria, M., 2002, “Ferritic/Martensitic Steels - Overview of Recent Results,” *Journal of Nuclear Materials*, **307–311**, pp. 455–465.
- [107] Schneibel, J. H., Liu, C. T., Miller, M. K., Mills, M. J., Sarosi, P., Heilmaier, M., and Sturm, D., 2009, “Ultrafine-Grained Nanocluster-Strengthened Alloys with Unusually High Creep Strength,” *Scripta Materialia*, **61**(8), pp. 793–796.
- [108] Noh, S., Choi, B.-K., Kang, S. H., and Kim, T., 2014, “Influence of Mechanical Alloying Atmospheres on the Microstructures and Mechanical Properties of 15Cr Ods Steels,” *Nuclear Engineering and Technology*, **46**, pp. 857–862.
- [109] Mishra, R. S., and Ma, Z. Y., 2005, “Friction Stir Welding and Processing,” *Materials Science and Engineering: R: Reports*, **50**(1), pp. 1–78.
- [110] Wang, J., Yuan, W., Mishra, R. S., and Charit, I., 2013, “Microstructure and Mechanical Properties of Friction Stir Welded Oxide Dispersion Strengthened Alloy,” *Journal of Nuclear Materials*, **432**(1), pp. 274–280.
- [111] Cabibbo, M., Forcellese, A., Santecchia, E., Paoletti, C., Spigarelli, S., and Simoncini, M., 2020, “New Approaches to Friction Stir Welding of Aluminum Light-Alloys,” *Metals*, **10**(2), p. 233.
- [112] Anselmi-Tamburini, U., 2021, “Spark Plasma Sintering,” *Encyclopedia of Materials: Technical Ceramics and Glasses*, M. Pomeroy, ed., Elsevier, Oxford, pp. 294–310.
- [113] Zhang, Z.-H., Liu, Z.-F., Lu, J.-F., Shen, X.-B., Wang, F.-C., and Wang, Y.-D., 2014, “The Sintering Mechanism in Spark Plasma Sintering – Proof of the Occurrence of Spark Discharge,” *Scripta Materialia*, **81**, pp. 56–59.
- [114] Cavaliere, P., Sadeghi, B., Shamanian, M., and Ashrafizadeh, F., 2019, “Al-Based Nanocomposites Produced via Spark Plasma Sintering: Effect of Processing Route and Reinforcing Phases,” *Spark Plasma Sintering of Materials: Advances in Processing and Applications*, P. Cavaliere, ed., Springer International Publishing, Cham, pp. 161–190.
- [115] Franke, P., Heintze, C., Bergner, F., and Weißgärber, T., 2010, “Mechanical Properties of Spark Plasma Sintered Fe-Cr Compacts Strengthened by Nanodispersed Ytria Particles,” *Materials Testing*, **52**(3), pp. 133–138.

- [116] Joshi, V. V., Whalen, S. A., Lavender, C. A., Grant, G. J., Reza-E-Rabby, M. D., Rohatgi, A., and Darsell, J. T., 2021, “United States Patent: 11045851 - Method for Forming Hollow Profile Non-Circular Extrusions Using Shear Assisted Processing and Extrusion (ShAPE).”
- [117] Li, X., Tang, W., and Reynolds, A. P., 2012, “Visualization of Material Flow in Friction Extrusion,” *ICAA13: 13th International Conference on Aluminum Alloys*, John Wiley & Sons, Ltd, pp. 1659–1664.
- [118] Catalini, D., Kaoumi, D., Reynolds, A. P., and Grant, G., 2012, “Friction Consolidation of an Oxide Dispersion Strengthened Steel,” *Transactions of the American Nuclear Society*, **107**, pp. 458–461.
- [119] Overman, N. R., Whalen, S. A., Bowden, M. E., Olszta, M. J., Kruska, K., Clark, T., Stevens, E. L., Darsell, J. T., Joshi, V. V., Jiang, X., Mattlin, K. F., and Mathaudhu, S. N., 2017, “Homogenization and Texture Development in Rapidly Solidified AZ91E Consolidated by Shear Assisted Processing and Extrusion (ShAPE),” *Materials Science and Engineering: A*, **701**, pp. 56–68.
- [120] Croteau, J. R., Jung, J.-G., Whalen, S. A., Darsell, J., Mello, A., Holstine, D., Lay, K., Hansen, M., Dunand, D. C., and Vo, N. Q., 2020, “Ultrafine-Grained Al-Mg-Zr Alloy Processed by Shear-Assisted Extrusion with High Thermal Stability,” *Scripta Materialia*, **186**, pp. 326–330.
- [121] Li, X., Zhou, C., Overman, N., Ma, X., Canfield, N., Kappagantula, K., Schroth, J., and Grant, G., 2021, “Copper Carbon Composite Wire with a Uniform Carbon Dispersion Made by Friction Extrusion,” *Journal of Manufacturing Processes*, **65**, pp. 397–406.
- [122] Komarasamy, M., Li, X., Whalen, S. A., Ma, X., Canfield, N., Olszta, M. J., Varga, T., Schemer-Kohn, A. L., Yu, A., Overman, N. R., Mathaudhu, S. N., and Grant, G. J., 2021, “Microstructural Evolution in Cu–Nb Processed via Friction Consolidation,” *J Mater Sci*, **56**(22), pp. 12864–12880.
- [123] Li, X., Grant, G., Zhou, C., Wang, H., Perry, T., and Schroth, J., 2019, “Copper-Graphite Composite Wire Made by Shear-Assisted Processing and Extrusion,” *Friction Stir Welding and Processing X*, Y. Hovanski, R. Mishra, Y. Sato, P. Upadhyay, and D. Yan, eds., Springer International Publishing, Cham, pp. 163–169.
- [124] Li, X., Zhou, C., Overman, N., Ma, X., Canfield, N., Kappagantula, K., Schroth, J., and Grant, G., 2021, “Copper Carbon Composite Wire with a Uniform Carbon Dispersion Made by Friction Extrusion,” *Journal of Manufacturing Processes*, **65**, pp. 397–406.
- [125] Bajaj, P., Hariharan, A., Kini, A., Kürnsteiner, P., Raabe, D., and Jäggle, E. A., 2020, “Steels in Additive Manufacturing: A Review of Their Microstructure and Properties,” *Materials Science and Engineering: A*, **772**, p. 138633.

- [126] Walker, J. C., Berggreen, K. M., Jones, A. R., and Sutcliffe, C. J., 2009, "Fabrication of Fe–Cr–Al Oxide Dispersion Strengthened PM2000 Alloy Using Selective Laser Melting," *Advanced Engineering Materials*, **11**(7), pp. 541–546.
- [127] Kelly, T. J., 1979, "Pulsed YAG Laser Welding of ODS Alloys," *AIP Conference Proceedings*, **50**(1), pp. 215–220.
- [128] Zhong, W., Sridharan, N., Isheim, D., Field, K. G., Yang, Y., Terrani, K., and Tan, L., 2021, "Microstructures and Mechanical Properties of a Modified 9Cr Ferritic-Martensitic Steel in the as-Built Condition after Additive Manufacturing," *Journal of Nuclear Materials*, **545**, p. 152742.
- [129] Wilms, M. B., Streubel, R., Frömel, F., Weisheit, A., Tenkamp, J., Walther, F., Barcikowski, S., Schleifenbaum, J. H., and Gökce, B., 2018, "Laser Additive Manufacturing of Oxide Dispersion Strengthened Steels Using Laser-Generated Nanoparticle-Metal Composite Powders," *Procedia CIRP*, **74**, pp. 196–200.
- [130] Song, Q., Zhang, Y., Wei, Y., Zhou, X., Shen, Y., Zhou, Y., and Feng, X., 2021, "Microstructure and Mechanical Performance of ODS Superalloys Manufactured by Selective Laser Melting," *Optics & Laser Technology*, **144**, p. 107423.
- [131] Mirzababaei, S., Ghayoor, M., Doyle, R. P., and Pasebani, S., 2021, "In-Situ Manufacturing of ODS FeCrAlY Alloy via Laser Powder Bed Fusion," *Materials Letters*, **284**, p. 129046.
- [132] Boegelein, T., Louvis, E., Dawson, K., Tatlock, G. J., and Jones, A. R., 2016, "Characterisation of a Complex Thin Walled Structure Fabricated by Selective Laser Melting Using a Ferritic Oxide Dispersion Strengthened Steel," *Materials Characterization*, **112**, pp. 30–40.
- [133] Shi, Y., Lu, Z., and Xie, R., 2020, "Microstructure Characterization and Micro-Hardness of Fe-9Cr ODS Alloy Produced by Laser Powder Bed Fusion," *IOP Conf. Ser.: Mater. Sci. Eng.*, **772**(1), p. 012110.
- [134] Kenel, C., Dawson, K., Barras, J., Hauser, C., Dasargyri, G., Bauer, T., Colella, A., Spierings, A. B., Tatlock, G. J., Leinenbach, C., and Wegener, K., 2017, "Microstructure and Oxide Particle Stability in a Novel ODS  $\gamma$ -TiAl Alloy Processed by Spark Plasma Sintering and Laser Additive Manufacturing," *Intermetallics*, **90**, pp. 63–73.
- [135] Doñate-Buendia, C., Kürnsteiner, P., Stern, F., Wilms, M. B., Streubel, R., Kusoglu, I. M., Tenkamp, J., Bruder, E., Pirch, N., Barcikowski, S., Durst, K., Schleifenbaum, J. H., Walther, F., Gault, B., and Gökce, B., 2021, "Microstructure Formation and Mechanical Properties of ODS Steels Built by Laser Additive Manufacturing of Nanoparticle Coated Iron-Chromium Powders," *Acta Materialia*, **206**, p. 116566.

- [136] Boegelein, T., Dryepondt, S. N., Pandey, A., Dawson, K., and Tatlock, G. J., 2015, “Mechanical Response and Deformation Mechanisms of Ferritic Oxide Dispersion Strengthened Steel Structures Produced by Selective Laser Melting,” *Acta Materialia*, **87**, pp. 201–215.
- [137] Liu, Y., Fang, J., Liu, D., Lu, Z., Liu, F., Chen, S., and Liu, C. T., 2010, “Formation of Oxides Particles in Ferritic Steel by Using Gas-Atomized Powder,” *Journal of Nuclear Materials*, **396**, pp. 86–93.
- [138] Hunt, R., Kramer, K., and El-Dasher, B., 2015, “Selective Laser Sintering of MA956 Oxide Dispersion Strengthened Steel,” *Journal of Nuclear Materials*, **464**.
- [139] Rock, C., Vadlakonda, R., Figurskey, S., Ledford, C., West, H., Miller, V., Pankow, M., Daniels, K. E., and Horn, T., 2020, “Analysis of Self-Organized Patterned Surface Oxide Spots on Ejected Spatter Produced during Laser Powder Bed Fusion,” *Additive Manufacturing*, **35**, p. 101320.
- [140] Simonelli, M., Tuck, C., Aboulkhair, N. T., Maskery, I., Ashcroft, I., Wildman, R. D., and Hague, R., 2015, “A Study on the Laser Spatter and the Oxidation Reactions During Selective Laser Melting of 316L Stainless Steel, Al-Si10-Mg, and Ti-6Al-4V,” *Metall Mater Trans A*, **46**(9), pp. 3842–3851.
- [141] Doñate-Buendía, C., Frömel, F., Wilms, M. B., and al, et, 2018, “Oxide Dispersion-Strengthened Alloys Generated by Laser Metal Deposition of Laser-Generated Nanoparticle-Metal Powder Composites,” *Materials and design*, **154**, pp. 360–369.
- [142] Gao, R., Zeng, L., Ding, H., Zhang, T., Wang, X., and Fang, Q., 2016, “Characterization of Oxide Dispersion Strengthened Ferritic Steel Fabricated by Electron Beam Selective Melting,” *Materials & Design*, **89**, pp. 1171–1180.
- [143] Vasquez, E., Giroux, P.-F., Lomello, F., Chniouel, A., Maskrot, H., Schuster, F., and Castany, P., 2019, “Elaboration of Oxide Dispersion Strengthened Fe-14Cr Stainless Steel by Selective Laser Melting,” *Journal of Materials Processing Technology*, **267**, pp. 403–413.
- [144] Vasquez, E., Giroux, P.-F., Lomello, F., Nussbaum, M., Maskrot, H., Schuster, F., and Castany, P., 2020, “Effect of Powder Characteristics on Production of Oxide Dispersion Strengthened Fe14Cr Steel by Laser Powder Bed Fusion,” *Powder Technology*, **360**, pp. 998–1005.
- [145] Zhong, Y., Liu, L., Zou, J., Li, X., Cui, D., and Shen, Z., 2020, “Oxide Dispersion Strengthened Stainless Steel 316L with Superior Strength and Ductility by Selective Laser Melting,” *Journal of Materials Science & Technology*, **42**, pp. 97–105.

- [146] Ghayoor, M., Lee, K., He, Y., Chang, C., Paul, B. K., and Pasebani, S., 2020, "Selective Laser Melting of Austenitic Oxide Dispersion Strengthened Steel: Processing, Microstructural Evolution and Strengthening Mechanisms," *Materials Science and Engineering: A*, **788**, p. 139532.
- [147] Ghayoor, M., Mirzababaei, S., Sittiho, A., Charit, I., Paul, B. K., and Pasebani, S., 2021, "Thermal Stability of Additively Manufactured Austenitic 304L ODS Alloy," *Journal of Materials Science & Technology*, **83**, pp. 208–218.
- [148] Ghayoor, M., Lee, K., He, Y., Chang, C., Paul, B. K., and Pasebani, S., 2019, "Microstructural Analysis of Additively Manufactured 304L Stainless Steel Oxide Dispersion Strengthened Alloy," *Microscopy and Microanalysis*, **25**(S2), pp. 2594–2595.
- [149] Chang, H. J., Cho, H. Y., and Kim, J. H., 2015, "Stability of Y–Ti–O Nanoparticles during Laser Melting of Advanced Oxide Dispersion-Strengthened Steel Powder," *Journal of Alloys and Compounds*, **653**, pp. 528–533.
- [150] Zhang, X., Cao, H., Yang, X., Zhao, Y., Wang, H., Mao, X., and Zhai, Y., 2021, "Enhanced Thermal Stability of the Cellular Structure through Nano-Scale Oxide Precipitation in 3D Printed 316L Stainless Steel," *Fusion Engineering and Design*, **164**, p. 112213.
- [151] Morrow, B., Lienert, T., Knapp, C., Sutton, J., Brand, M., Pacheco, R., Livescu, V., Carpenter, J., and Gray, G., 2018, "Impact of Defects in Powder Feedstock Materials on Microstructure of 304L and 316L Stainless Steel Produced by Additive Manufacturing," *Metallurgical and Materials Transactions A*, **49**.
- [152] Saeidi, K., Kvetková, L., Lofaj, F., and Shen, Z., 2015, "Austenitic Stainless Steel Strengthened by the in Situ Formation of Oxide Nano-inclusions," *RSC Adv.*, **5**(27), pp. 20747–20750.
- [153] Eo, D.-R., Park, S.-H., and Cho, J.-W., 2018, "Inclusion Evolution in Additive Manufactured 316L Stainless Steel by Laser Metal Deposition Process," *Materials & Design*, **155**, pp. 212–219.
- [154] Song, M., Lin, X., Liu, F., Yang, H., and Huang, W., 2016, "Effect of Environmental Oxygen Content on the Oxide Inclusion in Laser Solid Formed AISI 420 Stainless Steel," *Materials & Design*, **90**, pp. 459–467.
- [155] Paul, B. K., Lee, K., He, Y., Ghayoor, M., Chang, C., and Pasebani, S., 2020, "Oxide Dispersion Strengthened 304 L Stainless Steel Produced by Ink Jetting and Laser Powder Bed Fusion," *CIRP Annals*, **69**(1), pp. 193–196.

- [156] Doñate-Buendia, C., Streubel, R., Kürsteiner, P., Wilms, M. B., Stern, F., Tenkamp, J., Bruder, E., Barcikowski, S., Gault, B., Durst, K., Schleifenbaum, J. H., Walther, F., and Gökce, B., 2020, "Effect of Nanoparticle Additivation on the Microstructure and Microhardness of Oxide Dispersion Strengthened Steels Produced by Laser Powder Bed Fusion and Directed Energy Deposition," *Procedia CIRP*, **94**, pp. 41–45.
- [157] Shi, Y., Lu, Z., Xu, H., Xie, R., Ren, Y., and Yang, G., 2019, "Microstructure Characterization and Mechanical Properties of Laser Additive Manufactured Oxide Dispersion Strengthened Fe-9Cr Alloy," *Journal of Alloys and Compounds*, **791**, pp. 121–133.
- [158] Shi, Y., Lu, Z., Yu, L., Xie, R., Ren, Y., and Yang, G., 2020, "Microstructure and Tensile Properties of Zr-Containing ODS-FeCrAl Alloy Fabricated by Laser Additive Manufacturing," *Materials Science and Engineering: A*, **774**, p. 138937.
- [159] Malis, T., Cheng, S. C., and Egerton, R. F., 1988, "EELS Log-Ratio Technique for Specimen-Thickness Measurement in the TEM," *J Electron Microsc Tech*, **8**(2), pp. 193–200.
- [160] Kimura, A., Kasada, R., Iwata, N., Kishimoto, H., Zhang, C. H., Isselin, J., Dou, P., Lee, J. H., Muthukumar, N., Okuda, T., Inoue, M., Ukai, S., Ohnuki, S., Fujisawa, T., and Abe, T. F., 2011, "Development of Al Added High-Cr ODS Steels for Fuel Cladding of next Generation Nuclear Systems," *Journal of Nuclear Materials*, **417**(1), pp. 176–179.
- [161] Williams, C. A., Smith, G. D. W., and Marquis, E. A., 2012, "The Effect of Ti on the Coarsening Behavior of Oxygen-Rich Nanoparticles in Oxide-Dispersion-Strengthened Steels after Annealing at 1200°C," *Scripta Materialia*, **67**(1), pp. 108–111.
- [162] Reed, T. B., 1961, "Induction-Coupled Plasma Torch," *Journal of Applied Physics*, **32**(5), pp. 821–824.
- [163] Houk, R. S., and Thompson, J. J., 1988, "Inductively Coupled Plasma Mass Spectrometry," *Mass Spectrometry Reviews*, **7**(4), pp. 425–461.
- [164] Wilbur, S., 2009, "Factors Determining Sensitivity in ICP-MS," *Spectroscopy Supplements*, **0**(0).
- [165] Abou-Shakra, F. R., 2003, "Chapter 12 - Biomedical Applications of Inductively Coupled Plasma Mass Spectrometry (ICP-MS) as an Element Specific Detector for Chromatographic Separations," *Handbook of Analytical Separations*, I.D. Wilson, ed., Elsevier Science B.V., pp. 351–371.
- [166] Coburn, J. W., and Chen, M., 1980, "Optical Emission Spectroscopy of Reactive Plasmas: A Method for Correlating Emission Intensities to Reactive Particle Density," *Journal of Applied Physics*, **51**(6), pp. 3134–3136.

- [167] Lough, C. S., Escano, L. I., Qu, M., Smith, C. C., Landers, R. G., Bristow, D. A., Chen, L., and Kinzel, E. C., 2020, “In-Situ Optical Emission Spectroscopy of Selective Laser Melting,” *Journal of Manufacturing Processes*, **53**, pp. 336–341.
- [168] Lednev, V. N., Sdvizhenskii, P. A., Asyutin, R. D., Tretyakov, R. S., Grishin, M. Y., Stavertiy, A. Y., Fedorov, A. N., and Pershin, S. M., 2019, “In Situ Elemental Analysis and Failures Detection during Additive Manufacturing Process Utilizing Laser Induced Breakdown Spectroscopy,” *Opt. Express, OE*, **27**(4), pp. 4612–4628.
- [169] Everton, S. K., Hirsch, M., Stravroulakis, P., Leach, R. K., and Clare, A. T., 2016, “Review of In-Situ Process Monitoring and in-Situ Metrology for Metal Additive Manufacturing,” *Materials & Design*, **95**, pp. 431–445.
- [170] Younkin, T. R., Biewer, T. M., Klepper, C. C., and Marcus, C., 2014, “Description of the Prototype Diagnostic Residual Gas Analyzer for ITER,” *Review of Scientific Instruments*, **85**(11), p. 11E816.
- [171] Redhead, P. A., 1992, “Measurement of Residual Currents in Ionization Gauges and Residual Gas Analyzers,” *Journal of Vacuum Science & Technology A*, **10**(4), pp. 2665–2673.
- [172] Frigola, P., Agustsson, R. B., Faillace, L., Murokh, A. Y., Ciovati, G., Clemens, W. A., Dhakal, P., Marhauser, F., Rimmer, R. A., Spradlin, J. K., Williams, R. S., Mireles, J., Morton, P. A., and Wicker, R. B., 2015, *Advance Additive Manufacturing Method for SRF Cavities of Various Geometries*, JLAB-ACC-15-2216; DOE/OR/23177-5015, Thomas Jefferson National Accelerator Facility (TJNAF), Newport News, VA (United States).
- [173] Ledford, C., Rock, C., Carriere, P., Frigola, P., Gamzina, D., and Horn, T., 2019, “Characteristics and Processing of Hydrogen-Treated Copper Powders for EB-PBF Additive Manufacturing,” *Applied Sciences*, **9**(19), p. 3993.
- [174] Terrazas, C. A., Mireles, J., Gaytan, S. M., Morton, P. A., Hinojos, A., Frigola, P., and Wicker, R. B., 2016, “Fabrication and Characterization of High-Purity Niobium Using Electron Beam Melting Additive Manufacturing Technology,” *Int J Adv Manuf Technol*, **84**(5), pp. 1115–1126.
- [175] Nyman, L., Kestilä, A., Porri, P., Pudas, M., Salmi, M., Silander, R., Miikkulainen, V., Kaipio, M., Kallio, E., and Ritala, M., 2021, “Constructing Spacecraft Components Using Additive Manufacturing and Atomic Layer Deposition: First Steps for Integrated Electric Circuitry,” *Journal of Aerospace Engineering*, **34**(5), p. 04021049.
- [176] Whittig, L. D., and Allardice, W. R., 1986, “X-Ray Diffraction Techniques,” *Methods of Soil Analysis*, John Wiley & Sons, Ltd, pp. 331–362.

- [177] Gonon, M., 2021, “Case Studies in the X-Ray Diffraction of Ceramics,” *Encyclopedia of Materials: Technical Ceramics and Glasses*, M. Pomeroy, ed., Elsevier, Oxford, pp. 560–577.
- [178] Neufeind, J., and Poulsen, H. F., 1995, “Diffraction on Disordered Materials Using ‘Neutron-like’ Photons,” *Phys. Scr.*, **T57**, pp. 112–116.
- [179] Ren, Y., 2012, “High-Energy Synchrotron X-Ray Diffraction and Its Application to In Situ Structural Phase-Transition Studies in Complex Sample Environments,” *JOM*, **64**(1), pp. 140–149.
- [180] Wong, H., Dawson, K., Ravi, G., Howlett, L., Jones, R., and Sutcliffe, C., 2019, “Multi-Laser Powder Bed Fusion Benchmarking—Initial Trials with Inconel 625,” *The International Journal of Advanced Manufacturing Technology*, **105**.
- [181] Jadhav, S. D., Goossens, L. R., Kinds, Y., Hooreweder, B. V., and Vanmeensel, K., 2021, “Laser-Based Powder Bed Fusion Additive Manufacturing of Pure Copper,” *Additive Manufacturing*, **42**, p. 101990.
- [182] He, L., Zhao, H., and Niu, W., 2018, “Understanding the Effect of Oxygen on Weld Pool and Keyhole in Laser Beam Welding,” *Journal of Laser Applications*, **30**(1), p. 012003.
- [183] Leung, C. L. A., Marussi, S., Towrie, M., Atwood, R. C., Withers, P. J., and Lee, P. D., 2019, “The Effect of Powder Oxidation on Defect Formation in Laser Additive Manufacturing,” *Acta Materialia*, **166**, pp. 294–305.
- [184] Scipioni Bertoli, U., Guss, G., Wu, S., Matthews, M. J., and Schoenung, J. M., 2017, “In-Situ Characterization of Laser-Powder Interaction and Cooling Rates through High-Speed Imaging of Powder Bed Fusion Additive Manufacturing,” *Materials & Design*, **135**, pp. 385–396.

## APPENDICES

**Table A.1: Table of powder samples acquired before and after each experimental run.**

Sample Name	Build Number	Condition	AM Atmosphere	Sample Mass (g, original)	Nominal Bottom Cut (um)	Nominal Top Cut (um)
ASC-1-81_P1	0	Virgin	N/A	4	20	45
ASC-1-81_P2	0	Virgin	N/A	4	20	45
ASC-1-81_P3	0	Virgin	N/A	4	45	53
ASC-1-81_P4	0	Virgin Jars 1-3 Blended	N/A	24	20	53
ASC-1-81_P5	0	Virgin Jars 1-3 Blended	N/A	24	20	53
ASC-1-81_P6	1	Left Bed_1 Use	Ar	2	20	53
ASC-1-81_P7	1	Right Bed 1 Use	Ar	2	20	53
ASC-1-81_P8	1	Post Build 1_1 Use	Ar	7	20	53
ASC-1-81_P9	2	Left Bed_1 Use	Ar	2	20	53
ASC-1-81_P10	2	Right Bed 1 Use	Ar	2	20	53
ASC-1-81_P11	2	Post Build 2_1 Use	Ar	7	20	53
ASC-1-81_P12	3	Right Bed 1 Use	Ar	2	20	53
ASC-1-81_P13	3	Post Build 3_1 Use	Ar	5	20	53
ASC-1-81_P14	4	Right Bed 1 Use	Ar	2	20	53
ASC-1-81_P15	4	Post Build 4_1 Use	Ar	6	20	53
ASC-1-81_P16	5	Right Bed 1 Use	Ar + 5	4	20	53
ASC-1-81_P17	5	Post Build 5_1 Use	Ar + 5	5	20	53
ASC-1-81_P18	6	Right Bed 1 Use	Ar + 5	3	20	53
ASC-1-81_P19	6	Post Build 6_1 Use	Ar + 5	6	20	53
ASC-1-81_P20	7	Right Bed 1 Use	Ar + 5	2	20	53

ASC-1-81_P21	7	Post Build 7_1 Use	Ar + 5	5	20	53
ASC-1-81_P22	8	Right Bed 1 Use	Ar + 10	3	20	53
ASC-1-81_P23	8	Post Build 8_1 Use	Ar + 10	6	20	53
ASC-1-81_P24	9	Right Bed 1 Use	Ar + 10	3	20	53
ASC-1-81_P25	9	Post Build 9_1 Use	Ar + 10	7	20	53
ASC-1-81_P26	10	Right Bed 1 Use	Ar + 10	4	20	53
ASC-1-81_P27	10	Post Build 10_1 Use	Ar + 10	6	20	53
ASC-1-81_P28	11	Pre-Build 11 Top Cut	Ar, 1 previous use		20	53
ASC-1-81_P29	11	Pre-Build 11	Ar, 1 previous use		20	45
ASC-1-81_P30	11	Right Bed 2 Use	Ar+10	4	20	45
ASC-1-81_P31	11	Post Build 11_2 Use	Ar+10	2	20	45
ASC-1-81_P32	12	Pre-Build 11	Ar, 1 previous use		20	45
ASC-1-81_P33	12	Right Bed 1 Use	Ar + 3	1	20	45
ASC-1-81_P34	12	Post Build 12_1 Use	Ar + 3	4	20	45
ASC-1-81_P35	13	Right Bed 1 Use	Ar+7		20	45
ASC-1-81_P36	13	Post Build 12_1 Use	Ar+7		20	45
ASC-1-81_P37		Pre-Build 14 Top Cut				

**Table A.2: Table of ASC-1-81 samples consolidated by LPBF.**

Sample ID	Date	Build	Pos.	Gas	Powder Condition	Hatch (mm)	Layer (mm)	Speed (mm/s)	Power (J/s)	Volumetric Energy Density (J/mm <sup>3</sup> )
ASC-1-81_S1	20211023	2	4	Ar	Virgin	0.05	0.025	760	95	100
ASC-1-81_S2	20211023	2	5	Ar	Virgin	0.05	0.025	380	95	200
ASC-1-81_S3	20211023	2	6	Ar	Virgin	0.05	0.025	608	95	125
ASC-1-81_S4	20211022	1	4	Ar	Virgin	0.05	0.025	507	95	150
ASC-1-81_S5	20211022	1	5	Ar	Virgin	0.03	0.025	608	95	208
ASC-1-81_S6	20211022	1	6	Ar	Virgin	0.05	0.025	338	95	225
ASC-1-81_S7	20211022	1	7	Ar	Virgin	0.08	0.025	304	95	156
ASC-1-81_S8	20211023	2	7	Ar	Virgin	0.03	0.025	760	95	167
ASC-1-81_S9	20211023	3	1	Ar	Virgin	0.03	0.025	507	95	250
ASC-1-81_S10	20211023	3	2	Ar	Virgin	0.08	0.025	507	95	94
ASC-1-81_S11	20211023	3	3	Ar	Virgin	0.08	0.025	760	95	63
ASC-1-81_S12	20211023	3	4	Ar	Virgin	0.08	0.025	338	95	141
ASC-1-81_S13	20211023	3	5	Ar	Virgin	0.03	0.025	434	95	292
ASC-1-81_S14	20211023	3	6	Ar	Virgin	0.08	0.025	434	95	109
ASC-1-81_S15	20211023	3	7	Ar	Virgin	0.08	0.025	380	95	125
ASC-1-81_S16	20211023	4	1	Ar	Virgin	0.08	0.025	608	95	78

ASC-1-81_S17	20211023	4	2	Ar	Virgin	0.03	0.025	380	95	333
ASC-1-81_S18	20211023	4	3	Ar	Virgin	0.03	0.025	1050	95	121
ASC-1-81_S19	20211023	4	4	Ar	Virgin	0.05	0.025	434	95	175
ASC-1-81_S20	20211023	4	5	Ar	Virgin	0.03	0.025	1700	95	75
ASC-1-81_S21	20211023	4	6	Ar	Virgin	0.05	0.025	304	95	250
ASC-1-81_S22	20211023	4	7	Ar	Virgin	0.015	0.025	1260	95	201
ASC-1-81_S23	20211023	5	1	Ar+5 %O2	Virgin	0.05	0.025	608	95	125
ASC-1-81_S24	20211023	5	2	Ar+5 %O2	Virgin	0.08	0.025	608	95	78
ASC-1-81_S25	20211023	5	3	Ar+5 %O2	Virgin	0.08	0.025	380	95	125
ASC-1-81_S26	20211023	5	4	Ar+5 %O2	Virgin	0.08	0.025	338	95	141
ASC-1-81_S27	20211023	5	5	Ar+5 %O2	Virgin	0.03	0.025	608	95	208
ASC-1-81_S28	20211023	5	6	Ar+5 %O2	Virgin	0.05	0.025	507	95	150
ASC-1-81_S29	20211023	5	7	Ar+5 %O2	Virgin	0.05	0.025	304	95	250
ASC-1-81_S30	20211023	6	1	Ar+5 %O2	Virgin	0.05	0.025	760	95	100
ASC-1-81_S31	20211023	6	2	Ar+5 %O2	Virgin	0.03	0.025	380	95	333
ASC-1-81_S32	20211023	6	3	Ar+5 %O2	Virgin	0.08	0.025	304	95	156

ASC-1-81_S33	20211023	6	4	Ar+5 %O2	Virgin	0.08	0.025	760	95	63
ASC-1-81_S34	20211023	6	5	Ar+5 %O2	Virgin	0.03	0.025	1700	95	75
ASC-1-81_S35	20211023	6	6	Ar+5 %O2	Virgin	0.03	0.025	507	95	250
ASC-1-81_S36	20211023	6	7	Ar+5 %O2	Virgin	0.05	0.025	380	95	200
ASC-1-81_S37	20211023	7	1	Ar+5 %O2	Virgin	0.05	0.025	434	95	175
ASC-1-81_S38	20211023	7	2	Ar+5 %O2	Virgin	0.03	0.025	760	95	167
ASC-1-81_S39	20211023	7	3	Ar+5 %O2	Virgin	0.03	0.025	1050	95	121
ASC-1-81_S40	20211023	7	4	Ar+5 %O2	Virgin	0.08	0.025	434	95	109
ASC-1-81_S41	20211023	7	5	Ar+5 %O2	Virgin	0.03	0.025	434	95	292
ASC-1-81_S42	20211023	7	6	Ar+5 %O2	Virgin	0.08	0.025	507	95	94
ASC-1-81_S43	20211023	7	7	Ar+5 %O2	Virgin	0.05	0.025	338	95	225
ASC-1-81_S44	20211024	8	1	Ar+1 %O	Virgin	0.03	0.025	1700	95	75
ASC-1-81_S45	20211024	8	2	Ar+1 %O	Virgin	0.05	0.025	434	95	175
ASC-1-81_S46	20211024	8	3	Ar+1 %O	Virgin	0.05	0.025	608	95	125

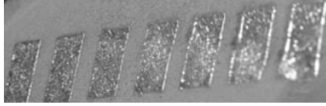
ASC-1-81_S47	20211024	8	4	Ar+1 0%O	Virgin	0.08	0.025	304	95	156
ASC-1-81_S48	20211024	8	5	Ar+1 0%O	Virgin	0.03	0.025	434	95	292
ASC-1-81_S49	20211024	8	6	Ar+1 0%O	Virgin	0.08	0.025	760	95	63
ASC-1-81_S50	20211024	8	7	Ar+1 0%O	Virgin	0.03	0.025	380	95	333
ASC-1-81_S51	20211024	9	1	Ar+1 0%O	Virgin	0.08	0.025	507	95	94
ASC-1-81_S52	20211024	9	2	Ar+1 0%O	Virgin	0.08	0.025	338	95	141
ASC-1-81_S53	20211024	9	3	Ar+1 0%O	Virgin	0.08	0.025	434	95	109
ASC-1-81_S54	20211024	9	4	Ar+1 0%O	Virgin	0.08	0.025	608	95	78
ASC-1-81_S55	20211024	9	5	Ar+1 0%O	Virgin	0.05	0.025	760	95	100
ASC-1-81_S56	20211024	9	6	Ar+1 0%O	Virgin	0.05	0.025	507	95	150
ASC-1-81_S57	20211024	9	7	Ar+1 0%O	Virgin	0.03	0.025	507	95	250
ASC-1-81_S58	20211024	10	1	Ar+1 0%O	Virgin	0.03	0.025	1050	95	121
ASC-1-81_S59	20211024	10	2	Ar+1 0%O	Virgin	0.08	0.025	380	95	125
ASC-1-81_S60	20211024	10	3	Ar+1 0%O	Virgin	0.05	0.025	338	95	225

ASC-1-81_S61	20211024	10	4	Ar+1 0%O	Virgin	0.03	0.025	760	95	167
ASC-1-81_S62	20211024	10	5	Ar+1 0%O	Virgin	0.05	0.025	304	95	250
ASC-1-81_S63	20211024	10	6	Ar+1 0%O	Virgin	0.03	0.025	608	95	208
ASC-1-81_S64	20211024	10	7	Ar+1 0%O	Virgin	0.05	0.025	380	95	200
ASC-1-81_S65	20211025	11	1	Ar+1 0%O	1 use*	0.05	0.025	608	95	125
ASC-1-81_S66	20211025	11	2	Ar+1 0%O	1 use*	0.08	0.025	338	95	141
ASC-1-81_S67	20211025	11	3	Ar+1 0%O	1 use*	0.05	0.025	304	95	250
ASC-1-81_S68	20211025	11	4	Ar+1 0%O	1 use*	0.05	0.025	380	95	200
ASC-1-81_S69	20211025	11	5	Ar+1 0%O	1 use*	0.08	0.025	434	95	109
ASC-1-81_S70	20211025	11	6	Ar+1 0%O	1 use*	0.03	0.025	434	95	292
ASC-1-81_S71	20211025	11	7	Ar+1 0%O	1 use*	0.05	0.025	338	95	225
ASC-1-81_S72	20211025	12	1	Ar+5 %O	1 use*	0.05	0.025	608	95	125
ASC-1-81_S73	20211025	12	2	Ar+5 %O	1 use*	0.03	0.025	434	95	292
ASC-1-81_S74	20211025	12	3	Ar+5 %O	1 use*	0.03	0.025	380	95	333

ASC-1-81_S75	20211025	12	4	Ar+5 %O	1 use*	0.08	0.025	507	95	94
ASC-1-81_S76	20211025	12	5	Ar+5 %O	1 use*	0.05	0.025	507	95	150
ASC-1-81_S77	20211025	12	6	Ar+5 %O	1 use*	0.05	0.025	338	95	225
ASC-1-81_S78	20211025	12	7	Ar+5 %O	1 use*	0.05	0.025	380	95	200
ASC-1-81_S79	20211025	13	1	Ar+3 %O	Virgin	0.05	0.025	380	95	200
ASC-1-81_S80	20211025	13	2	Ar+3 %O	Virgin	0.05	0.025	608	95	125
ASC-1-81_S81	20211025	13	3	Ar+3 %O	Virgin	0.05	0.025	338	95	225
ASC-1-81_S82	20211025	13	4	Ar+3 %O	Virgin	0.08	0.025	304	95	156
ASC-1-81_S83	20211025	13	5	Ar+3 %O	Virgin	0.03	0.025	760	95	167
ASC-1-81_S84	20211025	13	6	Ar+3 %O	Virgin	0.08	0.025	507	95	94
ASC-1-81_S85	20211025	13	7	Ar+3 %O	Virgin	0.08	0.025	608	95	78
ASC-1-81_S86	20211026	14	1	Ar+7 %O	Virgin	0.05	0.025	380	95	200
ASC-1-81_S87	20211026	14	2	Ar+7 %O	Virgin	0.05	0.025	608	95	125
ASC-1-81_S88	20211026	14	3	Ar+7 %O	Virgin	0.05	0.025	338	95	225

ASC-1-81_S89	20211026	14	4	Ar+7 %O	Virgin	0.08	0.025	304	95	156
ASC-1-81_S90	20211026	14	5	Ar+7 %O	Virgin	0.03	0.025	760	95	167
ASC-1-81_S91	20211026	14	6	Ar+7 %O	Virgin	0.08	0.025	507	95	94
ASC-1-81_S92	20211026	14	7	Ar+7 %O	Virgin	0.08	0.025	608	95	78
ASC-1-81_S93	20211026	15	1	Argon	1 use+	0.05	0.025	608	95	125
ASC-1-81_S94	20211026	15	2	Argon	1 use+	0.05	0.025	608	95	125
ASC-1-81_S95	20211026	16	2	Argon	1 use+	0.08	0.025	608	95	78
ASC-1-81_S96	skipped by accident				1 use+	0	0			
ASC-1-81_S97	20211026	16	1	Argon	1 use+	0.08	0.025	608	95	78
ASC-1-81_S98	20211027	17	2	Argon	1 use+	0.05	0.025	608	95	125
ASC-1-81_S99	20211027	17	1	Argon	1 use+	0.05	0.025	608	95	125

Build 1:5-7



Build 2: 1-4



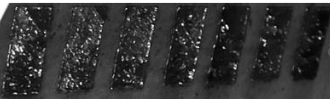
Build 3:9-15



Build 4:S16-21



Build 5:S22-29



Build 6: S30-36



Build 7: S37-43



Build 8: S44-50



Build 9: S51-57



Build 10: S58-64



Build 11: S65-71



Build 12: S72-78



Build 13: S79-85



Build 14: S86-92



**Figure A.1: Collection of Photos for each build with sample numbers (15 x 7.5 x 4 mm) used to generate the processing space for ASC 1-81 GARS Fe ferritic powder using LPBF.**